

TOKAMAK DENSITY LIMITS

**A Thesis
Presented to
The Academic Faculty**

by

Frederick Alan Kelly

**In Partial Fulfillment
of the Requirements for the Degree
Doctor of Philosophy in Nuclear Engineering
in the School of Mechanical Engineering**

**Georgia Institute of Technology
December 2000**

TOKAMAK DENSITY LIMITS

Approved:

Weston M. Stacey, Chairman

Alan V. Larson

Thomas W. Petrie

Edward W. Thomas

C. K. Chris Wang

Date Approved 12/13/00

ACKNOWLEDGEMENTS

I wish to express my appreciation to my advisor, Professor W. M. Stacey, Jr., for laying the theoretical foundation of this work and for his continued support and guidance throughout its completion. I am grateful to the members of my reading committee, Professors A. V. Larson, E. W. Thomas and C. K. Wang, and T. W. Petrie for making their valuable time available to read the text and make useful comments.

I thank Dr. J. Rapp for supplying TEXTOR data and many discussions. Thanks are due to M. Brix, M. Lehnen and J. Ongena for processing TEXTOR data and discussing TEXTOR's diagnostics. Thanks are also due to M. Z. Tokar for discussing thermal instability theory.

I am thankful to Drs. J. Mandrekas and D. Zhang for providing the FIRE data and to the former for providing the fits to impurity radiation used in the calculations.

We owe a tremendous debt to the scientists that have gone before. In particular, Werner Heisenberg in Physics and Philosophy reminds us that "we have to remember that what we observe is not nature in itself but nature exposed to our method of questioning."

This research was sponsored by the U. S. Department of Energy under Grant Nos. DE-FG02-96ER54350 and DE-FG02-99ER54538.

TABLE OF CONTENTS

| | Page |
|--|------|
| ACKNOWLEDGEMENTS | iii |
| LIST OF TABLES | vi |
| LIST OF FIGURES | vii |
| SUMMARY | xi |
| CHAPTER | |
| I. INTRODUCTION TO TOKAMAK DENSITY LIMITS | 1 |
| 1.1 Background | |
| 1.2 Outline of Thesis | |
| II. THERMAL INSTABILITY DENSITY LIMIT THEORIES | 7 |
| 2.1 Introduction | |
| 2.2 MARFE Theory | |
| 2.3 Radiative Collapse Theory | |
| III. MEASUREMENTS IN TEXTOR | 18 |
| 3.1 Introduction | |
| 3.2 TEXTOR Diagnostics | |
| 3.3 The TEXTOR Plasma Edge | |
| 3.3.1 Poloidal Asymmetries in Data | |
| 3.3.2 Treatment of Shafranov Shift Effects in the Data | |
| 3.3.3 Correction of Gradient Scale Lengths for Shafranov Shift | |
| IV. ANALYSIS OF MARFE ONSET IN TEXTOR | 40 |
| 4.1 Introduction | |
| 4.2 Use of Experimental Data in Evaluating the MI | |
| 4.3 Processing of Measured Data | |
| 4.4 Analysis of Shot 80252 | |

| | | |
|-------|--|-----|
| 4.5 | Analysis of Power Scan Shots | |
| 4.6 | Summary | |
| V. | ANALYSIS OF PARAMETRIC DEPENDENCE IN TEXTOR DENSITY LIMIT SHOTS | 63 |
| 5.1 | Introduction | |
| 5.2 | TEXTOR Operating History | |
| 5.2.2 | Ohmic Plasmas | |
| 5.2.2 | Auxiliary Heated Plasmas | |
| 5.3 | MARFE Onset Parameter Dependencies in TEXTOR | |
| 5.3.1 | Current Scaling | |
| 5.3.2 | Magnetic Field Scaling | |
| 5.3.3 | Power Scaling | |
| 5.3.4 | Plasma Position Dependence | |
| 5.3.5 | Wall Material | |
| 5.4 | Radiative Collapse Density Limit Parameter Dependence in TEXTOR | |
| 5.5 | Symmetric Detachment or MARFE as the Density Limiting Phenomenon? | |
| 5.6 | Conclusions | |
| VI. | DENSITY LIMITS OF THE FUSION IGNITION RESEARCH EXPERIMENT (FIRE) | 105 |
| 6.1 | Introduction | |
| 6.2 | Analysis of MARFE Density Limit in FIRE | |
| 6.3 | Analysis of Disruptive Density Limit in FIRE | |
| 6.4 | Transport Barrier Neural Concentration in FIRE | |
| 6.5 | Discussion and Conclusions | |
| VII. | SUMMARY AND CONCLUSIONS | 123 |
| | REFERENCES | 127 |
| | VITA | 137 |

LIST OF TABLES

| Table | Page |
|--|-------------|
| 4.1 Experimental parameters at MARFE onset for TEXTOR power scan with background 3 and new atomic coefficients. | 48 |
| 4.2 Evaluation of the MARFE Index at MARFE onset for the TEXTOR power scan. | 49 |
| 6.1 Baseline FIRE machine parameters. | 107 |
| 6.2 Maximum allowed impurity fractions for ignition. | 108 |

LIST OF FIGURES

| Figure | Page |
|---|------|
| 1.1 Edge operational diagram showing regime boundaries and experimental results of ASDEX Upgrade (discharges with $I_p = 1$ MA only). | 6 |
| 3.1 Poloidal cross-section of TEXTOR with its limiters. | 30 |
| 3.2 The TEXTOR heating system, with 2 antenna pairs (ICRH) and 2 neutral injector plug-in (PINI) systems (one co- and one counter-injector). | 31 |
| 3.3 a) View of the He-beam sources and their respective observation systems and b) schematic view in a poloidal cross-section with Shafranov shifted LCFS surface. | 32 |
| 3.4 LFS radial profiles of the line intensities at $\lambda_1 = 667.8$ nm, $\lambda_2 = 728.1$ nm, and $\lambda_3 = 706.5$ nm. The dotted line represents the subtracted intensity of the estimated background light. | 33 |
| 3.5 Top view of TEXTOR showing region visible to CCD camera. | 34 |
| 3.6 Radial edge profiles of a) n_e and b) T_e at three poloidal positions in shot 77536. | 35 |
| 3.7 Measured density and temperature profiles at the LFS and HFS for different plasma densities. ($P_{\text{heat}} = 1.55$ MW) | 36 |
| 3.8 Density and temperature profiles measured at the LFS for different neutral beam heating power. (Line averaged central density $n_e = 3.9 \times 10^{19} \text{ m}^{-3}$) | 37 |
| 3.9 Model of TEXTOR tokamak and plasma geometry when limited by the ALT-II limiter. | 38 |
| 3.10 Schematic used to determine the plasma major radius $R_o' = R(\rho_{\text{plasma}})$ and minor radius $a' = \rho_{\text{plasma}}$ on the basis of the electron density profile measurement. | 39 |

| | | |
|------|--|----|
| 4.1 | Experimental line average density versus auxiliary heating power at MARFE onset. | 52 |
| 4.2 | Experimental radiated and ohmic heating powers versus auxiliary heating power at MARFE onset. | 53 |
| 4.3 | ALT-II limiter fluxes versus power crossing separatrix at MARFE onset. | 54 |
| 4.4 | Bumper limiter fluxes versus power crossing separatrix at MARFE onset. | 55 |
| 4.5 | LFS electron temperature at the separatrix versus auxiliary heating power with different data processing. | 56 |
| 4.6 | LFS electron density at the separatrix versus auxiliary heating power with different data processing. | 57 |
| 4.7 | Temperature decay length just inside the separatrix versus auxiliary heating power at MARFE onset with different data processing. | 58 |
| 4.8 | Density decay length just inside the separatrix versus auxiliary heating power at MARFE onset with different data processing. | 59 |
| 4.9 | MARFE Index versus auxiliary heating power at MARFE onset with different data processing. | 60 |
| 4.10 | MARFE Index versus auxiliary heating power before and at MARFE onset using new atomic coefficients and background 2. | 61 |
| 4.11 | Uncertainty of MARFE Index versus auxiliary heating power. | 62 |
| 5.1 | Hugill-diagram of TEXTOR. | 91 |
| 5.2 | The line averaged density \bar{n}_e , the electron temperature on axis $T_e(R_0)$ and the total radiated power P_{rad} from an ohmic discharge which disrupted at the density limit. | 92 |
| 5.3 | a) Electron temperature profile and b) radial density profile at the beginning of contraction. CCD camera recording showed plasma detachment from the limiters. The temperature gradient region is | |

| | |
|---|-----|
| indicated by the ∇T_e on the high field side of the profile. The labels EC1, etc., denote ECE channels. | 93 |
| 5.4 Temporal evolution of the radiative collapse of TEXTOR shot 71257: heated and radiated powers, solid curves; line-averaged density, dashed curve; Z_{eff} , plus symbols. Neon injection begins at 1.5 s and the time of disruption is indicated by the vertical line. | 94 |
| 5.5 Line-averaged density versus Z_{eff} comparison of TEXTOR shots that disrupted after detachment or MARFEs. Evolution of three radiative collapse discharges that detached (solid curves) and the predicted density limit (chain curves). The circles indicate discharges that MARFEd before disrupting near the Greenwald limit (horizontal dashed line). | 95 |
| 5.6 Disruptive density limit versus average current density for auxiliary heated TEXTOR discharges ($P_{aux} = 1.1-2.3$ MW). The chained line indicates the Greenwald limit. | 96 |
| 5.7 \bar{n}_e scaling with global parameters ($I_p = 350$ kA, $P_{NBI} = 1.4$ MW): a) toroidal magnetic field, $n_e^{cr} \propto B_t^{-0.5}$ solid line, $n_e^{cr} \propto a + b \times B_t^{-0.5}$ dashed line, $n_e^{cr} \propto B_t^{-1}$ dash-dot line; b) heating power, $n_e^{cr} \propto P_{heat}^{0.16}$. | 97 |
| 5.8 \bar{n}_e versus P_{sep} for shots 81531-81532, 81573-81581, 81537-81539 at MARFE onset ($I_p = 350$ kA and $B_T = 2.25$ T). | 98 |
| 5.9 $n_e(a)$ versus P_{sep} for shots 81532, 81573-81575, 81577, 81579, 81581 at MARFE onset ($I_p = 350$ kA and $B_T = 2.25$ T). | 99 |
| 5.10 Radiative cooling rates of carbon, oxygen and silicon versus electron temperature. | 100 |
| 5.11 Dependence of the disruptive density limit on the horizontal plasma position ($I_p = 270$ kA, $P_{aux} = 0.9-1.0$ MW). The Greenwald limit is indicated by the dashed line. | 101 |
| 5.12 $\langle\sigma v\rangle$ ($\text{cm}^3 \text{s}^{-1}$) for recombination and ionization. | 102 |
| 5.13 a) Local electron density, b) temperature, c) D/H flux at the limiter and d) global radiation level as a function of line-averaged electron density. The data for ohmic heating, $I_p = 340$ kA and deuterium | |

| | |
|---|-----|
| filling are used as the reference case. The variation of parameters (plasma current, neutral beam heating “NBI” and hydrogen filling “H”) with respect to the reference data are indicated. | 103 |
| 5.14 Variation of the plasma edge parameters n_e and T_e and the radiative fraction with line-average density, with and without auxiliary heating ($P_{heat} = 0.3/1.5$ MW), and for siliconized and boronized conditions. | 104 |
| 6.1 FIRE baseline ion and electron temperature profiles. | 113 |
| 6.2 FIRE baseline ion and electron density profiles. | 114 |
| 6.3 MARFE Index versus neutral fraction for FIRE with varied λ 's. | 115 |
| 6.4 MARFE Index versus neutral fraction for FIRE with varied impurities. | 116 |
| 6.5 MARFE Index versus neutral fraction for FIRE with varied beryllium concentration. | 117 |
| 6.6 MARFE Index versus neutral fraction for FIRE with varied carbon concentration.. | 118 |
| 6.7 MARFE Index versus neutral fraction for FIRE with varied neon concentration.. | 119 |
| 6.8 MARFE Index versus neutral fraction for FIRE with varied iron concentration.. | 120 |
| 6.9 FIRE lower divertor edge geometry and GTNEUT computational regions. | 121 |
| 6.10 a) Neutral densities in the regions just inside the FIRE separatrix and b) net neutral influx from edge to core from regions inside the separatrix. | 122 |

SUMMARY

The measured density limits in the German Tokamak TEXTOR have been analyzed. For a series of 'power scan' shots that ended in multifaceted asymmetric radiation from the edge (MARFE), in which the auxiliary heating power was varied and other operating parameters were held approximately constant, this analysis consisted of: 1) correcting the basic measurements of density and temperature distributions for the background light, Shafranov shift, etc. to obtain 'measured' density and temperature profiles for comparison with theory; 2) calculation of neutral atom and impurity ion concentrations in the plasma edge region by attenuating measured gas sources at various plasma-wall interaction locations (limiters) into the plasma with a numerical calculation; 3) identification of uncertainties in the measured and calculated experimental data; 4) evaluation of theoretical prediction of the onset of MARFEs due to thermal instabilities in the plasma edge; and 5) comparison of measured and predicted MARFE onset, taking into account uncertainties.

The parametric dependence of the measured conditions for MARFE onset and for radiative collapse leading to disruption in TEXTOR were compared with the parametric dependence of predictions of MARFE onset and radiative collapse given by thermal instability theory, over a range of values for plasma current, magnetic field and auxiliary heating power and over a range of wall materials and wall conditions.

Based on the agreement between theoretical prediction and experiment found in the TEXTOR analyses, the MARFE and radiative collapse density limits were predicted for the proposed FIRE burning plasma experiment.

CHAPTER I

INTRODUCTION TO TOKAMAK DENSITY LIMITS

1.1 Background

The thermonuclear power in a tokamak reactor is proportional to $n^2 \langle \sigma v \rangle V$. In order to achieve adequate fusion power performance, future tokamak reactors must operate safely at high density, while retaining sufficiently high energy confinement, or become large and costly. Stable plasmas must be reliably produced with central densities well above 10^{20} m^{-3} . The average densities for these plasmas are expected to be near or beyond the limits observed in current tokamak experiments, which can be bounded by the empirical Greenwald limit [1.1], $n_{\text{GW}}(10^{20} \text{ m}^{-3}) = I(\text{MA})/\pi a^2(\text{m})$. Confinement is generally observed to degrade when the Greenwald limit is approached. Although it was developed from a database of ohmic and auxiliary heated low-confinement (L-mode) plasmas, the empirical Greenwald limit has been successful in describing high-confinement (H-mode) plasmas. While it is not clear that the Greenwald limit can extrapolate to tokamak reactors, such a density limit provides a strong motivation to understand its physical basis.

Recently, there has been an extensive investigation in tokamaks (DIII-D [1.2-1.7], TEXTOR [1.8-1.12], ASDEX [1.13-1.16], JET [1.17-1.21]) both to understand the physical mechanisms and to find operating regimes capable of exceeding the Greenwald limit.

Experimentally, the density is limited in a variety of ways: by MHD instabilities leading to a disruption; by the inability to further increase the density with continued fueling because of confinement degradation; or by the increase of power losses in the edge causing a collapse of the radial temperature profile leading to a disruption. The most common density limit is the fueling limit related to confinement degradation. The fueling density limit is frequently associated with an H-L transition followed by a MARFE (Multifaceted Asymmetric Radiation From the Edge). The dependence on edge temperature and density of this operational limit in ASDEX Upgrade is clearly illustrated in Figure 1.1 [1.22].

Core MARFEs followed by a H-L (high-to-low confinement mode) transition, limit the density well below the Greenwald limit in continuous gas puffed lower single-null DIII-D discharges with low triangularity. Similar continuous gas puff fueled DIII-D discharges with higher triangularity or with pumping in the lower divertor have achieved densities near or above the Greenwald value, apparently limited by confinement deterioration, without the formation of core MARFEs. Pellet fueled DIII-D discharges have achieved densities up to twice the Greenwald value, limited by global radiative collapse [1.7].

Tokamaks operating near the density limit often terminate with disruptions that have the potential to be massively destructive when projected to tokamak reactors. Disruptions can occur with little warning in tokamaks operating close to limits in β and q_95 . The energy stored in the plasma is deposited rapidly onto the divertor plates, limiters

and walls. The vertical stability of an elongated plasma column may be lost after a disruption, and then the combination of the plasma motion and plasma current decay induces eddy currents both in the vacuum vessel and in the halo region around the plasma, resulting in large and potentially destructive forces on the vacuum vessel and plasma-facing components. While concepts are being developed to ameliorate the effects of disruptions, it is clear that the ability to reliably predict and prevent disruptions would be a far superior solution [1.23]. Thus, it is important to understand the mechanisms responsible for the density limit.

Many theoretical explanations for density limits have been advanced. The thermal instability of the radial temperature and density profiles, driven by radiation and atomic physics losses in the plasma edge, can cause a collapse of the edge temperature profile [1.24-1.28] if the density is sufficiently large. Such a collapse is usually followed by strong MHD activity and a disruption. These “hard” density limits have been observed in most tokamaks under certain conditions. The power and particle balances in the divertor and scrape-off layer can place an upper limit on the edge plasma density and hence on the overall plasma density [1.29-1.31]. Core MARFES, which are radiation and atomic physics driven thermal instabilities along the closed field lines in the plasma edge [1.32-1.40], could cause a deterioration of confinement or lead to a disruptive collapse of the discharge. MHD activity or electrostatic instabilities also could increase edge transport and degrade confinement.

The MARFE was first explained as a radiation-driven thermal instability by Neuhauser et al. [1.32] and Drake [1.33]. Stacey [1.34-1.40] has developed a general theoretical formalism, based on linear thermal instability of the plasma edge, that enables a quantitative prediction of the MARFE onset density limit in tokamaks and explains the dependence of this density limit on the parameters of the plasma edge with physical processes of atomic radiation, charge-exchange, elastic scattering and ionization. Recently, this theory has been successfully applied to quantitative MARFE onset prediction in DIII-D [1.6,1.7].

The purpose of this thesis is to investigate the role of thermal instabilities, in particular MARFEs, in determining the density limits in TEXTOR. We have examined a number of L-mode shots that terminated with MARFEs in a scan of the NBI (Neutral Beam Injection) heating power, all at constant magnetic field and plasma current. One other MARFE shot in TEXTOR at a different current was also examined.

We also make predictions of the density limits of a proposed next-step option for the United States fusion program.

1.2 Outline of Thesis

The second chapter describes the MARFE and disruptive collapse thermal instability theories of the physics mechanisms underlying the density limit. The third chapter reviews the experimental setup of the TEXTOR tokamak. The fourth chapter examines MARFE onset in TEXTOR and compares the MARFE theory developed in

chapter two with experimental observations. Chapter five gives a qualitative comparison of the parameter dependence of the measured density limit in TEXTOR with the predictions of the two thermal instability theories of chapter two. Chapter six examines the density limit characteristics of the proposed Fusion Ignition Research Experiment (FIRE). The conclusions drawn from this thesis are contained in the seventh chapter.

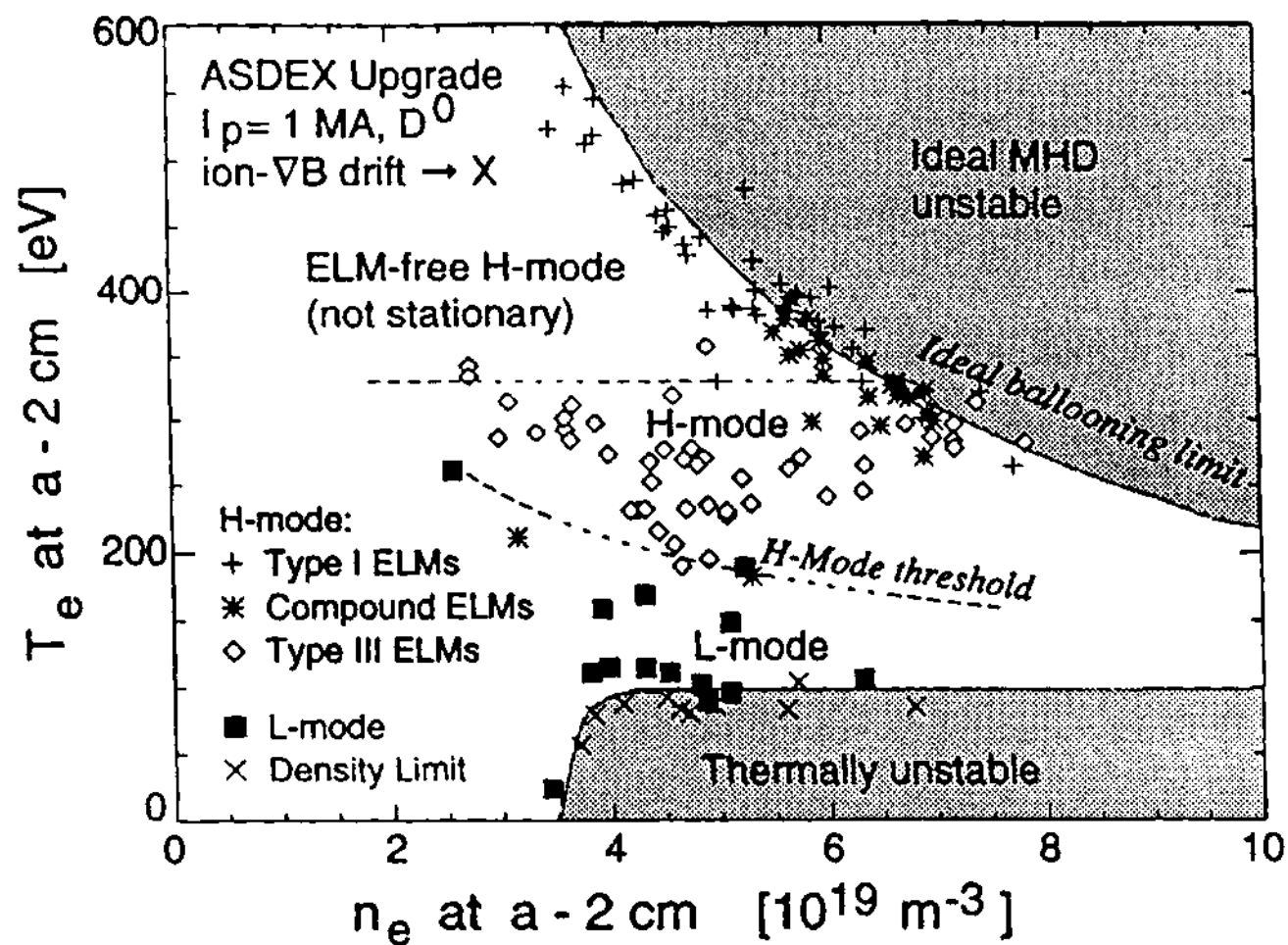


Figure 1.1 Edge operational diagram showing regime boundaries and experimental results of ASDEX Upgrade (discharges with $I_p = 1$ MA only).

CHAPTER II

THERMAL INSTABILITY DENSITY LIMIT THEORIES

2.1 Introduction

Rather than a single physical mechanism limiting the maximum achievable density in a tokamak plasma, experiment suggests multiple causes, resulting in many theoretical explanations for density limits being postulated.

The MARFE (Multifaceted Asymmetric Radiation From the Edge) phenomenon has long been observed in tokamak experiments above a certain density [2.1,2.2]. It is characterized by a toroidally symmetric, poloidally asymmetric belt of cold dense, strongly radiating plasma, usually forming first at the inner edge of the torus in limited plasmas and at the X-point in diverted plasmas. The MARFE has been explained in terms of long wavelength parallel [2.3-2.8] or parallel-perpendicular [2.9-2.10] thermal instabilities along the closed field lines just inside the separatrix driven by a radiative condensation mechanism. A theory for the MARFE instability as a local cooling of the plasma driven by an ionization-recombination instability of recycling neutrals has also been proposed [2.11,2.12]. MARFEs appear to cause confinement to deteriorate or lead to a disruptive collapse of the discharge.

Short radial wavelength thermal instabilities in the plasma edge, driven by neutral atom cooling due to ionization, charge exchange and elastic scattering and by impurity

radiation, could cause enhanced edge transport resulting in a deterioration of confinement and a limiting of the achievable density [2.13,2.14].

The phenomenon of thermal radiative collapse is seen as a radiating zone at the plasma edge which suddenly propagates inward, leaving behind a region of reduced temperature, and usually leads to a disruption. The radiative collapse of the radial temperature and density profiles leading to a disruption has been explained [2.15-2.18] as a long wavelength, essentially radial thermal instability driven by radiation in the edge.

Mechanisms other than thermal instabilities can also limit the achievable density. The inability to obtain equilibrium solutions for the power and particle balances above a certain density in the divertor and scrape-off layer can place an upper limit on achievable densities in the scrape-off layer, which in turn would limit the edge plasma density and hence the overall plasma density [2.19-2.21]. Large scale MHD instabilities are also observed to cause confinement degradation.

In this thesis, we examine in detail the MARFE density limit and also consider the disruptive collapse. The thermal instability theories for the MARFE and the radiative collapse theories used in this work are described in section 2.2 and 2.3, respectively.

2.2 MARFE Theory

A linear analysis of the stability of the coupled fluid density, momentum and energy balance equations to one-dimensional (parallel) or two-dimensional (parallel-perpendicular or poloidal-toroidal) perturbations just inside the last closed flux surface (LCFS) leads to a

dispersion relation for the growth of the perturbation [2.8,2.13]. It was shown

theoretically [2.8] and confirmed computationally [2.10] that larger

$k_{\parallel} = (m + n q B_{\theta} / B) / qR$ modes are progressively more stable and $k_{\parallel} \equiv 0$ modes

are the least stable (m and n are the poloidal and toroidal mode numbers), because the

parallel thermal diffusivity is large and the stabilizing term $k_{\parallel}^2 \chi_{\parallel}$ appears in the

dispersion relation. In this context, an (m = 0, n = 0) instability corresponds to a uniform

heating or cooling of the plasma edge or to a uniform edge density increase or decrease,

not to an instability which penetrates into the plasma core.

We calculate the edge density at which the uniform $k_{\parallel} \equiv 0$ modes become

unstable - the MARFE onset condition. These modes subsequently couple to and trigger

the nonuniform modes which constitute the stable MARFE. The finite- k_{\parallel} dispersion

relation for coupled two-dimensional perturbations in the density, temperature and

velocity [2.13] is used to determine a maximum edge plasma density for which a non-

positive growth rate is possible (i.e. for stability). This expression is evaluated in the limit

$k_{\parallel} \rightarrow 0$ to obtain a conservative estimate for the maximum density for which the uniform

equilibrium solution is stable; the MARFE onset density n_{MARFE} .

$$\begin{aligned}
n_{\text{MARFE}} = & \left[\chi_r \left(\nu L_T^{-2} - (1 - C^{(2)}) L_T^{-1} L_n^{-1} \right) \right] \div \left\{ f_z \left[\left(\nu + 1 - C^{(2)} \right) \frac{L_z}{T} - \frac{\partial L_z}{\partial T} \right] + \right. \\
& f_0 \left[\frac{E_{\text{ion}} \langle \sigma v \rangle_{\text{ion}}}{T} \left(\nu - \frac{T}{\langle \sigma v \rangle_{\text{ion}}} \frac{\partial \langle \sigma v \rangle_{\text{ion}}}{\partial T} \right) \right] + \\
& \left. f_0^{\text{cold}} \left[\frac{3}{2} \left(\langle \sigma v \rangle_{\text{cx}} + \langle \sigma v \rangle_{\text{el}} \right) \left(\nu - 1 - T \frac{\partial \left(\langle \sigma v \rangle_{\text{cx}} + \langle \sigma v \rangle_{\text{el}} \right) / \partial T}{\left(\langle \sigma v \rangle_{\text{cx}} + \langle \sigma v \rangle_{\text{el}} \right)} \right) \right] \right\}
\end{aligned} \tag{2.1}$$

where f_0 and f_0^{cold} are the total and previously uncollided neutral concentrations, f_z and L_z are the impurity concentration and radiation function, ν characterizes the temperature dependence of the radial heat conductivity ($\chi_r \sim T^\nu$), E_{ion} is the deuterium ionization energy and the $\langle \sigma v \rangle_x$ are the atomic rate coefficients with $x = \text{cx}$, el , and ion referring to charge-exchange, elastic scattering and ionization, respectively. The radiation function is evaluated from a fit to coronal equilibrium solutions, with neutral atom charge exchange recombination taken into account [2.22,2.23]. L_T and L_n are the temperature and density gradient scale lengths, all just inside the last closed flux surface (LCFS). The gradient scale lengths (also known as decay lengths, λ_X) are defined for $X = T, n$ as

$$L_X = \lambda_X \equiv \left(-\frac{1}{X} \frac{\partial X}{\partial r} \right)^{-1} \tag{2.2}$$

The impurities are assumed to be entrained with the ions, and the ion and impurity momentum equations are summed. This results in

$$C^{(2)} = \frac{1.5}{Z_{\text{eff}}} \left(1 - \frac{0.6934}{1.3167 Z_{\text{eff}}} \right) \left(1 + \frac{n_z Z^2}{n_i} \right) \quad (2.3)$$

a quantity related to the thermal friction [2.24].

In order to evaluate the MARFE onset density from experimental measurement, an effective edge thermal diffusivity can be defined from the expression for the conducted heat flux

$$q_r = \chi n T L_T^{-1} = Q_r f_{\text{cond}} \quad (2.4)$$

where $Q_r = P_{\text{sep}}/A_{\text{LCFS}}$ is the total heat flux flowing across the LCFS from the core into the scrape-off layer (SOL), f_{cond} is the fraction of this heat flux which is conductive, P_{sep} is the conductive and convective power crossing the LCFS and A_{LCFS} is the area of the LCFS .

The MARFE onset edge density then becomes

$$\begin{aligned}
n_{\text{MARFE}} = & \left[\frac{f_{\text{cond}} P_{\text{sep}}}{T A_{\text{LCFS}}} \left(\nu L_T^{-1} - (1 - C^{(2)}) L_n^{-1} \right) \right]^{\frac{1}{2}} + \\
& \left\{ f_z \left[\left(\nu + 1 - C^{(2)} \right) \frac{L_z}{T} - \frac{\partial L_z}{\partial T} \right] + \right. \\
& f_0 \left[\frac{E_{\text{ion}} \langle \sigma v \rangle_{\text{ion}}}{T} \left(\nu - \frac{T}{\langle \sigma v \rangle_{\text{ion}}} \frac{\partial \langle \sigma v \rangle_{\text{ion}}}{\partial T} \right) \right] + \\
& \left. f_0^{\text{cold}} \left[\frac{3}{2} \left(\langle \sigma v \rangle_{\text{cx}} + \langle \sigma v \rangle_{\text{el}} \right) \left(\nu - 1 - T \frac{\partial \left(\langle \sigma v \rangle_{\text{cx}} + \langle \sigma v \rangle_{\text{el}} \right) / \partial T}{\left(\langle \sigma v \rangle_{\text{cx}} + \langle \sigma v \rangle_{\text{el}} \right)} \right) \right] \right\}^{\frac{1}{2}} \quad (2.5)
\end{aligned}$$

It is convenient to define the MARFE Index (MI)

$$\text{MI} = \frac{n_{\text{exp}}}{n_{\text{MARFE}}} \quad (2.6)$$

as the ratio of the actual plasma edge density to n_{MARFE} , which predicts MARFE onset when $\text{MI} > 1$. Equations (2.5) and (2.6) have been found to predict MARFE onset in good agreement with experiment in several DIII-D H-mode shots [2.25, 2.26].

An attractive aspect of this formulation of thermal instability theory is the fact that it leads to a simple expression for the MARFE onset density limit that can be readily evaluated from the experimental data, without requiring a coupled multimode dynamics

calculation [2.10]; however, the calculation of the subsequent MARFE evolution would require a multimode, or other, spatial dynamics simulation.

2.3 Radiative Collapse Theory

By using a coupled radial temperature-density perturbation in a linear analysis the energy and density equations summed over ions and electrons in a 1-D cylindrical approximation, it can be shown that global thermal instabilities are driven by radiation in the plasma edge. The perturbed solution that arises in the linear analysis satisfies an equation which would be Bessel's equation if certain spatial-dependent quantities are replaced by an average value. Such a linear analysis [2.18] of the stability of the global core plasma equilibrium against thermal instabilities driven by edge radiation leads to a prediction of the maximum value of the volume-average density for which the equilibrium is stable with respect to a radiative collapse of the radial temperature and density profiles

$$n_{av} \leq n_{RC} \equiv f^{-1} \frac{\left[\hat{\chi}_{\perp} \left(\frac{5.5}{a} \right)^2 \langle g \rangle + 2y \left(f_z \langle g L_z \rangle - \left\langle \frac{1}{4} U_a g (\sigma v) \right\rangle \right) \right]}{2 \left\langle \frac{1}{4} U_a g \frac{\partial (\sigma v)}{\partial T} + f_z \left(-\frac{\partial \mathcal{L}_z}{\partial T} \right) g^2 \right\rangle} \times$$

$$\left[1 \pm \sqrt{1 + \frac{4 \left(\left\langle -\frac{\partial \hat{H}}{\partial T} \right\rangle - y \left\langle \frac{\partial \hat{H}}{\partial n} \right\rangle \right) \left\langle \frac{1}{4} U_a g \frac{\partial (\sigma v)}{\partial T} + f_z \left(-\frac{\partial \mathcal{L}_z}{\partial T} \right) g^2 \right\rangle}{\left(\hat{\chi}_{\perp} \left(\frac{5.5}{a} \right)^2 \langle g \rangle + 2y \left(f_z \langle g L_z \rangle - \left\langle \frac{1}{4} U_a g (\sigma v) \right\rangle \right) \right)^2}} \right] \quad (2.7)$$

where the spatial average for a quantity X is defined as [2.18]

$$\langle X \rangle \equiv \frac{\int_0^a r X(r) J_0(5.5r/a) dr}{\int_0^a r J_0(5.5r/a) dr} \quad (2.8)$$

with J_0 being the zero order Bessel function. $\hat{H}(r)$ is the heating distribution due to auxiliary heating sources and ohmic heating. (σv) is the fusion reactivity and U_a is the fusion energy release. $f_z = n_z / n$ is the impurity fraction, and $L_z(T)$ is the impurity radiation function. $f = n_o / n_{av}$ is the peak-to-average factor for the equilibrium density distribution, and $g(r) = n(r) / n_o$ is the radial density distribution. The perturbed temperature and density distributions have the form [2.18]

$$\tilde{T}(r) = \tilde{T}_0 J_0(\mu r) \quad (2.9)$$

$$\tilde{n}(r) = \tilde{n}_0 J_0(\mu r) \quad (2.10)$$

We require that $\tilde{T}(a) = \tilde{n}(a) = 0$ at the second zero crossing of J_0 , so that $\mu a = 5.5$. A positive value of \tilde{T}_0 corresponds to a collapsing temperature profile. The variable y is defined as

$$y \equiv \frac{\tilde{n}_0}{\tilde{T}_0} \quad (2.11)$$

y introduces the effect of coupled density instabilities on the density limit for collapse of the temperature profile and is given by [2.18]

$$y = \frac{-b \mp \sqrt{b^2 - 4ac}}{2a} \quad (2.12)$$

where

$$\begin{aligned}
a &\equiv 3\langle T \rangle \left(\left\langle \frac{\partial S}{\partial n} \right\rangle - \mu^2 \hat{D}_\perp \right) - \left\langle \frac{\partial \hat{H}}{\partial n} + 2\bar{n} \left(\frac{1}{4} U_\alpha (\sigma v) - f_z L_z \right) \right\rangle \\
b &\equiv 3\langle \bar{n} \rangle \left(\left\langle \frac{\partial S}{\partial n} \right\rangle - \mu^2 \hat{D}_\perp \right) + 3\langle T \rangle \left\langle \frac{\partial S}{\partial T} \right\rangle - \\
&\quad \left\langle \frac{\partial \hat{H}}{\partial T} + \bar{n}^2 \left(\frac{1}{4} U_\alpha \frac{\partial (\sigma v)}{\partial T} + f_z \left(-\frac{\partial L_z}{\partial T} \right) \right) \right\rangle + \langle \bar{n} \rangle \mu^2 \hat{\chi}_\perp \\
c &\equiv 3\langle \bar{n} \rangle \left\langle \frac{\partial S}{\partial T} \right\rangle
\end{aligned} \tag{2.13}$$

The quantities $\hat{\chi}_\perp = \langle \bar{n} \chi \rangle / \langle \bar{n} \rangle$ and $\hat{D}_\perp = \langle D_\perp \rangle$ are average thermal and particle diffusivities, respectively, over the core and edge. $S = n n_n (\sigma v)_{ion}$ is the ionization particle source, with n_n being the neutral density and $(\sigma v)_{ion}$ being the ionization reactivity.

The main effect of coupling the density and temperature perturbations on the density limit for radiative collapse of the temperature profile is represented by the $2yf_z \langle gL_z \rangle$ term in the numerator of the first factor in Eq. (2.7). Since L_z is generally much larger in the interval where J_0 is negative (the cooler mantle and edge of the plasma), the $\langle gL_z \rangle$ part of this term will generally be negative. The term $2yf_z \langle gL_z \rangle$ will be positive, increasing the density limit, for $y \equiv \bar{n}_0 / \tilde{T}_0 < 0$. The value of y given by Eq. (2.12) will usually be negative if a and b of Eq. (2.13) have the same sign. Fueling may effect the

density limit, since y depends on the fueling source S . However, the dependence on S is too complex to provide general conclusions [2.18].

Edge cooling terms due to the atomic physics effects of charge-exchange, ionization and elastic scattering can be included [2.18] in Eqs. (2.7) and (2.13) by

$$\text{replacing } \frac{f}{z} \frac{L}{z} \text{ with } \frac{f}{z} \frac{L}{z} + f_0 \left(\frac{3}{2} T \left((\sigma v)_{cx} + (\sigma v)_{el} \right) + E_{ion} (\sigma v)_{ion} \right).$$

Equation (2.7) defines a radiative collapse density limit n_{RC} . Because a radiative collapse of the temperature usually leads to a disruption, Eq. (2.7) may also be considered a disruption density limit. It is convenient to define a radiative collapse index

$$RCI = n_{av}^{exp} / n_{RC} \quad (2.14)$$

where n_{av}^{exp} is the experimental volume average density.

Equations (2.7)-(2.14) have been found to predict radiative collapse in agreement with experimental observation in a couple of shots in DIII-D [2.26].

CHAPTER III

MEASUREMENTS IN TEXTOR

3.1 Introduction

TEXTOR, Tokamak Experiment for Technology Oriented Research, became operational in January 1983 at the Institut für Plasmaphysik, Forschungszentrum Jülich in Germany [3.1]. TEXTOR was designed and built as a test bed for the investigation and control of particle and power exhaust under conditions close to those of a fusion reactor. The two main thrusts [3.2] of the associated research program are: 1) The properties of the plasma edge, including the plasma composition and the effects of impurities; 2) The physical processes involved with the interaction of edge plasma with the wall and limiter materials.

TEXTOR is a medium size tokamak with a major radius of $R_0 = 1.75$ m. TEXTOR has a circular cross-section with a nominal minor radius determined by a toroidal belt limiter of $|R-R_0| = 46.0$ cm. Inside the vessel, a liner is installed with a radius of 55.0 cm. A poloidal cross-section [3.3] of TEXTOR is shown in Figure 3.1. On the low field side (LFS), 45° below the midplane, the ALT-II toroidal belt limiter is installed. The ALT-II pumped limiter consists of eight graphite blades, each 150 cm long, 28 cm in width. On the high field side (HFS) at $R-R_0 = -49.8$ cm, a toroidal bumper limiter is

mounted on the liner. Also shown are the retractable poloidal main limiters with which the minor radius can be reduced to $|R-R_0| = 42.0$ cm. All limiters are made of carbon.

Thermal expansion of the in-vessel components must be accounted for in determining the plasma size and position. The operational vessel and liner temperatures are 150°C and 300°C, respectively. The support structure of the poloidal limiter is rigidly attached to the transformer yokes of TEXTOR and does not move when the vessel is heated. The ALT-II limiter moves outward with increasing temperature. At a liner temperature of 300°C with retracted poloidal limiters, the radius of the last closed flux surface is $|R-R_0| = 46.3$ cm. Thermal expansion of the liner moves the bumper limiter to $R-R_0 = -49.3$ cm, 3.0 cm from the LCFS [3.4].

The auxiliary heating systems of TEXTOR consist of two neutral beam injectors, which are tangentially set up in co- and counter-directions to the plasma current, and two ICRH antennas. A top view [3.5] of the TEXTOR heating system is shown in Figure 3.2.

During 1993-94, TEXTOR was upgraded for long-pulse operation (to a pulse length of ~ 10 s from ~ 3 s), by providing a new ohmic heating coil able to deliver a larger flux swing. The upgraded machine is called TEXTOR-94 to distinguish it from the machine in its earlier period. Since long-pulse operation is not a factor in the density limit, the machine will be referred to simply as TEXTOR.

3.2 TEXTOR Diagnostics

The plasma core electron temperature profile $T_e(R)$ is measured by a ten channel second harmonic X-mode Electron Cyclotron Emission (ECE) radiometer. Near the density limit, however, the central density may exceed the cut-off for the second harmonic. In this case, additional channels [3.6] using third harmonic frequencies can measure $T_e(R)$ from $1.89 \leq R \leq 1.99$ m. The core electron density is measured with a nine channel HCN interferometer.

Edge electron temperatures and densities are measured with helium beams at different poloidal locations [3.4]. Thermal He-beams can be installed on the low field (LFS) and high field side (HFS) at the midplane and at the bottom (BOT), and a supersonic He-beam can be mounted at the top of the vessel. An oblique view of the He-beams (except the BOT thermal beam) is shown in Figure 3.3a [3.4] and a schematic view in a poloidal cross-section is shown in Figure 3.3b [3.7]; however, the He-beams in TEXTOR are actually located at somewhat different toroidal positions.

All He-beams are observed nearly perpendicular with radial and temporal resolutions of 1.2 mm and 100 ms over the whole discharge. A flux of $2\text{--}5 \times 10^{18}$ He-atoms/s is produced by effusive sources at the LFS and HFS. The supersonic He-beam on top of TEXTOR has a flux of only $\sim 5 \times 10^{16}$ He-atoms/s, but its neutral density (1×10^{16} – 1×10^{17} m⁻³) is comparable to the effusive sources due to its very low divergence. It is important to note that the lower the amount of injected He, the lower the intensity of the background light from recycled He [3.4].

In order to determine the n_e - and T_e -profiles using thermal He-beams, the line intensity ratios of two transitions in the singlet ($\lambda_1 = 668 \text{ nm}$, $\lambda_2 = 728 \text{ nm}$) and of one transition in the triplet system ($\lambda_3 = 706 \text{ nm}$) of He are measured. Above a minimum edge density of 10^{18} m^{-3} and a minimum temperature of 10 eV, T_e and n_e can then be calculated by comparing measured line intensity ratios with the equilibrium results of a collisional-radiative model. The accuracy of the model rests on the accuracy of the atomic rate coefficients. The line intensities of several other transitions were compared with the results of the collisional-radiative model and found to agree within $\pm 20\%$ [3.4]. There still exists a discrepancy in that the actual penetration depth of the thermal He-atoms is shorter than predicted by the model. At the given temperatures of the liner and vessel, the error bar is $(-2/+4) \text{ mm}$ for determination of the absolute radial positions. The electron temperatures and densities are given as accurate to within $\pm 20\%$ [3.4].

Background light from recycled He or from the plasma itself can have a significant effect on the evaluation of the edge profiles. In Figure 3.4 [3.4], the measured radial profiles of the λ_1 , λ_2 and λ_3 emission lines on the LFS are shown. The He-beam should be completely ionized at $R - R_0 = 40 \text{ cm}$, yet some signals still have a significant value. This background light, mostly from higher ionized impurity lines, is dependent on the plasma conditions and drops to nearly zero at the LCFS. An approximation used to subtract the background light is a straight line, from the measured value at $R - R_0 = 40 \text{ cm}$ to its intersection at $R - R_0 = 47 \text{ cm}$ with a horizontal line representing the dark current of the diode array camera. The dark current is the null response of the diode array.

MARFEs are detected by measuring the H_{α} radiation with a tangentially viewing CCD camera and by measuring the C II (426.7 nm) radiation directly at the bumper limiter surface. A mirror diagnostic scanning the whole poloidal cross-section allows the C-III (229.6 nm), C-IV (580.5 nm) and C V (227.1 nm) emission lines to be determined. The MARFE radiation can be quantified by measurements with a 34 channel bolometric diagnostic, using tomographic reconstruction methods. The total radiated power can also be determined. Z_{eff} can be measured using the visible bremsstrahlung, or by means of charge exchange recombination spectroscopy (CXRS), from which the concentration of low-Z impurities (neon, oxygen, carbon) may be determined [3.3].

The ion temperature in the edge [3.3] can be measured by a CXRS diagnostic [3.8] with a scanning mirror. However, the time resolution of this diagnostic is not sufficient to get a temperature profile of the ions for a density ramp up. A steady state companion discharge at a density near that at which the MARFE appears is performed with the mirror scanning the edge. In the MARFE discharge, the scanning mirror is fixed to look at one radial position for comparison with the companion discharge [3.3].

Emission spectroscopy [3.9] was used to determine the particle fluxes of deuterium, carbon and oxygen simultaneously from the ALT-II limiter and of deuterium and carbon from the bumper limiter. The various particle fluxes were measured by means of an interference filter and a spectrometer, which serves for 2D-recordings (spectral and spatial) either photographically or in combination with a CCD-image intensifier system. The observation volumes are chosen in such a way that the emitted intensity is integrated

both in the line of sight and in the radial direction. For the respective fluxes the following filters are used: H_{α}/D_{α} ($\lambda = 656.1$ nm, FWHM = 4.0 nm), O I ($\lambda = 844.6$ nm, FWHM = 5.0 nm), O II ($\lambda = 441.5$ nm, FWHM = 3.4 nm), C I ($\lambda = 909.5$ nm, FWHM = 1.0 nm), and C II ($\lambda = 426.9$ nm, FWHM = 3.5 nm). The CCD video camera has a tangential view, shown in Fig. 3.5 [3.10]. The view includes an entire ALT-II blade, half of one ICRH antenna pair, the top and bottom limiters and two of the three gas feeds used for external fueling. The outboard poloidal limiter and the inner bumper limiter cannot be seen simultaneously, but the view can be adjusted to include one or the other.

The ALT-II blade is also viewed from above by a calibrated photodiode. The diode measures emission from a rectangular region 40 cm long poloidally and 5.7 cm wide toroidally, focused on the center of the blade. This measurement is used for calibration of the camera data. Since the diode view integrates poloidally across the blade, the measurement provides a brightness per unit toroidal length.

Not all neutrals born at the limiter are ionized in front of the limiter, some can travel a significant distance parallel to the LCFS. In TEXTOR, this creates a halo [3.10] around the limiter belt, extending over a substantial fraction of the plasma surface.

The photon fluxes were converted into particle fluxes as described in Ref. 3.11. The deuterium flux has been corrected for molecular contribution by multiplying by 1.5, and the error in the deuterium flux was estimated at $\pm 40\%$ [3.12]. The halo flux around the ALT-II limiter was estimated at 30-50% of the ALT-II limiter flux itself [3.12-3.13].

3.3 The TEXTOR Plasma Edge

The electron density and temperature edge profiles are the result of the interaction by transport and atomic physics processes of the core with the material surfaces. The processes at the plasma edge constitute a highly non-linear system [3.14]: the production of impurities by different release mechanisms, the penetration of main ion and impurity neutrals into the plasma edge and the transport of main and impurity ions into and inside of the confined volume.

The edge electron temperature affects the energy of the impinging ions and thus the sputtering yields via the sheath potential. The impurities released from the limiters penetrate into the plasma edge, are ionized and affect the heat flux balance by their line radiation, causing a reduction of electron temperature [3.15].

3.3.1 Poloidal Asymmetries in Data

The radial decay lengths in the SOL of TEXTOR increase with increasing distance along the magnetic field line from a limiter, reaching a maximum at the stagnation point [3.16]. Poloidal asymmetries in a tokamak are produced by the $\mathbf{E} \times \mathbf{B}$ drift [3.4,3.7,3.17] and by the $\mathbf{B} \times \nabla p$ diamagnetic drift. For higher density discharges [3.18-19] or for higher neutral beam heating power [3.19], a shoulder appears in the LFS density profiles. Asymmetries of the plasma can also be caused by horizontal and vertical shifts of the plasma column.

Radial profiles of n_e and T_e at three poloidal beam positions in discharge 77536 are shown in Figure 3.6 a) and b) [3.4]. The line averaged central density was $3 \times 10^{19} \text{ m}^{-3}$. Although the plasma has been aligned in such a way that plasma shifts can be excluded, the profiles vary poloidally. The higher n_e and lower T_e on the HFS might be influenced by the nearby bumper limiter, which acts as a source of recycled particles or by the asymmetry of the heat flux. This development of asymmetries can be explained qualitatively by model calculations with 2-D two-fluid codes which consider the role of drift motions [3.17-19].

The formation of density shoulders can also be explained by drift effects. Drifts are induced by radial pressure gradients and electric fields in the boundary layer. The densities measured at the LFS and HFS with thermal He-beams are shown in Figure 3.7. Low density discharges exhibit smooth radial profiles whereas for high densities a density shoulder appears at the LFS. Neither the HFS density profiles nor temperature profiles at either positions exhibit shoulder formation with increasing density [3.18]. There is a similar effect with increasing neutral beam heating power as shown for the LFS in Figure 3.8. Again, at the HFS there are neither experimental nor numerical results which display any deviations from smooth radial decay [3.19].

3.3.2 Treatment of Shafranov Shift Effects in the Data

For toroidal equilibrium to exist in a tokamak, a vertical magnetic field is necessary. The magnetic flux surfaces are shifted outward, forming non-concentric circles in a poloidal cross-section. The Grad-Shafranov equilibrium equation must be solved for

the displacement of the center of the magnetic flux surfaces from the center of the bounding flux surface (LCFS), $\Delta(r)$. The displacement of the magnetic axis, $\Delta_0 = \Delta(0)$, is called the Shafranov shift. For high β tokamaks, Δ_0 is given by [3.20]

$$\Delta_0 = \frac{a \nu}{1 + (1 + 3 \nu^2)^{1/2}} \quad (3.1)$$

where $\nu = \epsilon \beta_p$, $\epsilon = a/R_0$ is the inverse aspect ratio and $\beta_p = 2\mu_0 \langle p \rangle / B_p^2$ is the poloidal beta.

In TEXTOR, the position signals for the horizontal feedback system come from the nine channel HCN-interferometer or from probing coils for the magnetic field mounted outside the liner. The first method of finding the horizontal position compares the line-integrated signals at two horizontally symmetric positions; however, the Shafranov shift must be considered [3.4]. The tokamak major and minor radii are fixed (except for thermal expansion) by the vessel and the active limiter. The plasma major and minor radii, however, may vary. If the vertical magnetic field is fixed to make the plasma major and minor radii approximately equal to the tokamak major and minor radii for “standard” TEXTOR parameters ($I_p = 350$ MA, $P_{aux} = 1.3$ -1.4 MW, $B_0 = 2.25$ T) then changes in the plasma parameters (e.g., heating power) will change the Shafranov shift and hence the plasma major and minor radii. This will also affect the diagnostic measurements since the location of the LCFS will change.

A model of the TEXTOR geometry with tokamak major radius R_0 and minor radius a is shown in Figure 3.9. The ALT-II limiter is modeled as a point. The plasma

major and minor radii are R_0' and a' , respectively. The Shafranov shifts for the standard and actual plasma parameters are Δ_0 and Δ_0' , respectively. From this simple model, the constraint equations are

$$R_{\text{mag}} = R_0 + \Delta_0 = R_0' + \Delta_0' \quad (3.2)$$

and

$$a' = \sqrt{(a / \sqrt{2})^2 + (a / \sqrt{2} + \Delta_0' - \Delta_0)^2} \quad (3.3)$$

where R_{mag} is the position of the magnetic axis with respect to the center of the torus.

The positions of the LCFS at the midplane of the HFS and LFS are

$$R_{\text{LCFS}}^{\text{HFS}} = R_0' - a' \quad (3.4)$$

and

$$R_{\text{LCFS}}^{\text{LFS}} = R_0' + a' \quad (3.5)$$

Measurements taken by diagnostics installed at the LFS and HFS in TEXTOR must be adjusted to compensate for the actual plasma position. However, the calculated values of the Shafranov shift rely on a simple approximation, $\Delta_0 \text{ (cm)} = 2.2 + 6.0\beta_p$, since equilibrium calculations are not available for TEXTOR. The uncertainty in the horizontal position of the magnetic axis is about $\pm 0.5 \text{ cm}$. This makes the uncertainty in the location of the LCFS on the HFS about $\pm 1 \text{ cm}$ [3.12].

The procedure used to determine the flux surface geometry in TEXTOR is outlined in Reference 3.21. Using the HCN density profile measurements (n_e is considered

constant on a flux surface), the phase shift is determined at nine radial positions. Spline fitting gives the phase shift profile and hence, the density profile, by Abel inversion (Gottardi method), assuming cylindrical symmetry on each flux surface. $R(\rho)$ and ρ are then calculated at several positions and least squares fitted by a law including the Shafranov shift

$$R(\rho) = R_{\text{mag}} - \Delta'_0 (\rho / a')^{\alpha_R} \quad (3.6)$$

as shown in Figure 3.10.

3.3.3 Correction of Gradient Scale Lengths for Shafranov Shift

The Shafranov shift will compress the flux surfaces on the LFS and expand them on the HFS. The gradients of the flux surface quantities (e.g., density and temperature) must be adjusted for the Shafranov shift. We quantify variation of the flux surfaces by using the following zero-order solution of the Grad-Shafranov equation for high- β tokamaks [3.20]

$$\psi_0(\rho, \theta) = \frac{a^2 B_0^2}{2q_*} \left[\rho^2 - 1 + \nu \left(\rho^3 - \rho \right) \cos \theta \right] \quad (3.7)$$

where $\rho = r / a$, $\nu = \beta_t q_*^2 / \varepsilon$, $q_* = 2\pi a^2 B_0 / \mu_0 R_0 I_0$, $\varepsilon = a / R_0$,

$\beta_t = 2\mu_0 \langle P \rangle / B_0^2$, and θ is the poloidal angle referenced to the LFS midplane.

The gradient scale lengths can be expressed in terms of the partial derivative of ψ_0 with respect to r for $X = T, n$ as

$$L_x = \lambda_x \equiv \left(-\frac{1}{X} \frac{\partial X}{\partial r} \right)^{-1} = \left(-\frac{1}{X} \frac{\partial X}{\partial \psi} \frac{\partial \psi}{\partial r} \right)^{-1} \quad (3.8)$$

The gradient scale length measured at any poloidal position θ_m can be converted to a gradient scale length at any other poloidal position θ by

$$\lambda_x(\theta) = \lambda_x(\theta_m) \frac{\partial \psi(\theta_m) / \partial r}{\partial \psi(\theta) / \partial r} \quad (3.9)$$

where from equation (3.7) we obtain

$$\frac{\partial \psi_0}{\partial r} = \frac{aB_0}{2q_*} \left[2\rho + \nu \left(3\rho^2 - 1 \right) \cos \theta \right] \quad (3.10)$$

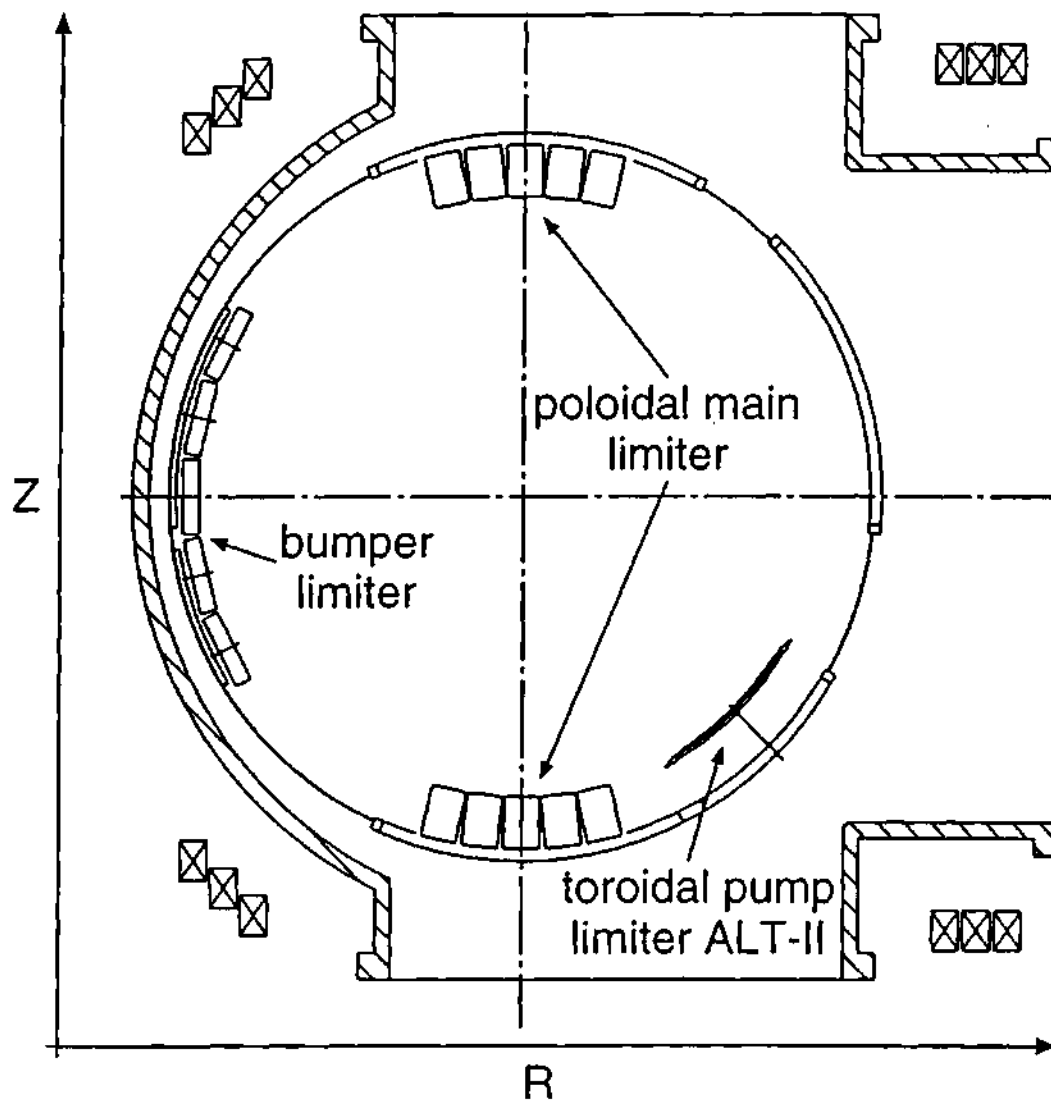


Figure 3.1 Poloidal cross-section of TEXTOR with its limiters.

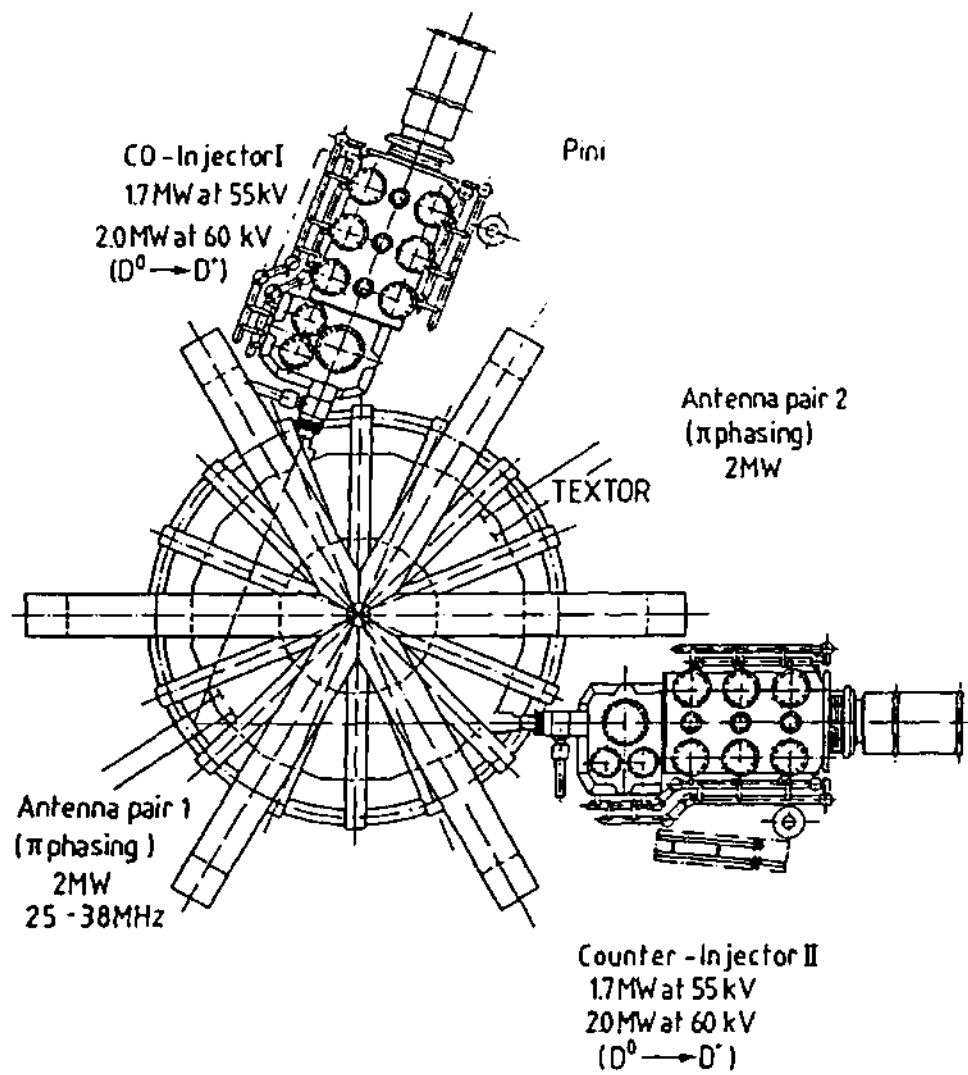


Figure 3.2 The TEXTOR heating system, with 2 antenna pairs (ICRH) and 2 neutral injector plug-in (PINI) systems (one co- and one counter-injector).

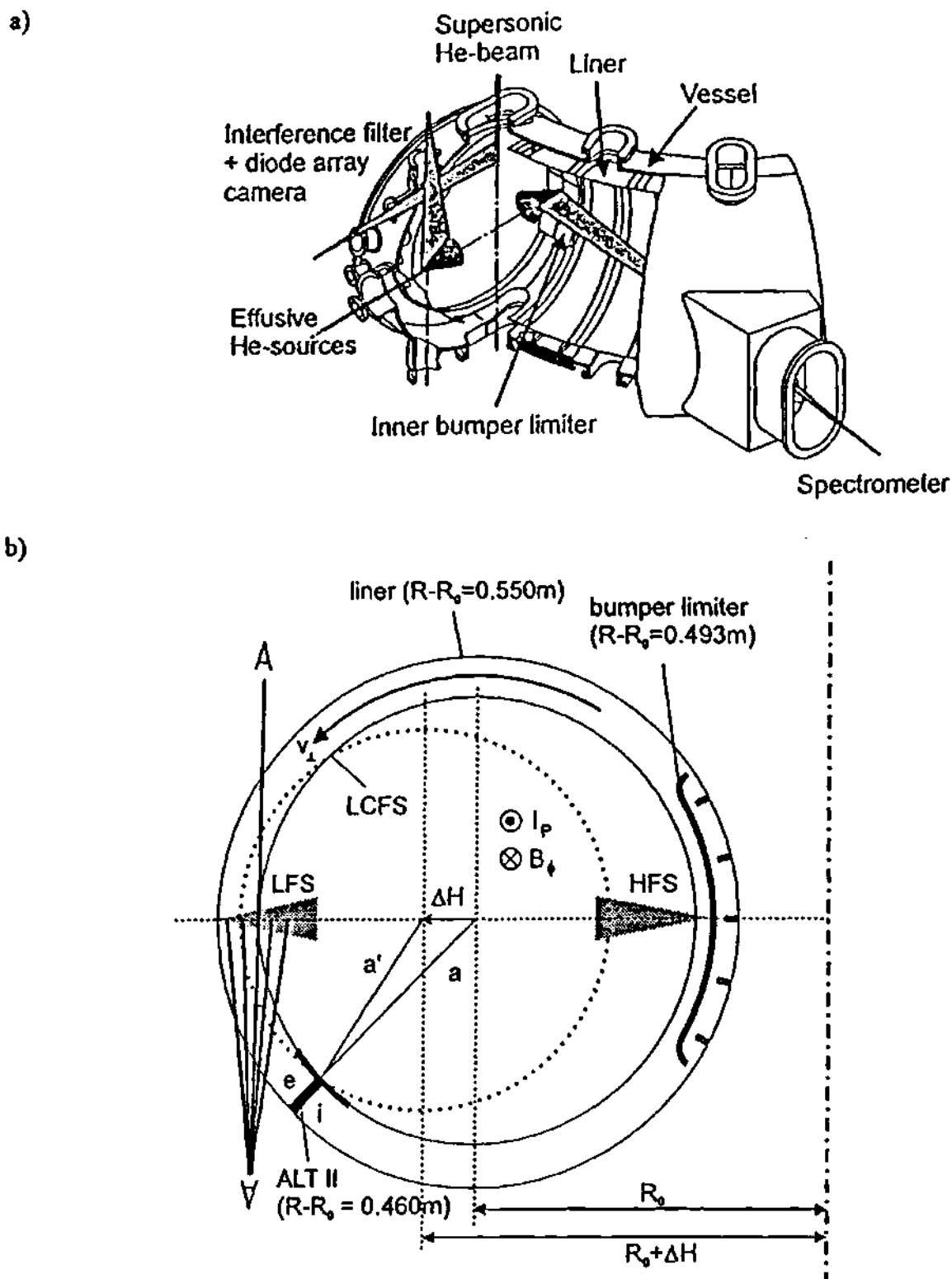


Figure 3.3 a) View of the He-beam sources and their respective observation systems and b) schematic view in a poloidal cross-section with Shafranov shifted LCFS surface.

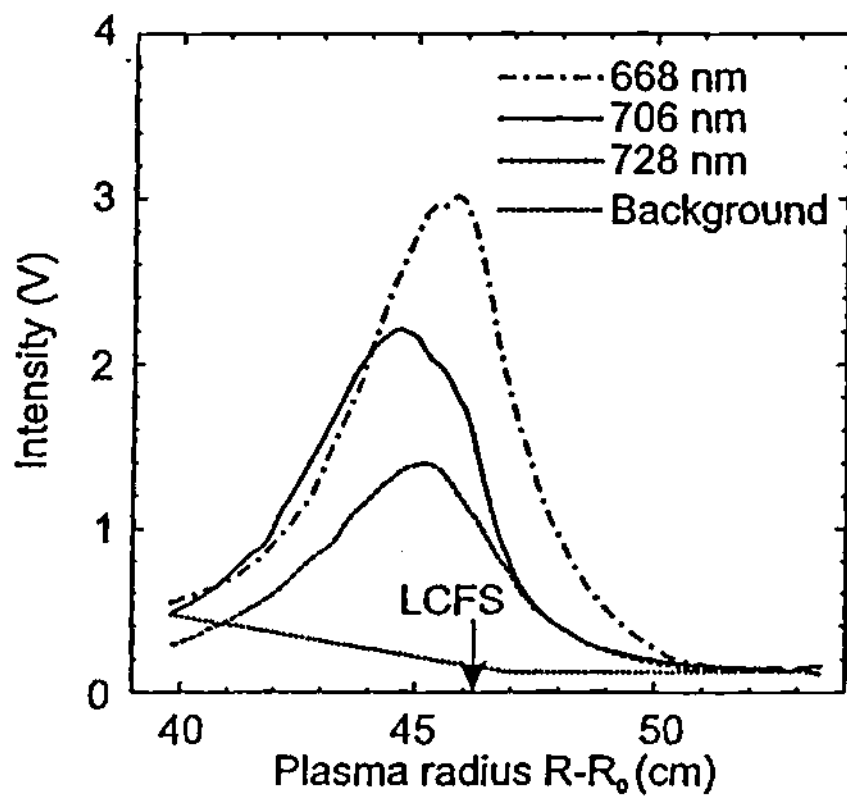


Figure 3.4 LFS radial profiles of the line intensities at $\lambda_1 = 667.8$ nm, $\lambda_2 = 728.1$ nm and $\lambda_3 = 706.5$ nm. The dotted line represents the subtracted intensity of the estimated background light.

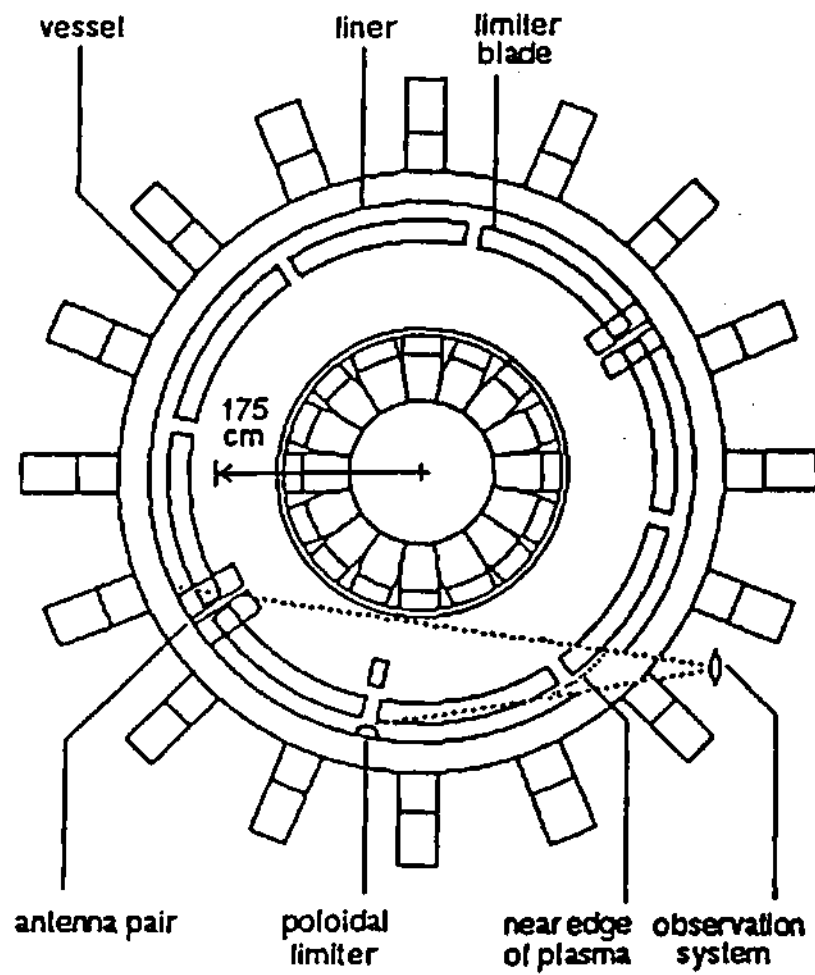


Figure 3.5 Top view of TEXTOR showing region visible to CCD camera.

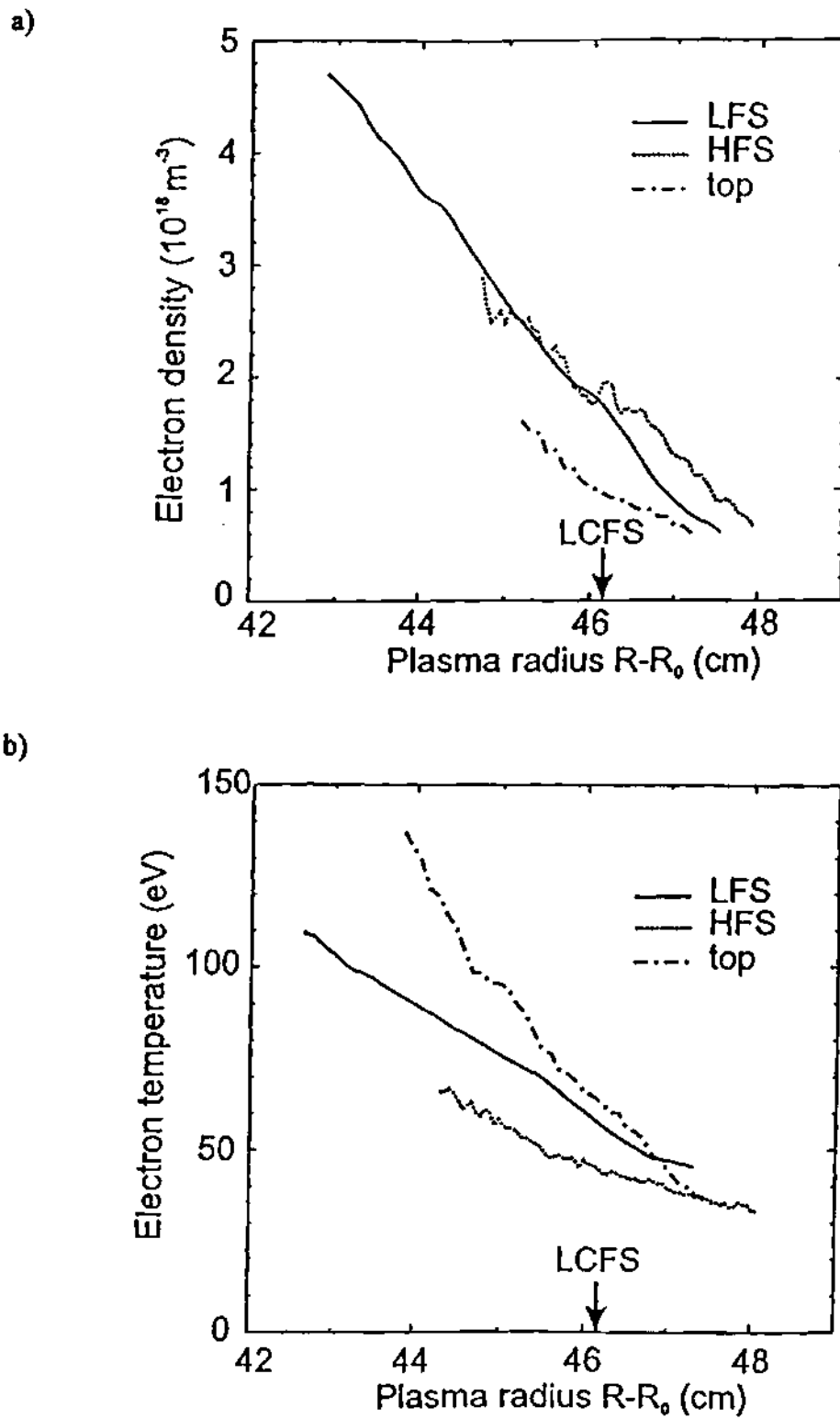


Figure 3.6 Radial edge profiles of a) n_e and b) T_e at three poloidal positions in shot 77536.

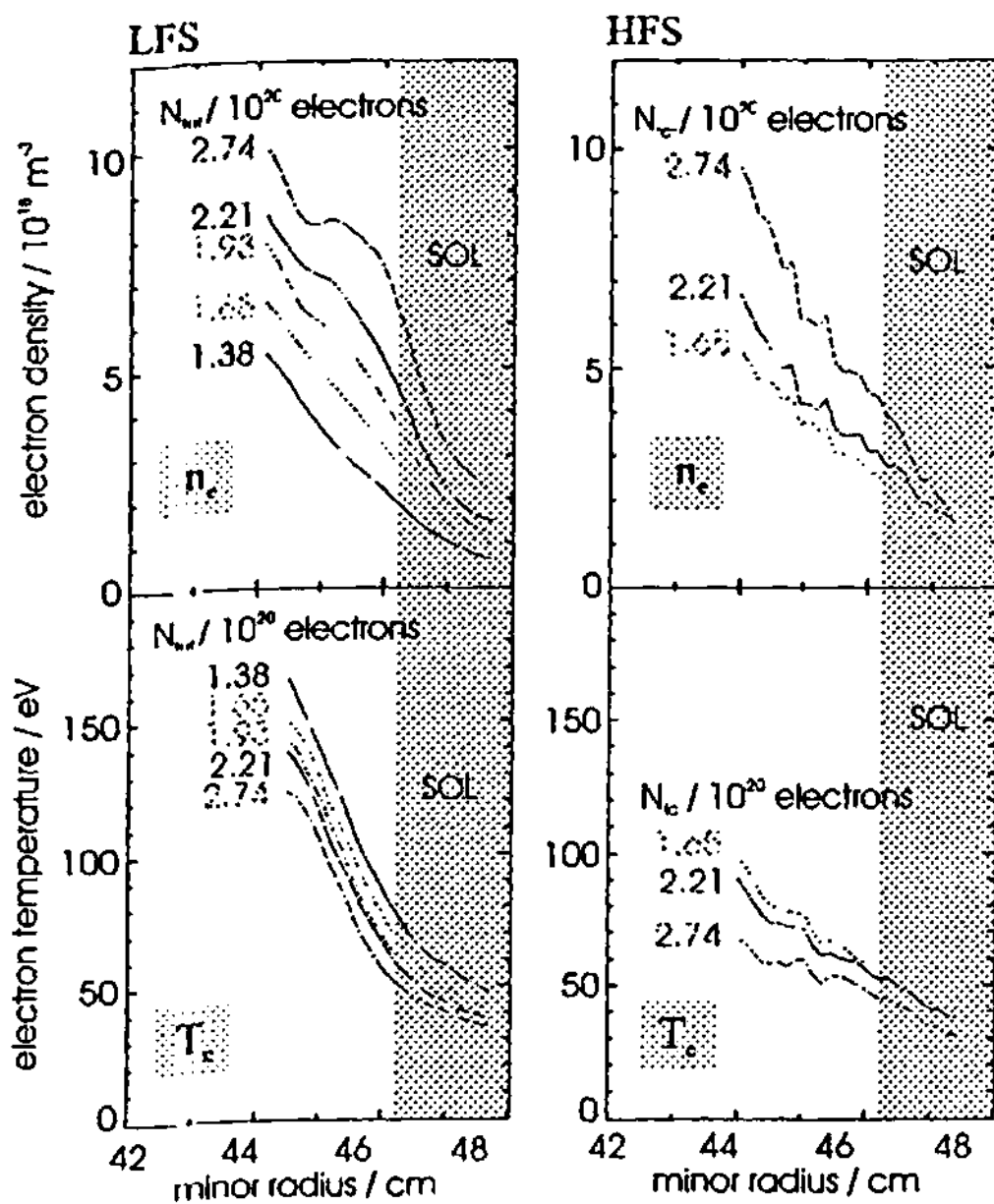


Figure 3.7 Measured density and temperature profiles at the LFS and HFS for different plasma densities. ($P_{\text{heat}} = 1.55 \text{ MW}$)

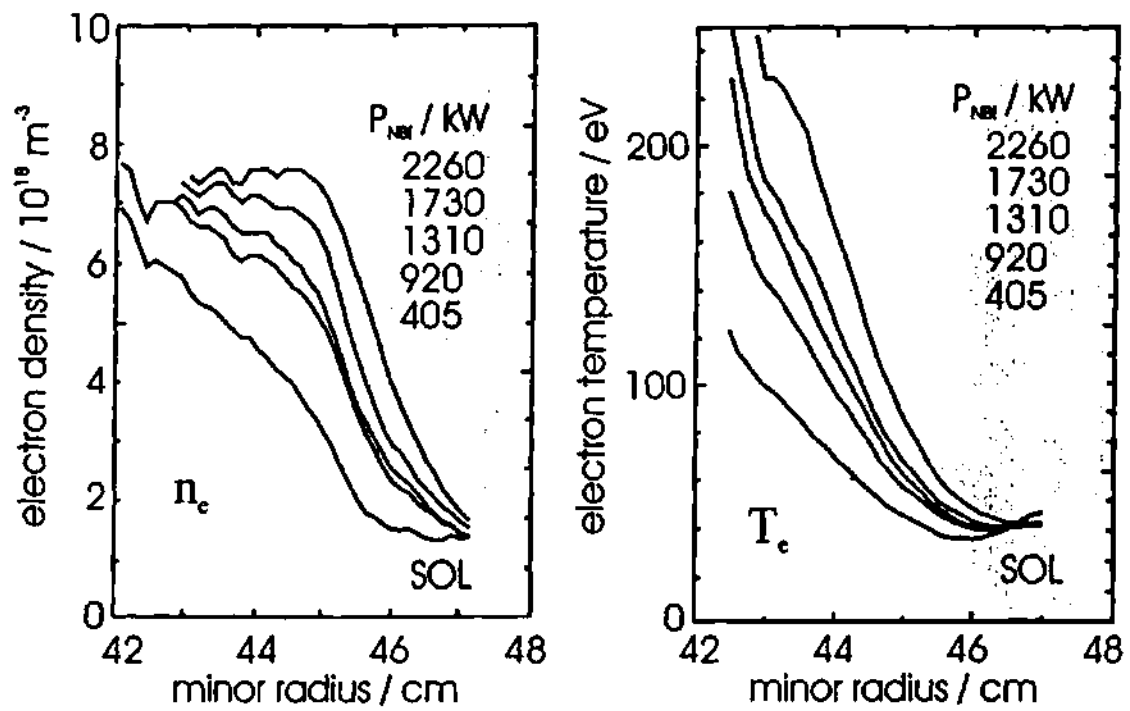


Figure 3.8 Density and temperature profiles measured at the LFS for different neutral beam heating power. (Line averaged central density $n_e = 3.9 \times 10^{19} \text{ m}^{-3}$)

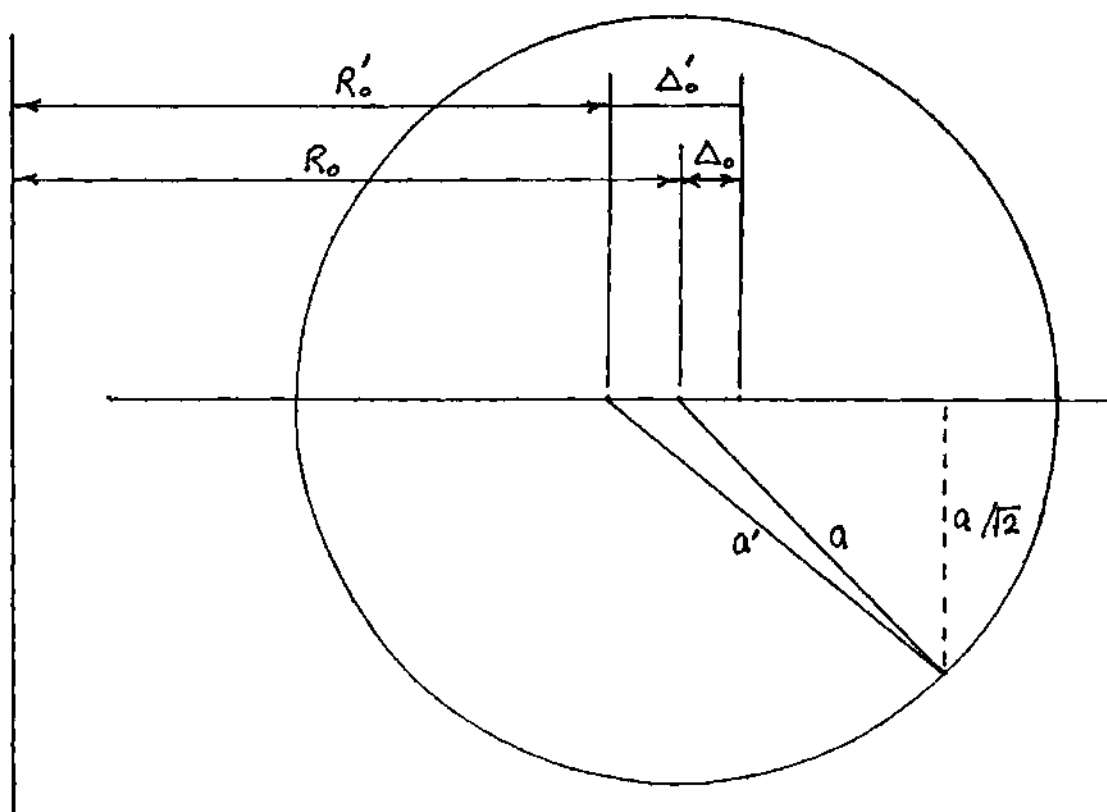


Figure 3.9 Model of TEXTOR tokamak and plasma geometry when limited by the ALT-II limiter.

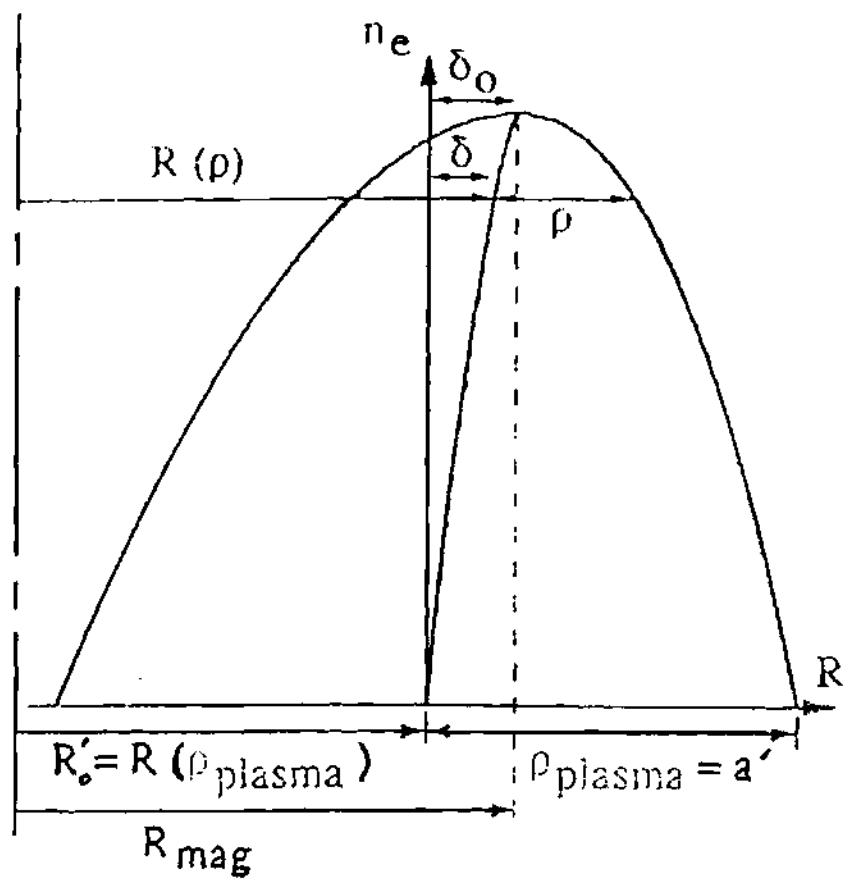


Figure 3.10 Schematic used to determine the plasma major radius $R'_0 = R(\rho_{plasma})$ and minor radius $a' = \rho_{plasma}$ on the basis of the electron density profile measurement.

CHAPTER IV

ANALYSIS OF MARFE ONSET IN TEXTOR

4.1 Introduction

Selected shots from TEXTOR which MARFEd were analyzed by comparison of the experimental edge conditions at MARFE onset with the edge conditions predicted for MARFE onset by the thermal instability theory discussed in Section 2.2.

The first shot analyzed, 80252, was performed in a boronized vessel. Then, a series of shots in a TEXTOR power scan (81531-81532, 81537-81539, 81573-81581) performed in a siliconized vessel over the 3rd and 4th of February, 1999, were analyzed. None of the shots were performed in a freshly conditioned machine, so the limiters were completely carbon. All shots were carried out in L-mode. All shots were limited by the ALT-II limiter, which was always pumped. The poloidal main limiters were withdrawn. There was continuous gas fueling until the MARFE occurred on the HFS. The shots were heated with neutral beam injection (H->D) with an energy of about 50 keV. For shots 81531-81532 ($P_{aux} = 0.61$ MW) and 81573-81581 ($P_{aux} = 0.90$ -1.47 MW), the direction of the neutral beam injection was parallel to the plasma current (co-injection), but for shots 81537-81539 ($P_{aux} = 1.73$ -2.33 MW) counter-injection was added to co-injection to obtain heating powers above 1.7 MW.

4.2 Use of Experimental Data in Evaluating the MI

The plasma edge electron temperatures and densities were measured by a thermal helium beam diagnostic [4.1] on the LFS midplane of TEXTOR as described in Section 3.2. The deuterium and carbon fluxes from the ALT-II and bumper limiters were obtained by measuring both spectral and spatial line intensity profiles as well as their integrated intensities [4.2]. All experimental data were provided by J. Rapp [4.3] of the TEXTOR team.

The temperature and density gradient scale lengths were obtained by graphically fitting the temperature and density profiles with exponential curves through pairs of data points inside the LCFS. The error in the gradient scale lengths were assumed to be approximately equal to the experimental error in the underlying variable.

Although the MARFEs occur on the inboard HFS of the plasma, the MARFE growth time is comparable to the time for ion diffusion along field lines from the LHS to the HFS of the plasma [4.4]. An ion will completely circumnavigate the periphery of the tokamak in the time it takes for a MARFE to grow and an electron will circumnavigate the periphery many times. Therefore, a poloidal average of the edge parameters was used to evaluate the MARFE density limit of Eq. (2.5). This required removing any density shoulders visible in the edge profiles and adjusting gradient scale lengths to take into account the expansion of the flux surfaces as discussed in sections 3.3.1 and 3.3.3, respectively. It should be noted that it is not always possible to detect a density shoulder.

The heat flux through the LCFS was calculated from the experimental P_{sep} divided by the plasma surface area $A_p \sim 32 \text{ m}^2$. The conductive fraction, f_{cond} , was assumed to be 0.9 based on analysis by the TRANSP code [4.5] of a representative TEXTOR discharge [4.3].

The experimental values of the deuterium fluxes were multiplied by 1.5 to account for D_2 molecules in the flux [4.3]. The deuterium fluxes from the bumper limiter and the ALT-II limiter were attenuated from their respective radial locations into the plasma edge. Similarly, the halo deuterium flux (assumed to be 40% of the ALT-II flux) was attenuated from $r = 50 \text{ cm}$ into the plasma edge. This attenuation was calculated with a 1-D neutral particle transport code based on the interface current balance method [4.6] and using the data of Ref. [4.7]. The background plasma density and temperature were calculated from the experimental values of the density and temperature at the LCFS exponentially attenuated outside the LCFS using the experimental values of their respective gradient scale lengths. The corresponding neutral deuterium density at the LCFS was divided by the experimental electron density at the LCFS to evaluate f_0 .

Experimentally based estimates of the ratios of incident carbon atom flux to incident deuterium atom flux from the bumper limiter and the ALT-II limiter were weighted by the relative magnitudes of the experimental values of the incident deuterium fluxes from the respective limiters to obtain an estimate of the carbon concentration. The carbon to deuterium flux ratio from the bumper limiter was multiplied by a factor of 0.8 to account for differences in the C-I and C-II light intensity. At the ALT-II limiter, the

energies of the atoms, rather than their velocities, were assumed to be equal [4.3], so the carbon to deuterium flux ratio was multiplied by the square root of the carbon/deuterium mass ratio.

The oxygen concentration in the plasma edge was taken to be 0.13 times the carbon concentration, based on the results of the CXRS diagnostic for shot 80251.

The ion temperature was not measured for these shots, but was constructed by assuming $T_i = 1.5T_e$ and $L_{Ti} = L_{Te}$, which corresponds to experimental data for ion temperature gathered for shot 80246.

For the purpose of calculating reaction rates, the cold neutral deuterium temperature was assumed to be 2 eV. Once collided, the neutral temperature was assumed to acquire the local ion temperature.

For the evaluation of Eq. (2.5) the average values of n and T and their gradient scale lengths over the region 1 cm inside the LCFS were used. These measured values were used: 1) directly to evaluate n and T and their gradient scale lengths that enter the theoretical predictions; 2) to evaluate the atomic physics reaction rates [4.7] and the coronal equilibrium impurity radiation function [4.8] in the edge plasma; and 3) to model the background plasma edge in the calculation of the neutral density in the plasma edge. The radiation function for carbon was modified [4.9] to include the effect of charge exchange and recombination [4.10,4.11] with 100 eV neutral hydrogen. The neutral and impurity concentrations needed to evaluate the theoretical expressions were calculated from measured data as described above.

4.3 Processing of Measured Data

The raw data for the edge profiles were processed to obtain the “experimental values” of n_e and T_e . Different versions of the processed data arise from different atomic data sets and different corrections for background light used in processing the raw data. We performed multiple versions of the analysis for each shot, corresponding to the different ways in which the raw data were processed.

The atomic data set used for the He-beam diagnostic was updated in February 2000. The old atomic data set gave higher temperatures and lower densities than the new atomic data set.

Furthermore, more than one procedure is in use at TEXTOR for correcting for background light. One background light profile (background 1) [4.3] consists of a three line profile: constant from $|R-R_0| = 40$ cm to 44 cm, a straight line from 44 cm to 47 cm and constant from 47 cm to 53.5 cm at the value of the dark current. Background 2 consists of a single straight line from the value of the 706 nm line at 40 cm to the value of the dark current at 53.5 cm. The two line background light profile shown in Figure 3.4 is referred to as background 3.

4.4 Analysis of Shot 80252

The critical plasma parameters for the onset of the MARFE in shot 80252 were measured for a plasma current of $I_p = 290$ kA and a toroidal magnetic field of $B_t = 2.25$ T. The plasma was heated by NBI at a power of $P_{aux} = 1.33$ MW. The ohmic and radiated

powers were 0.2 MW and 0.8 MW, respectively. A MARFE occurred at 2010 ms at a line-average density of $5.1 \times 10^{19} \text{ m}^{-3}$.

Just prior to the MARFE, the carbon concentration in the core plasma was 1% and Z_{eff} in the core was 1.5. At MARFE onset, the neutral hydrogen fluxes from the bumper and ALT-II limiter were $1.5 \times 10^{21} \text{ s}^{-1}$ and $1.7 \times 10^{22} \text{ s}^{-1}$, respectively. The carbon fluxes from the bumper and ALT-II limiter were $0.87 \times 10^{20} \text{ s}^{-1}$, and $0.75 \times 10^{20} \text{ s}^{-1}$, respectively. These lead to an estimation of the carbon and neutral concentrations in the plasma edge of 0.9% and 0.3%, respectively.

The Shafranov shift was determined to be 5.9 cm. Since the horizontal position control system uses this Shafranov shift as the reference value, no adjustment of the data measured at the LFS midplane was necessary for shot 80252.

Two versions of the edge profiles were used for the analysis of shot 80252. First, the old atomic data set and background 1 were used to obtain a temperature of 58 eV and a density of $6.5 \times 10^{18} \text{ m}^{-3}$ at the LCFS. The decay lengths were $\lambda_T = 3.7 \text{ cm}$ and $\lambda_n = 7.6 \text{ cm}$. The second version used the new atomic dataset and background 3 to obtain a temperature of 40 eV and a density of $9.5 \times 10^{18} \text{ m}^{-3}$ at the LCFS. The decay lengths were $\lambda_T = 3.9 \text{ cm}$ and $\lambda_n = 5.8 \text{ cm}$. Note that the temperature and density at the LCFS differ by ~50% between the two methods of processing.

The experimental parameters evaluated for conditions just prior to the MARFE onset were used to evaluate the MI. For shot 80252, the MI was 0.91 for the case of the old atomic data set and background 1, and the MI was 1.14 for the case of the new atomic

data set and background 3. We conclude from this result that MARFE onset is predicted reasonably well by Eq. (2.5) for shot 80252.

4.5 Analysis of Power Scan Shots

The plasma parameters at MARFE onset in the power scan were measured for a plasma current of $I_p = 350$ kA and a toroidal magnetic field of $B_t = 2.25$ T.

The neutral beam auxiliary heating power varied from 0.61 MW to 2.33 MW (co-injection up to 1.7 MW and a mixture of co- and counter-injection above that power).

The measured line-average density at MARFE onset is shown as a function of auxiliary heating power in Figure 4.1. The power scan actually consists of shots from three series of runs on different days. There is a trend of increasing MARFE onset density with P_{aux} over both the series of shots 81573-81581 ($P_{aux} = 0.90$ -1.47 MW) and the series of shots 81537-81539 ($P_{aux} = 1.73$ -2.33 MW), but the two series are offset. Similarly, the densities for the lowest power shots 81531-81532 ($P_{aux} = 0.61$ MW) are offset from the densities for the series 81573-81581 ($P_{aux} = 0.90$ -1.47 MW). The highest power shots (1.73-2.33 MW) were heated with counter- as well as co-injection, while all the lower power shots were heated with co-injection only, which could partially account for the offset between the series. However, this would not explain the offset between shots 81531-81532 ($P_{aux} = 0.61$ MW) and shots 81573-81581 ($P_{aux} = 0.90$ -1.47 MW) which are all heated with co-injection.

The total radiated power, P_{rad} , and the ohmic heating power, P_{oh} , plotted in Figure 4.2, also show different behavior in the three series of runs. P_{rad} increases in the power scan shots in a nearly linear trend. P_{oh} is seen to decrease slightly with increasing auxiliary power. However, shots 81531-81532 ($P_{\text{aux}} = 0.61$ MW) are somewhat above this trend while shot 81537 ($P_{\text{aux}} = 1.73$ MW) is somewhat below.

The particle fluxes at the ALT-II and bumper limiters are shown in Figures 4.3 and 4.4, respectively. Again, the fluxes in the co-injected series of shots below 1.7 MW exhibit a similar dependence as the co- plus counter-injected shots above 1.7 MW, but the two series are offset.

The temperatures and densities calculated at the LCFS using the three different corrections for the background and the two different atomic data sets are shown in Figures 4.5 and 4.6. The temperature and density gradient scale lengths just inside the LCFS using the same versions of the processed data are shown in Figures 4.7 and 4.8.

The MARFE Indices (MI) corresponding to the different processed versions of the measured data in Figures 4.5-4.8 are shown in Figure 4.9. By comparing Figures 4.7 and 4.9, it is clear that the MARFE Index is strongly correlated with the temperature gradient scale length, as is apparent from Eq. (2.5). For example, with the most recent processing procedure (new atomic data, background 3), the large λ_T of 7.2 cm for shot 81581 ($P_{\text{aux}} = 1.47$ MW) leads to a relatively large MI of 1.28 and the small λ_T of 3.6 cm for shot 81537 ($P_{\text{aux}} = 2.33$ MW) leads to a relatively small MI of 0.76. The offsets in measured particle fluxes may also contribute to the offsets in predicted MI.

Clearly, the procedure used to process the measured data has a substantial effect on the comparison between theory and “experiment”. Since the new atomic data set includes the latest values and more atomic transitions than the previous data set [4.12] and the background light profile 3 is the default profile [4.13], we will use these as the nominal values for subsequent analysis, except when otherwise noted.

The power scan experimental parameters are tabulated in Table 4.1. Using the new atomic data set and background light profile 3, the MARFE Index is evaluated in Table 4.2. For the first eight shots in Table 4.2, covering $P_{aux} = 0.61 - 1.73$ MW, the predicted MI is roughly at or slightly above unity, indicating conditions susceptible to MARFE onset. However, for shot 81539 ($P_{aux} = 2.33$ MW) the predicted MI is significantly less than one. As noted, this low value of MI is caused by the small value of λ_T at 2.33 MW. If this value of λ_T was similar to the others, then $MI \approx 1$ at 2.33 MW.

Table 4.1 Experimental parameters at MARFE onset for the TEXTOR power scan.

| Shot # | P_{aux} MW | P_{heat} MW | P_{sep} MW | P_{rad} MW | f_0 % | f_c % | λ_T^a cm | λ_n^a cm | T_e^b eV | n_e^b m^{-3} | δ_{LCFS} cm |
|--------|-----------------|------------------|-----------------|-----------------|------------|------------|---------------------|---------------------|---------------|---------------------|-----------------------|
| 81532 | 0.61 | 1.10 | 0.59 | 0.51 | 0.71 | 1.2 | 7.2 | 2.0 | 28 | 5.8e18 | 0.3 |
| 81573 | 0.90 | 1.25 | 0.68 | 0.57 | 0.65 | 1.4 | 6.6 | 3.9 | 31 | 6.6e18 | 0.1 |
| 81574 | 1.00 | 1.35 | 0.73 | 0.62 | 0.67 | 1.5 | 5.9 | 2.8 | 31 | 7.4e18 | 0.05 |
| 81575 | 1.14 | 1.50 | 0.86 | 0.64 | 0.60 | 1.5 | 5.5 | 3.0 | 32 | 7.4e18 | 0.0 |
| 81577 | 1.36 | 1.71 | 1.04 | 0.67 | 0.61 | 1.6 | 5.8 | 2.6 | 32 | 8.0e18 | 0.0 |
| 81579 | 1.42 | 1.77 | 1.08 | 0.69 | 0.60 | 1.6 | 6.1 | 2.4 | 34 | 8.7e18 | 0.0 |
| 81581 | 1.47 | 1.81 | 1.12 | 0.69 | 0.55 | 1.6 | 7.2 | 2.1 | 34 | 9.4e18 | 0.0 |
| 81537 | 1.73 | 2.00 | 1.20 | 0.80 | 0.70 | 1.4 | 6.2 | 2.2 | 35 | 8.9e18 | -0.1 |
| 81539 | 2.33 | 2.66 | 1.63 | 1.03 | 0.92 | 1.6 | 3.6 | 1.5 | 32 | 8.8e18 | -0.1 |

^a measured at $\theta_m = 0$, corrected by equation (3.8) to $\theta = \pi/2$ to obtain an “average”

^b LCFS at $\theta_m = 0$, after adjusting for the shift in horizontal position and removing density shoulders

These power scan shots span a significant range of edge parameters. The temperature and density gradient scale lengths ranged from 7.2 cm to 3.6 cm and from 3.9 cm to 1.5 cm, respectively. The temperature at the LCFS varied from 28 eV to 35 eV, while the density at the LCFS ranged from $5.8\text{e}18\text{ m}^{-3}$ to $9.4\text{e}18\text{ m}^{-3}$.

Table 4.2 Evaluation of the MARFE Index at MARFE onset for the TEXTOR power scan.

| | P_{aux} | \bar{n}_e | MI |
|--------|------------------|-----------------|------|
| Shot # | MW | m^{-3} | |
| 81532 | 0.61 | $6.1\text{e}19$ | 1.12 |
| 81573 | 0.90 | $5.1\text{e}19$ | 1.00 |
| 81574 | 1.00 | $5.6\text{e}19$ | 1.07 |
| 81575 | 1.14 | $6.0\text{e}19$ | 0.95 |
| 81577 | 1.36 | $6.1\text{e}19$ | 1.00 |
| 81579 | 1.42 | $6.2\text{e}19$ | 1.06 |
| 81581 | 1.47 | $6.3\text{e}19$ | 1.28 |
| 81537 | 1.73 | $5.8\text{e}19$ | 1.06 |
| 81539 | 2.33 | $6.7\text{e}19$ | 0.76 |

The MARFE Index is plotted versus P_{aux} in Figure 4.10 for conditions just before the MARFE onset and for conditions earlier in the shot well before the MARFE when the line-average density was $4.3\text{e}19\text{ m}^{-3}$, using the new atomic data and background light profile 2 for both set of calculations. While using the experimental parameters measured just prior to MARFE formation to evaluate the theoretical MARFE index generally led to a prediction of conditions for MARFE formation (i.e. MI somewhat greater than unity) except in the highest power shots, the predicted MI earlier in the shots were well below

unity. This result adds confidence to the prediction $MI > 1$ of MARFE onset when it was observed experimentally.

There is, of course, uncertainty in the raw measured data. The He-beam strength was less in the 81531-81532 ($P_{aux} = 0.61$ MW) and 81537-81539 ($P_{aux} = 1.73$ -2.33 MW) shots than for shots 81573-81581 ($P_{aux} = 0.90$ -1.47 MW). The error in the temperature was estimated [4.12] to be $\pm 50\%$ for shots 8153X and $\pm 30\%$ for shots 81573-81581. The error in density was estimated to be $\pm 20\%$ for all shots in the power scan [4.12]. The uncertainty in P_{rad} , which includes all the power radiated inside and outside the LCFS, was estimated to be $\pm 7\%$ [4.3]. The power crossing the separatrix is uncertain by $\pm 20\%$ [4.3].

The sensitivity of the predicted MI to uncertainties in the experimental parameters used to evaluate the MI was evaluated, using the new atomic coefficients and the background light profile 3. The maximum possible value of MI within the experimental uncertainties was evaluated with the deuterium flux increased by 40%, the impurity concentration increased by 20%, the density increased by 20%, the temperature set equal to 26 eV, the density gradient scale length reduced by 20% and the temperature gradient scale length increased by 30%. Similarly, we repeated the MI evaluation to obtain an estimate of the overall minimum possible MI. The results are plotted in Figure 4.11. The value of $MI = 1$ was within the experimental uncertainty for all shots in the power scan.

4.6 Summary

MARFE onset ($MI > 1$) was predicted for the experimental conditions measured just prior to MARFE onset in 8 out of 10 shots in the power scan using the best estimate, or nominal, values of the experimental parameters. A prediction of $MI \geq 1$ was within the experimental uncertainty for all shots in the power scan. MARFE onset was also predicted for shot 80252 which had a different plasma current and edge gradient scale lengths than the power scan shots. The experiment edge conditions varied over a significant range of values for some of the edge parameters which enter the prediction of MARFE onset. This relatively good agreement between theory and experiment indicates that MARFEs can be understood as radiative/atomic physics-driven thermal instabilities in the plasma edge and that Eq. (2.5) provides a good prediction of their onset in TEXTOR.

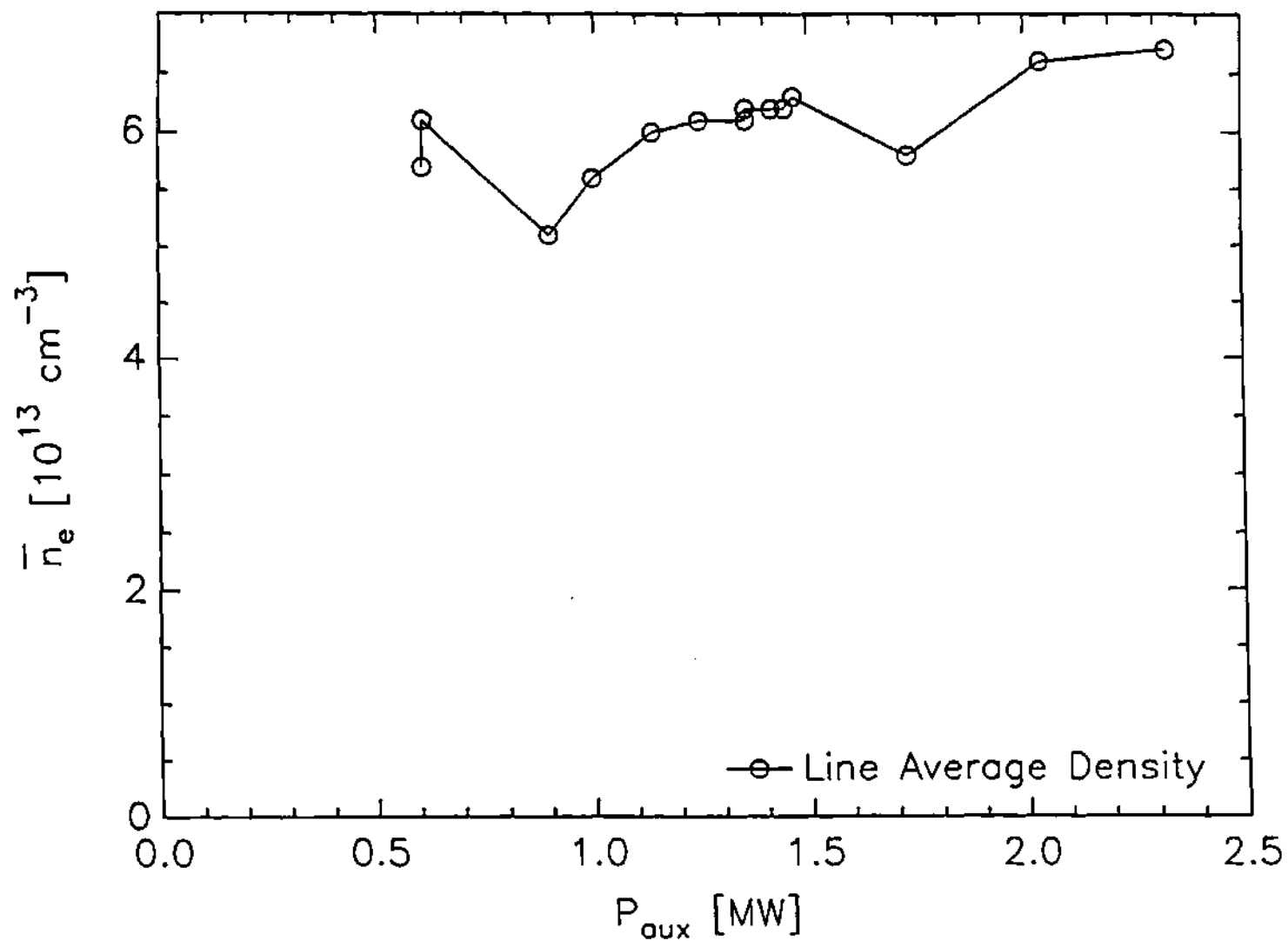


Figure 4.1 Experimental Line Average Density Versus Auxiliary Heating Power at MARFE Onset.

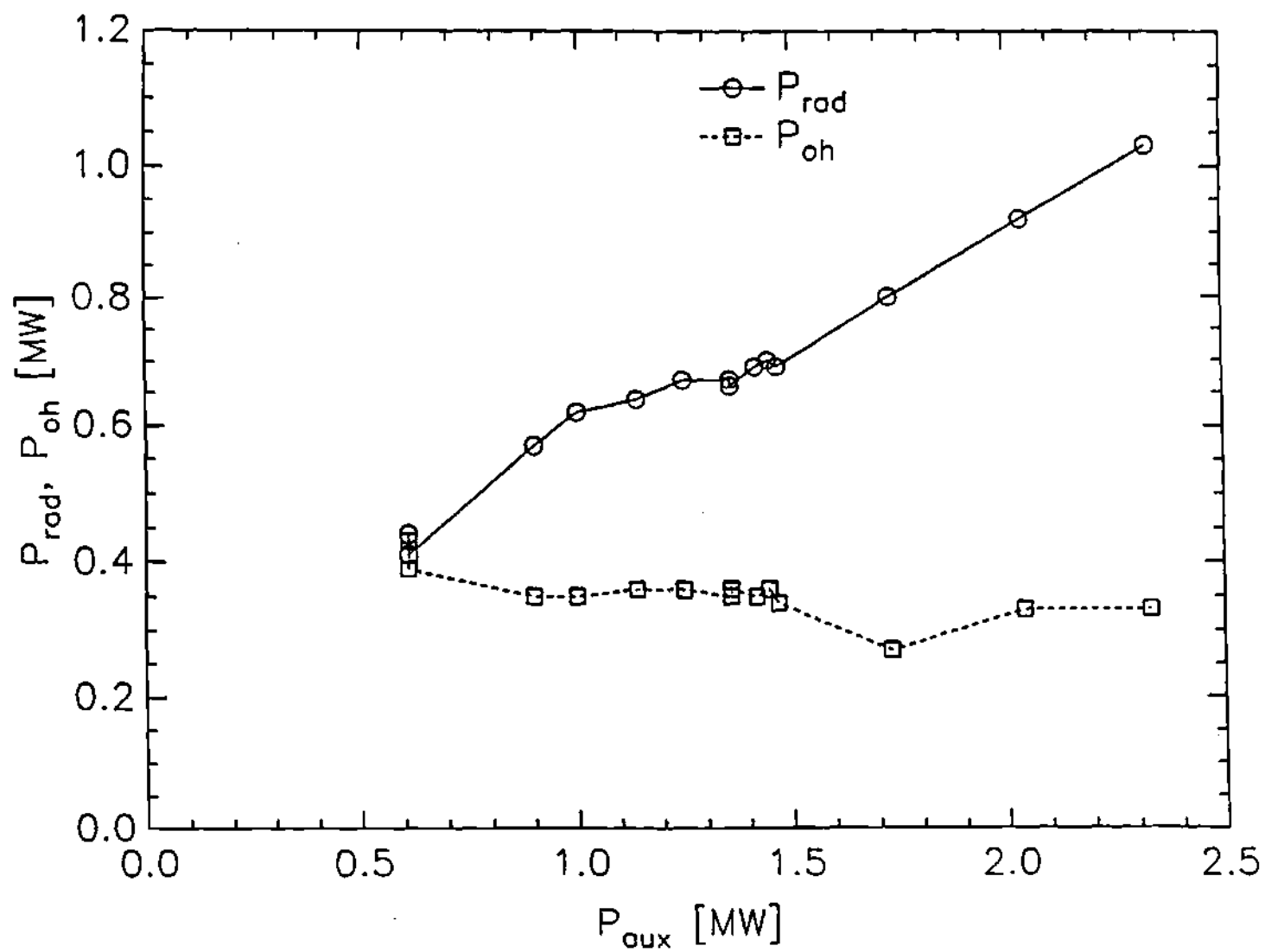


Figure 4.2 Experimental Radiated and Ohmic Heating Powers Versus Auxiliary Heating Power at MARFE Onset.

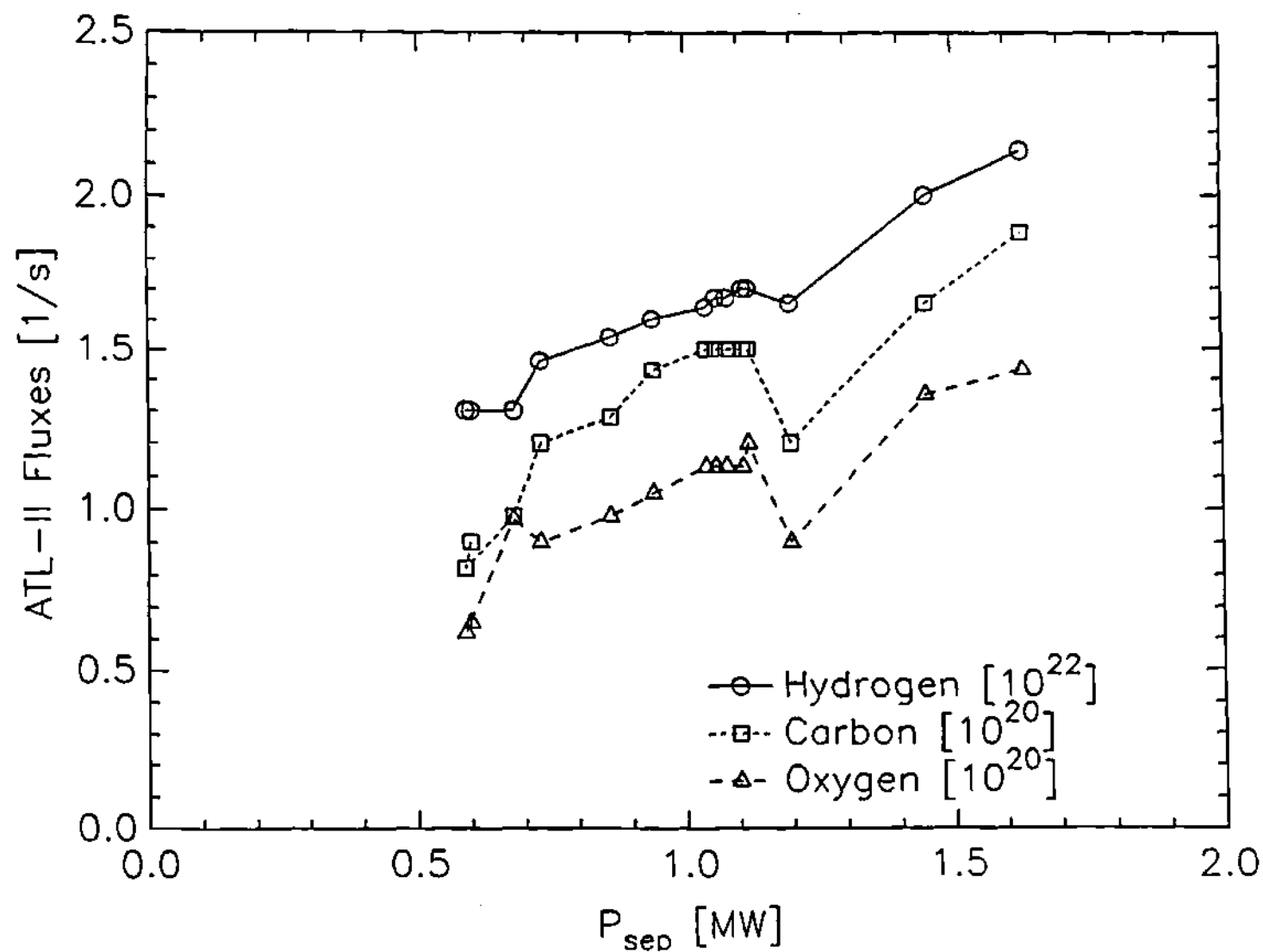


Figure 4.3 ALT-II Limiter Fluxes Versus Power Crossing Separatrix at MARFE Onset.

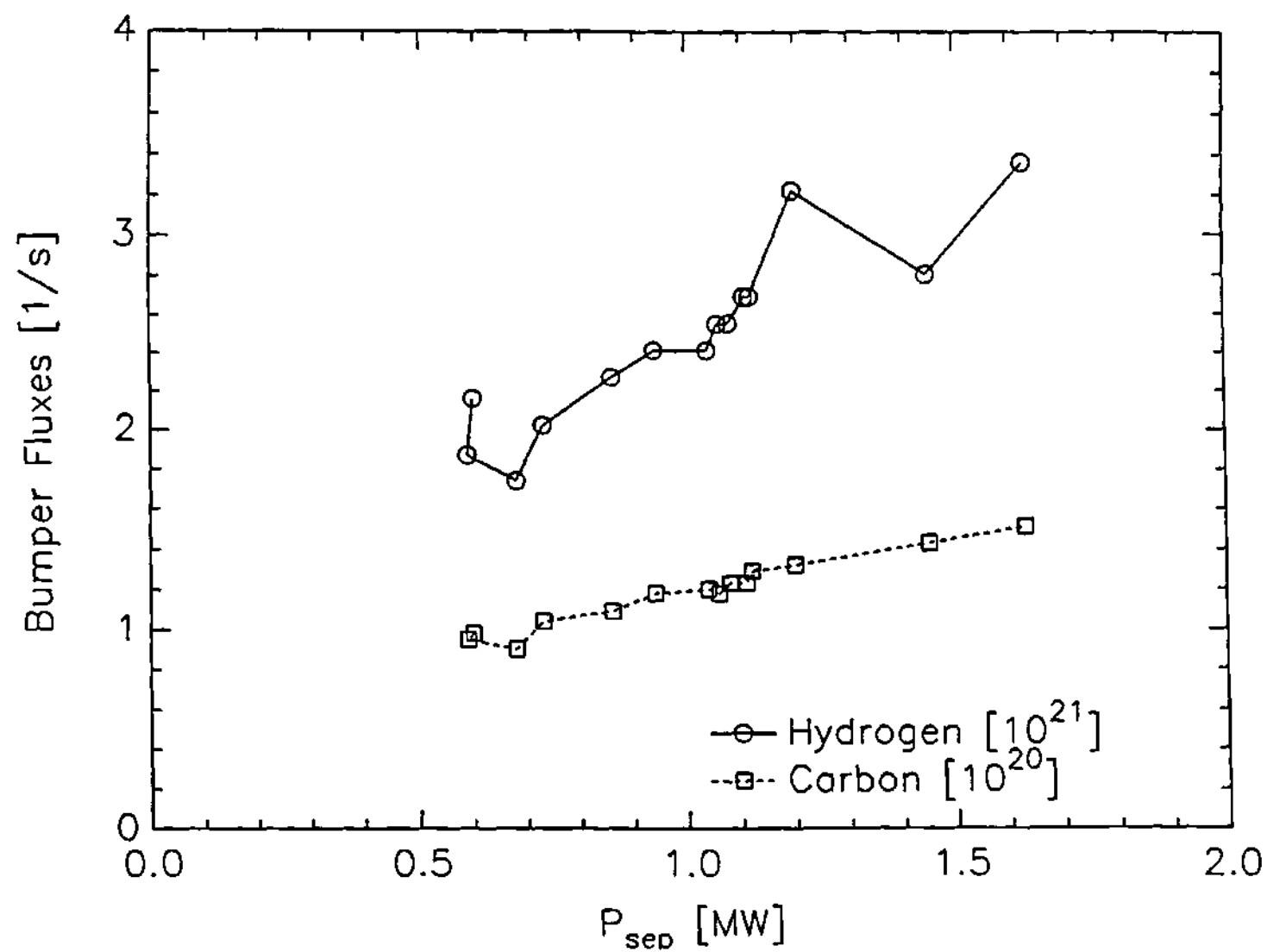


Figure 4.4 Bumper Limiter Fluxes Versus Power Crossing Separatrix at MARFE Onset.

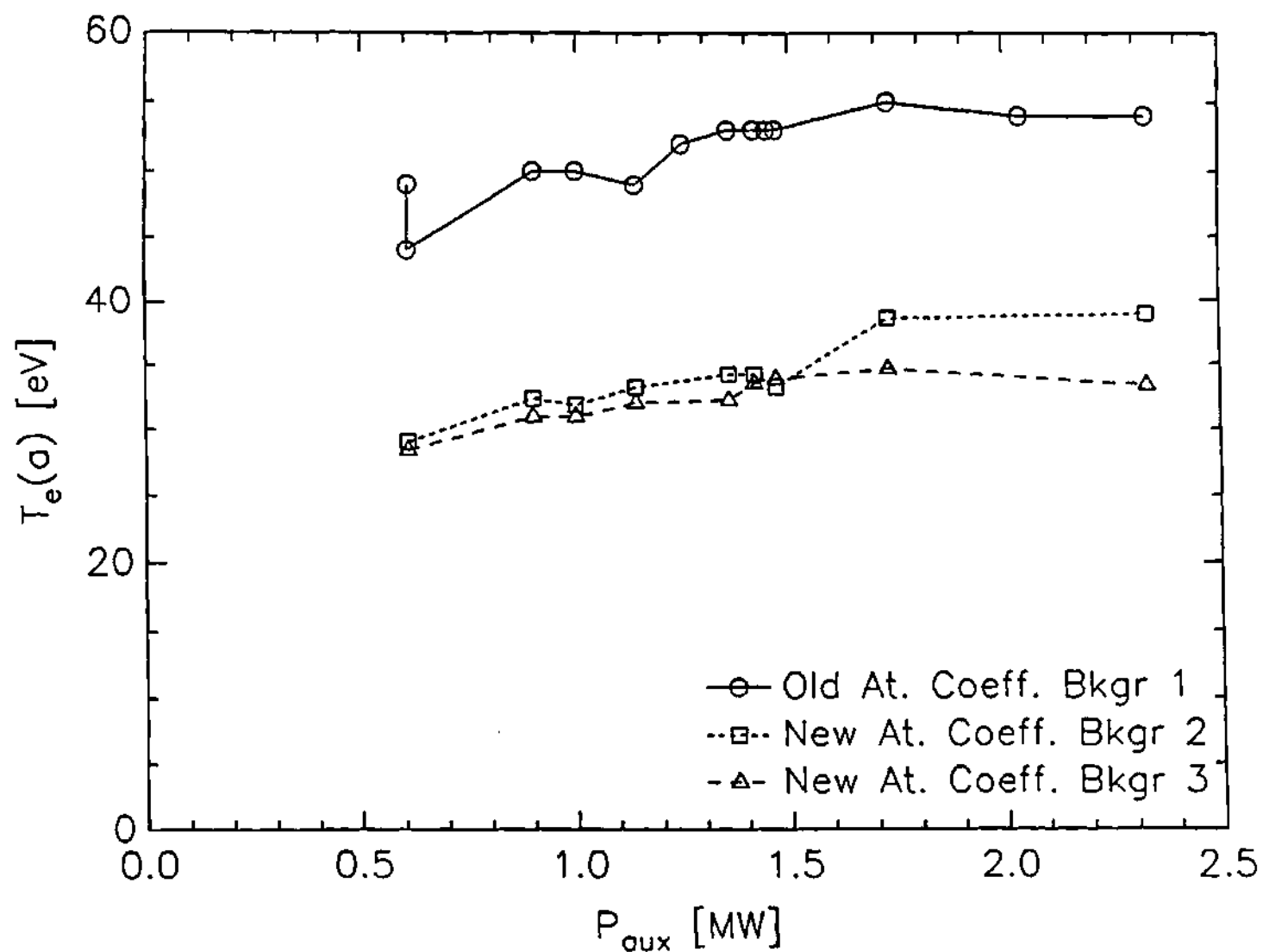


Figure 4.5 LFS Electron Temperature at the Separatrix Versus Auxiliary Heating Power with Different Data Processing.

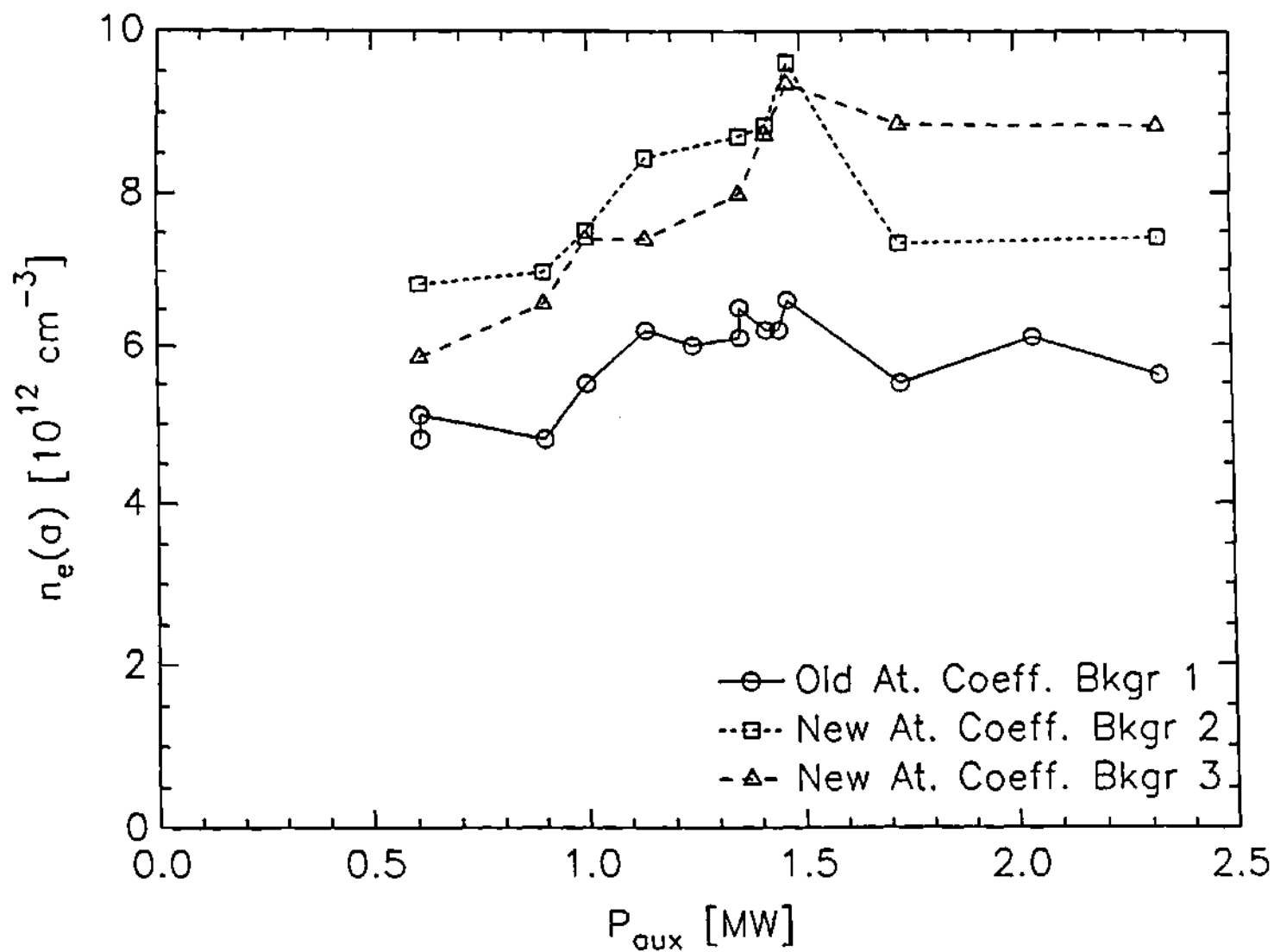


Figure 4.6 LFS Electron Density at the Separatrix Versus Auxiliary Heating Power with Different Data Processing.

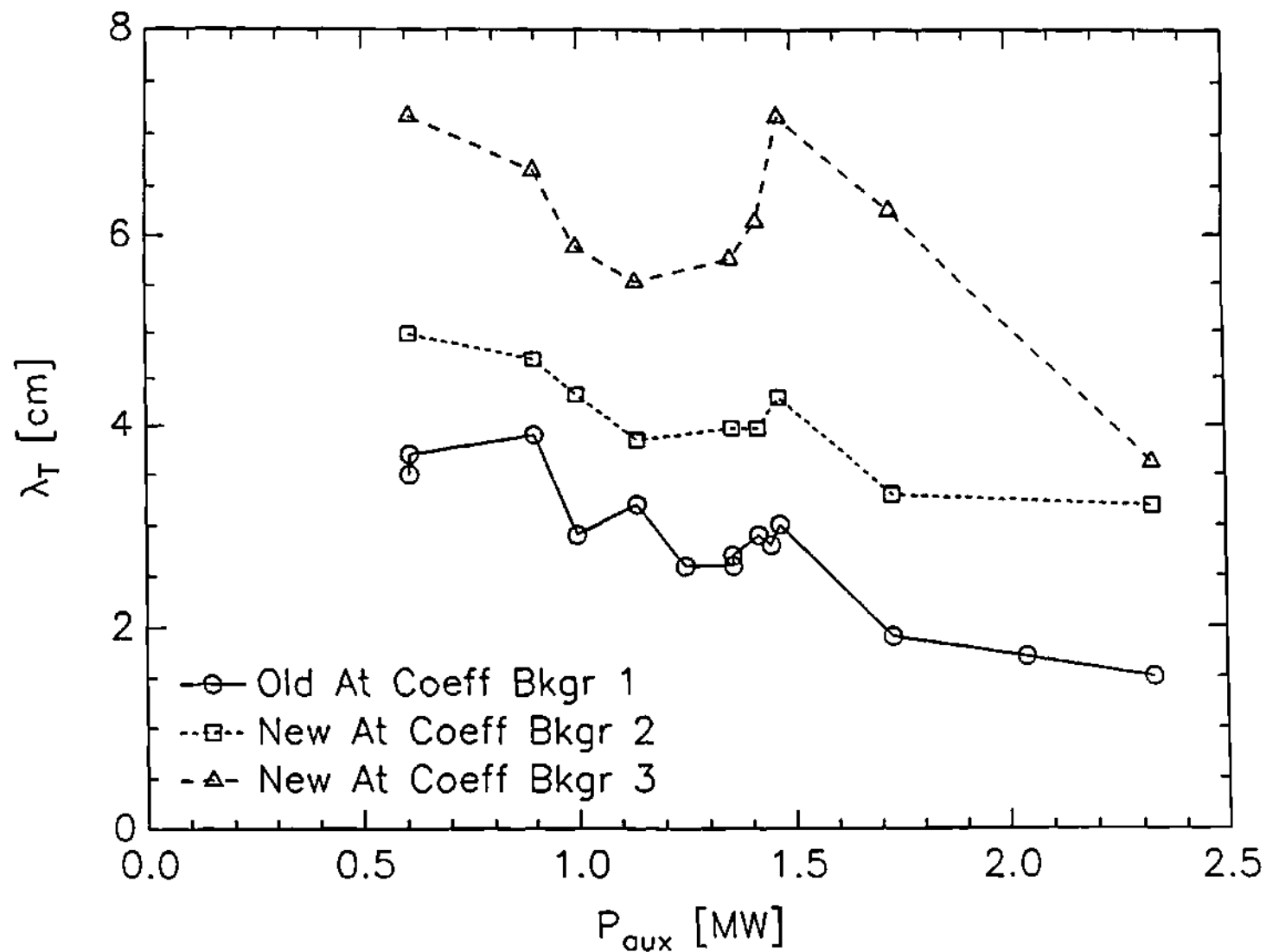


Figure 4.7 Temperature Decay Length Just Inside the Separatrix Versus Auxiliary Heating Power at MARFE Onset with Different Data Processing.

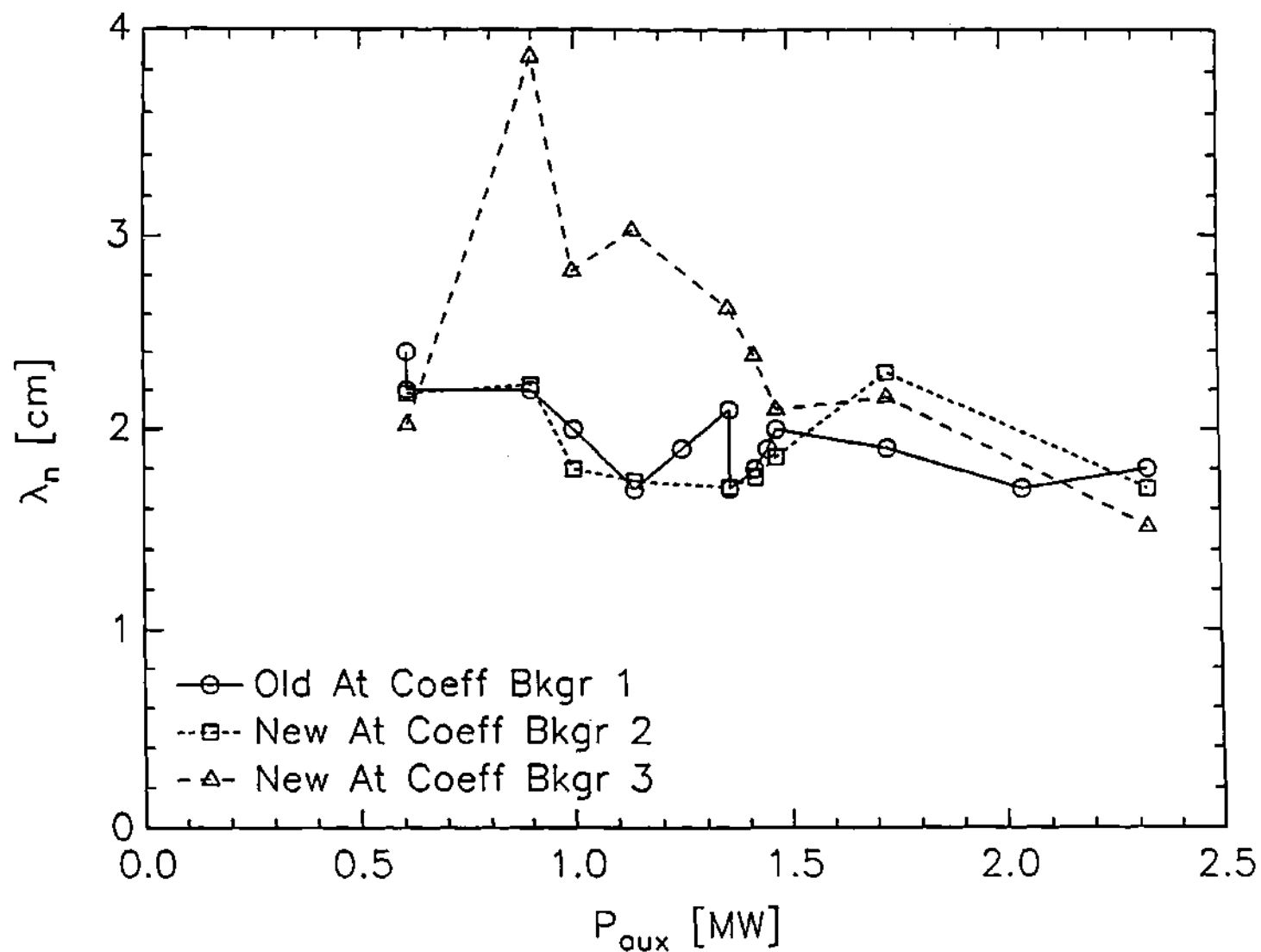


Figure 4.8 Density Decay Length Just Inside the Separatrix Versus Auxiliary Heating Power at MARFE Onset with Different Data Processing.

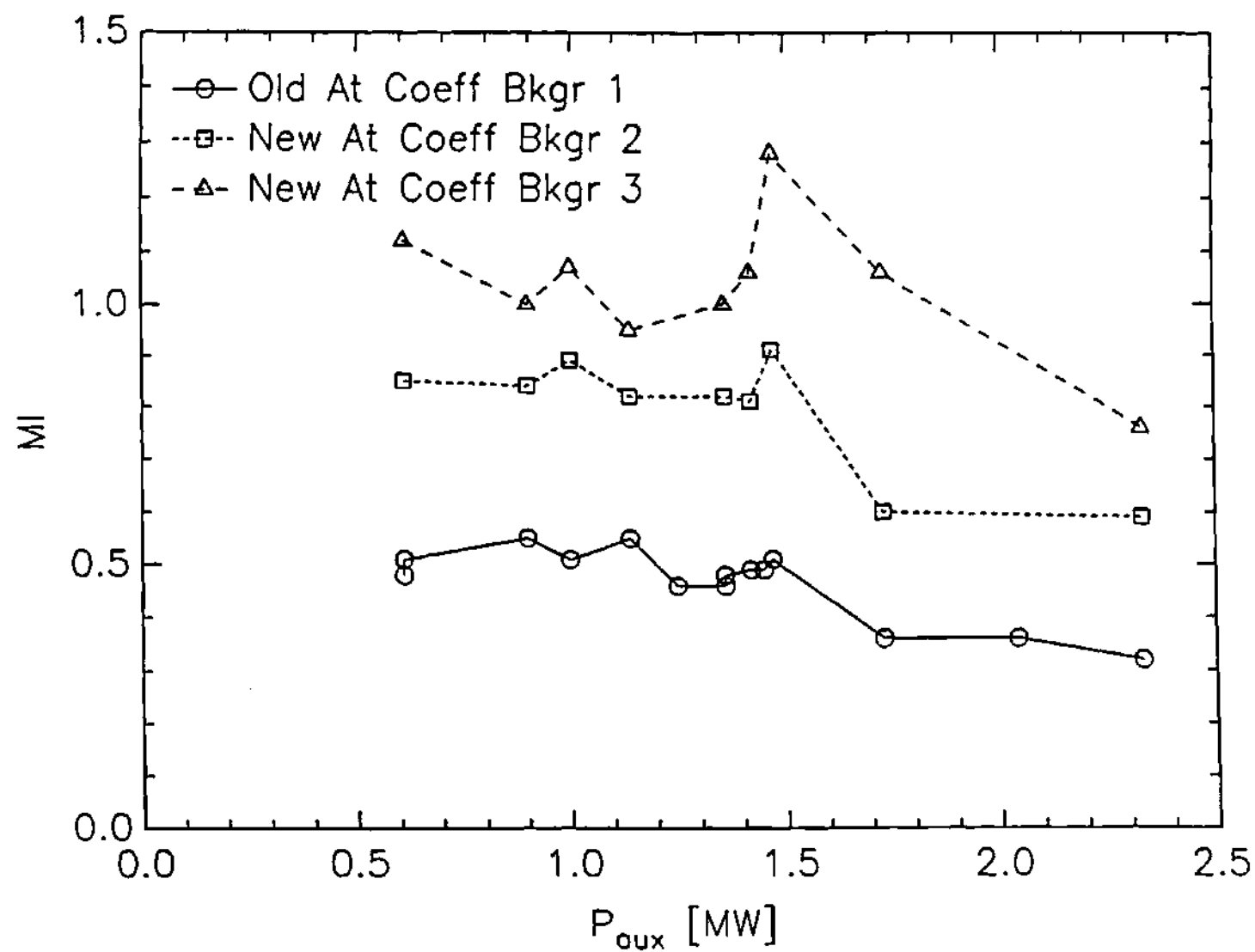


Figure 4.9 MARFE Index Versus Auxiliary Heating Power at MARFE Onset with Different Data Processing.

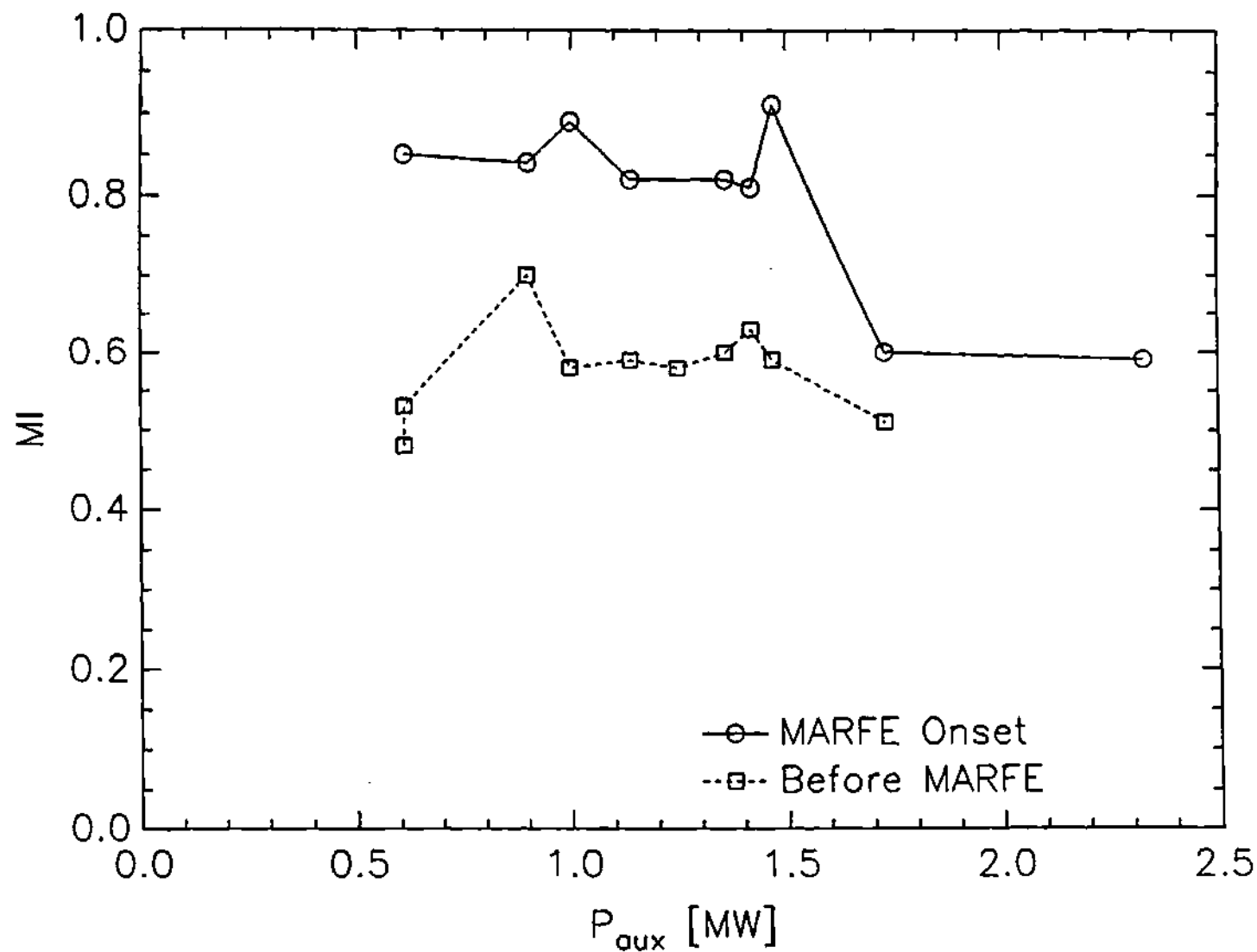


Figure 4.10 MARFE Index Versus Auxiliary Heating Power Before and at MARFE Onset Using New Atomic Coefficients and Background 2.

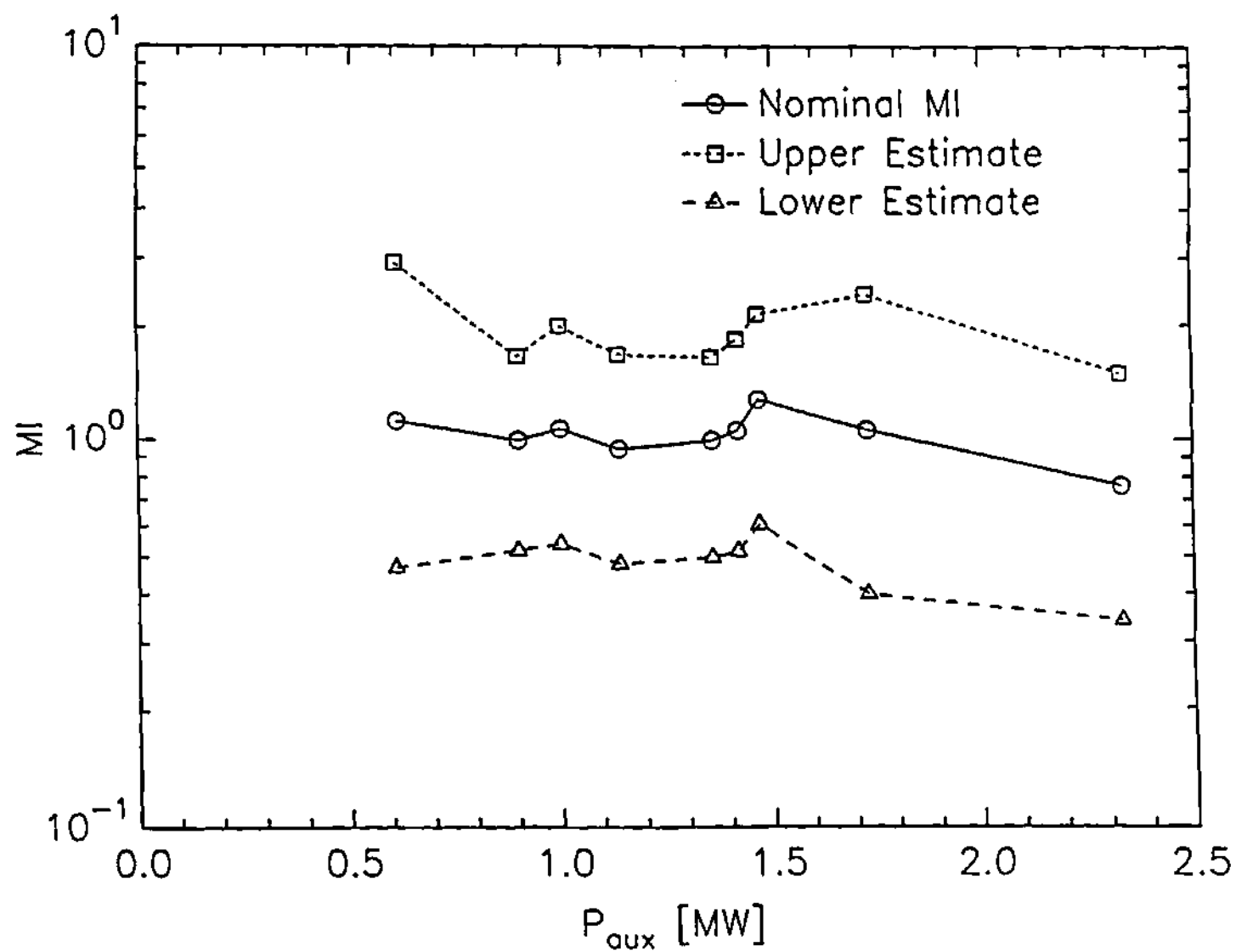


Figure 4.11 Uncertainty of MARFE Index Versus Auxiliary Heating Power.

CHAPTER V

ANALYSIS OF PARAMETRIC DEPENDENCE IN TEXTOR DENSITY LIMIT SHOTS

5.1 Introduction

Density limits have been determined in TEXTOR under many operating conditions other than those analyzed in the previous chapter. In this chapter, we examine the parametric dependencies across the broad range of density limit experiments in TEXTOR to see if they are qualitatively consistent with the predictions of the thermal instability theory. We begin by reviewing the operating history of TEXTOR with regard to the density limit.

5.2 TEXTOR Operating History

The density limit results for TEXTOR are summarized in a Hugill diagram (Figure 5.1) [5.1], where the inverse edge safety factor $1/q_e$ is plotted versus the Murakami number, the normalized line average density $\bar{n}_e R / B_T$. In cylindrical geometry, the edge safety factor is given by

$$q_e = \frac{5 a^2 B_T}{R I_p} \quad (5.1)$$

where a and R are in m, B_T is in T and I_p is in MA. Thus, the Hugill diagram is essentially a plot of the plasma current, I_p , versus the line-averaged density, \bar{n}_e .

5.2.1 Ohmic Plasmas

Since 1983 many different wall and limiter materials have been used as plasma facing materials in TEXTOR. Originally, the walls were metallic (Inconel liner) and the limiters were steel rails. The plasma was dominated by metallic impurities [5.2]. For these ohmically heated discharges, the maximum attainable line-average density increased linearly with the plasma current, up to a limiting current.

In these ohmic discharges, the density was limited by radiative collapse disruptions. A typical evolution of a discharge with a disruptive density limit for an ohmically heated plasma with continuous gas feeding is shown in Figure 5.2. The line average density increases until immediately before the disruption at $t = 1.418$ s. The central electron temperature falls as the density increases and fluctuates due to sawtooth activity. With increasing average plasma density, the radiative power loss from the impurities increases. When the power radiated by the impurities approximately equals the total input power at $t \approx 1.3$ s, a radiative collapse is initiated [5.2]. At this time the radiation power increases sharply, a luminous radiating ring forms in the plasma edge and the plasma edge detaches from the limiter. The edge temperature and density fall and the gradients of the electron temperature and density in the edge decrease (Figure 5.3). Further inside, the electron temperature and density gradients steepen. The core temperature profile remains

relatively unchanged, as only the very peak decreases. The core density profile broadens as the density increases.

Progress in increasing the density limit was made by coating the inner surface of TEXTOR with an amorphous layer of carbon (carbonization). Carbonization [5.3] led to a significant reduction of impurities in the plasma, with an increase in the density limit of ~50% over the entire current range. Later, the metal limiters were replaced by graphite limiters and the inner part of the liner was protected with graphite tiles (bumper limiter). In addition, a toroidal graphite belt limiter was installed (ALT pumped limiter). The main impurities were now carbon and oxygen. The radiation [5.3] from oxygen decreased by a factor of 5-8 and from metals by a factor of 10-20 in the plasma center compared to previous metal wall discharges that had been carefully conditioned by hydrogen glow-discharge cleaning. The metal concentration in the core was estimated to be 1×10^{-5} [5.3], while the concentration of oxygen [5.4] was approximately 0.6% ($\bar{n}_e \sim 3.5 \times 10^{19} \text{ m}^{-3}$, $I_p = 340 \text{ kA}$, $B_t = 2.0 \text{ T}$). The radial distribution of the impurities in TEXTOR was found to be peaked in the edge [5.5, 5.6]. The Z_{eff} was estimated [5.3] to be ~ 1.2 .

The density limit for both metallic and carbonized TEXTOR ohmic discharges was characterized as a hard and rapid disruption [5.7], with MHD precursors.

Still later, the plasma facing components were covered with an amorphous film of boron plus carbon (boronization). This reduced the level of oxygen in the plasma to 0.3% ($\bar{n}_e \sim 3.5 \times 10^{19} \text{ m}^{-3}$, $I_p = 340 \text{ kA}$, $B_t = 2.0 \text{ T}$) [5.4], but introduced some boron impurity.

Boronization also increased the edge densities and temperatures by 20-30% compared to carbonized conditions, which would change the hydrogen recycling as well [5.4]. A clear shift of the density limit to higher values over the entire current range was found. Further increases in the density limit were obtained by siliconization of the plasma facing components (which reduces the oxygen content of the plasma to its lowest levels [5.8]).

For pure ohmic heating (power density $\approx 10 \text{ kW/m}^3$) and boronization the density limit coincides with the global radiation limit ($\gamma \equiv P_{\text{rad}}/P_{\text{heat}} \rightarrow 100\%$). In this case, the edge density and temperature decrease such that the ionization and radiation zone shrinks to a smaller minor radius, that is, the plasma detaches from the limiter. Experiments show [5.2,5.8,5.9] both temperature and density decreasing in the outer third of TEXTOR.

Detachment does not occur with siliconization. At the highest density, the radiative fraction is about 60% for pure ohmic heating and the plasma remains well attached [5.8]. For siliconized ohmic plasmas, a poloidally asymmetric radiation concentrated on the high field side (a MARFE) occurs, followed by a disruption, similar to what is observed in auxiliary heated plasmas.

5.2.2 Auxiliary Heated Plasmas

The density limit generally increases when auxiliary heating is applied, for all wall conditions. With NBI heating, the density limit for siliconization is about 30% higher compared to boronization [5.8], as was the case with ohmic heating. An example of a neutral beam heated neon injection experiment (shot 71257) that suffered a radiative collapse is shown in Figure 5.4 [5.10]. The plasma current, toroidal magnetic field and

safety factor in this discharge were $I_p = 270$ kA, $B_T = 2$ T and $q_s = 4.4$, respectively. At $t = 1.0$ s, the neutral beam with 900 kW of heating power was turned on. Neon was injected into the plasma beginning at 1.5 s. As a result of the neon injection the electron density increased, the radiated power increased and the ohmic heating increased due to an increase in resistivity caused by the higher Z_{eff} and lower core temperature. The radiation is emitted primarily from the plasma boundary. When the radiated power equals the heating power at $t = 2.45$ s, a poloidally symmetric radiating belt appears in the edge (detachment) which is moving radially inward. This results in a disruption at $t = 2.52$ s.

Shot 71257 ($P_{heat} = 1400$ MW) and two shots ($P_{heat} = 600$ MW, 900 MW) with the same plasma current and toroidal magnetic field are shown in Figure 5.5 [5.10] as their line-average density evolves as a function of Z_{eff} . The density limit predicted by Ref. 5.11, due to radiative collapse, is shown as chain lines. Both auxiliary heated discharges ($P_{heat} = 900, 1400$ MW) disrupted near the predicted critical density [5.11] following a poloidally symmetric radiative collapse. An ohmic discharge ($P_{heat} = 600$ MW) that was nearly pure neon also disrupted at the predicted density limit. All of these shots, however, disrupted well below the Greenwald limit.

At the higher power levels obtained with neutral beam heating (power density ≥ 60 kW/m³) [5.8,5.10], the phenomenon of detachment disappears. The high heating powers lead to high- β plasmas with a pronounced Shafranov-shift. The radial heat flux (inferred from heat pulse propagation time delay studies [5.12]) then exhibits strong poloidal asymmetries which are thought to inhibit the formation of a poloidally symmetric radiating

shell [5.5,5.8]. Instead, at the highest densities a zone of high density and low temperature develops at the high field side, the MARFE. This thermal instability is driven by radiation and ionization similar to detachment and is strongly localized [5.8]. Experimentalists note that mechanisms such as poloidally asymmetric recycling [5.10,5.13,5.14,5.15,5.16], reduction of the edge parallel heat conduction to the HFS from the LFS due to increased connection length [5.10], radiation increase by impurity injection [5.14,5.15] and decrease of heating power [5.14,5.15], may contribute to MARFE development.

The formation of a MARFE often precedes a major disruption. The MARFE acts like a pump, increasing the density inside the MARFE, while the line-average density decreases by about 10-15% [5.14]. This characteristic differs from ohmic discharges, in which a poloidal plasma detachment rather than a MARFE occurred before the disruption was observed and no decrease in line-average density was apparent [5.2].

The MARFE density limit can be increased by shifting the plasma outward away from the bumper limiter [5.10,5.14,5.16], which may indicate a dependence of the MARFE onset with recycling from the bumper limiter.

5.3 MARFE Onset Parameter Dependencies In TEXTOR

Although the MARFE is an edge phenomenon, it is often [5.1,5.2,5.10, 5.17,5.18,5.19] correlated with global parameters such as plasma current, line average density, magnetic field geometry and strength, plasma geometry and heating power.

Experimentally in TEXTOR [5.1], the MARFE onset line-average density was found to scale as

$$\bar{n}_e^{cr} \propto I P_{heat}^{0.16} B^{-0.5} \quad (5.2)$$

The theoretical MARFE density limit of Eq. (2.1) depends only on edge parameters. If we assume, for the moment, that the value of χ_{\perp} in the edge is the same as the global value of χ_{\perp} , which can be related to an empirical correlation of energy confinement with global parameters [5.20]

$$\chi_{\perp} \equiv a^2 / 4\tau_E \quad (5.3)$$

then we can relate the predicted MARFE onset edge density to global parameters. A recent ITER power law regression fit [5.21] to the thermal confinement L-mode data from 14 tokamaks, including TEXTOR, found

$$\tau_{E, th}^L = 0.023 I^{0.96} B^{0.03} P^{-0.73} \bar{n}^{0.40} M^{0.20} R^{1.83} \varepsilon^{-0.06} \kappa^{0.64} \quad (5.4)$$

(s, MA, T, MW, 10^{19} m^{-3} , AMU, m). The global or 'engineering' variables are I = plasma current, R = major radius (geometric center), B = toroidal magnetic field (at major radius, R), P = loss power (corrected for charge exchange and orbit losses), \bar{n} = line average density, M = average ion mass, ε = inverse aspect ratio, and κ = elongation. Using Eqs. (5.3) and (5.4), the critical edge density predicted by Eq. (2.1) at MARFE onset scales as

$$n_{MARFE}^{edge} \propto a^2 I^{-0.96} B^{-0.03} P^{0.73} \bar{n}^{-0.40} M^{-0.20} R^{-1.83} \varepsilon^{0.06} \kappa^{-0.64} \quad (5.5)$$

Another approach is to use a theoretical transport model that accounts for fluctuations on a microscopic scale length to evaluate χ in Eq. (2.1). In TEXTOR a model [5.22] has been used that favors a gyroBohm form of the thermal diffusivity over the Bohm form. GyroBohm transport induced by ion temperature gradient (ITG) turbulence [5.23] can be written as

$$\chi = 1.02 \times 10^{-2} \frac{A_i^{1/2} F T_i^{3/2}}{L_n B^2} \text{ [m}^2\text{/s]} \quad (5.6)$$

where A_i denotes the ratio of the ion to proton mass, T_i is the ion temperature in eV, B is the magnetic field strength in tesla, the density gradient scale length is in cm, and F denotes a dimensionless parameter depending upon the safety factor q , collisionality and other factors. In TEXTOR, $F = 0.134q^2$ was used [5.22]. We use Eq. (5.6) to choose the value 3/2 for ν . We also use the definition of the energy confinement time [5.24]

$$\tau_E = \frac{3\bar{n}\bar{T}V}{P_L} = \frac{3\bar{n}\bar{T}V}{P_{\text{heat}}} \quad (5.7)$$

as the total energy in the plasma divided by the power loss, P_L , where the bar represents the average value and V is the plasma volume. We also assume that the ion and electron temperature and density are equal and that the heating power is equal to the power loss. In order to account for profile effects and to facilitate the elimination of T_i , we follow Mahdavi et al. [5.25] and define the pressure profile factor $g(\rho)$ by

$$n(\rho)T(\rho) \equiv g(\rho) \bar{n} \bar{T} \quad (5.8)$$

Using Eqs. (5.3), (5.7) and (5.8) with the gyro-Bohm form of the thermal diffusivity of Eq. (5.6), the MARFE onset edge density predicted by Eq. (2.5) scales as

$$n_{\text{MARFE}}^{\text{edge}} \propto \frac{a A_i^{1/8} [g(a) P]^3}{I^{1/2} R^{7/8} L_n^{1/4} \kappa^{3/8}} \quad (5.9)$$

A similar derivation, but using the Bohm form of the thermal diffusivity ($\chi \sim T/B$), leads to the prediction that the MARFE onset edge density scales as

$$n_{\text{MARFE}}^{\text{edge}} \propto \left(\frac{g(a) P}{R B} \right)^{1/3} \quad (5.10)$$

The separatrix density [5.26] for Ohmic and L-mode data in the ITER database has been scaled as

$$n_e(a) = 0.00236 \bar{n}_e^{1.08} \kappa^{1.11} B^{0.78} \quad (5.11)$$

Using Eq. (5.11), the critical line-average density at MARFE onset may then be scaled from Eqs. (5.5), (5.9) and (5.10), as

Global ITER Scaling of $\chi_{\perp}^{\text{edge}}$

$$\bar{n}_{\text{MARFE}} \propto a^{1.35} I^{-0.65} B^{-0.55} P^{0.49} M^{-0.14} R^{-1.24} \epsilon^{0.04} \kappa^{-1.18} \quad (5.12)$$

ITG (Gyro-Bohm) Scaling of $\chi_{\perp}^{\text{edge}}$

$$\bar{n}_{\text{MARFE}} \propto a^{0.93} I^{-0.46} B^{-0.72} [g(a) P]^{0.35} A_i^{0.12} R^{-0.81} \kappa^{-1.03} L_n^{-0.23} \quad (5.13)$$

Bohm Scaling of $\chi_{\perp}^{\text{edge}}$

$$\bar{n}_{\text{MARFE}} \propto B^{-1.03} \left[g(a) P \right]^{0.31} R^{-0.31} \kappa^{-1.03} \quad (5.14)$$

The ITG scaling of line-average density at MARFE onset, Eq. (5.13), is likely to have other indirect dependencies, since L_n depends on I and B .

5.3.1 Current Scaling

The maximum line-average density scales linearly with the plasma current in most tokamaks [5.17] and agrees well with the predicted Greenwald limit [5.18]

$$\bar{n}_{\text{GW}} \left(10^{20} \text{ m}^{-3} \right) = \frac{I \left(\text{MA} \right)}{\pi a^2 \left(\text{m} \right)} \equiv j \left(\text{MA} / \text{m}^{-2} \right) \quad (5.15)$$

where j is the average plasma current density. This was confirmed in a set of standard auxiliary heated TEXTOR discharges [5.10] in which the current was varied by a factor of three and the densities recorded just prior to the development of a MARFE as shown in Figure 5.6. The Greenwald limit, however, can be exceeded by a factor of ~ 1.7 in TEXTOR if the plasma facing components have received a fresh siliconization, due to silicon's lower impurity release at high density compared to carbon [5.1].

The theoretical MARFE density limit of Eq. (2.5) may be written in the form

$$n_{\text{MARFE}}^{\text{edge}} \propto \frac{\frac{f_{\text{cond}}}{T A_{\text{LCFS}}} \left(\eta j^2 + P_{\text{aux}} / V \right) \left(\nu L_T^{-1} - \left(1 - C^{(2)} \right) L_n^{-1} \right)}{f_0 \frac{E_{\text{ion}}}{T} \left(\frac{\nu L_0}{T} - \frac{\partial L_0}{\partial T} \right) + f_z \left(\frac{C L_z}{T} - \frac{\partial L_z}{\partial T} \right)} \quad (5.16)$$

in terms of auxilliary heating power, current density, neutral fraction and impurity fraction. L_0 and L_z are the neutral and impurity emissivities. If P_{aux} is small compared to ηj^2 (ohmic heating), then n_{MARFE} scales linearly with current density. When P_{aux} is larger than ηj^2 (auxiliary heating), there is no obvious current scaling. However, there may be indirect dependence on current which is not included in Eq. (5.16). If increasing the current raises the edge temperature, then Eq. (5.16) would predict an increase of the MARFE edge density limit.

The predicted MARFE onset edge density scalings of Eqs. (5.5) and (5.9), derived for the global ITER and ITG χ -scalings, are inversely dependent on current rather than proportional to current and the Bohm scaling does not involve current, which at first consideration seems inconsistent. However, the edge density does not scale with current in the same manner as does the line-average density, because the density profiles are current dependent. If we compare the conditions at MARFE onset in shots 80252 ($I_p = 290$ kA, $\bar{n}_e = 5.1 \times 10^{19} \text{ m}^{-3}$, $n_e(a) = 9.5 \times 10^{18} \text{ m}^{-3}$, $T_e(a) = 40$ eV, $\lambda_T = 3.9$ cm, $\lambda_n = 5.8$ cm) and 81575 ($I_p = 350$ kA, $\bar{n}_e = 6.0 \times 10^{19} \text{ m}^{-3}$, $n_e(a) = 7.4 \times 10^{18} \text{ m}^{-3}$, $T_e(a) = 32$ eV,

$\lambda_T = 5.5$ cm, $\lambda_a = 3.0$ cm), which have the same heating power and magnetic field but different currents, we observe that the line average density does indeed increase linearly with current, but the edge density decreases with current as predicted by the global ITER and ITG scalings, Eqs (5.5) and (5.9).

From this we conclude that $\bar{n} / n_{\text{edge}} = f(I)$ in TEXTOR and that this (unknown) dependence of the density profile on the current must be taken into account in attempting to reconcile a theory for the limiting edge density with measurements of the limiting line-average density. Experimental data is needed to determine the effect current has on the density profiles. Furthermore, if the auxiliary heating is balanced by increased radiative and atomic physics cooling, the current scaling of $n_{\text{MARFE}}^{\text{edge}}$ may extend into the auxiliary heating regime.

5.3.2 Magnetic Field Scaling

The dependence of the MARFE density limit on the toroidal magnetic field is less certain [5.1], since B_T could only be varied by a factor of 1.5. In Figure 5.7a, the scaling $n_e \sim B_T^{-0.5}$ yields a reasonable fit to the data, but so does a fit of the form $a+b/B_T$.

The predicted MARFE onset edge density has a weak dependence on B for the global ITER χ -scaling, has no B dependence for χ -scaling derived from ITG (gyro-Bohm) theory and varies as $B^{-1/3}$ for Bohm scaling. There may be, however, a strong dependence

of the density profile on B, which would introduce an indirect B-dependence into the theoretical prediction.

The predicted MARFE onset line-average density dependence using the global ITER (Eq. 5.12), ITG (Eq. 5.13) and Bohm (Eq. 5.14) scalings for χ are $\bar{n}_{\text{MARFE}} \sim B^{-0.55}$, $B^{-0.72}$ and $B^{-1.03}$, respectively. The predicted magnetic field dependence of the MARFE onset density is generally consistent with the experimental observations [5.1], when the measured effect of magnetic field on profiles is taken into account.

5.3.3 Power Scaling

There is some uncertainty with regard to how the MARFE density limit scales with power. Waidmann and Kuang [5.2] found the measured line-average density limit increased with the square root of the additional heating power delivered by the neutral beams, but not the total heating power. Rapp et al. [5.1] found the line-averaged density to scale as $P_{\text{heat}}^{0.16}$ (Figure 5.7b) and the critical edge density to scale with the separatrix power flux as $Q_r^{0.22}$.

The predicted MARFE onset edge density using the global ITER (Eq. 5.5), ITG (Eq. 5.9) and Bohm (Eq. 5.10) scalings for χ are $n_{\text{MARFE}}^{\text{edge}} \sim P^{0.73}$, $P^{0.38}$ and $P^{0.33}$, respectively. The predicted MARFE onset line-average density using the global ITER (Eq. 5.12), ITG (Eq. 5.13) and Bohm (Eq. 5.14) scalings for χ are $\bar{n}_{\text{MARFE}} \sim P^{0.49}$, $P^{0.35}$

and $P^{0.31}$, respectively. These predicted scalings are generally consistent with the experimental observations.

The MARFE density limit theory, as expressed by Eq. (2.5), predicts that the edge density should scale as the square root of the separatrix power flux. As discussed in Chapter 4, there are discontinuities in the power scan sequence examined in that chapter, effectively dividing it into several separate power scans. In Figure 5.8, the measured line-average MARFE onset density is plotted against P_{sep} . Also shown (dashed) are plots of $P_{sep}^{0.5}$ over the co-injected series of shots ($P_{sep} = 0.68$ -1.12 MW) and over the co- plus counter-injection series of shots ($P_{sep} = 1.20$ -1.63 MW), both normalized to the lowest power shot in the series. In Figure 5.9, the measured edge density just prior to MARFE onset is plotted against the power crossing the separatrix. Also shown (dashed) is

$$n_{MARFE}^{edge} \sim P_{sep}^{0.5}, \text{ normalized to } n_{MARFE}^{edge} \text{ at } P_{aux} = 0.90 \text{ MW. The theoretical } n_{MARFE}^{edge} \sim$$

$P_{sep}^{0.5}$ obviously provides a good fit to the data.

In Eq. (5.16), when P_{aux} is larger than ηj^2 , the edge temperature increases with auxiliary heating (Table 4.1) in the range of 30-50 eV resulting in a decrease of $f_z L_z$ when carbon and oxygen (Figure 5.10) are the dominant radiators in the edge. This change increases the MARFE density limit predicted by Eq. (5.16). The Hugill diagram (Figure 5.1) illustrates this increase of the density limit for boronized walls with ohmic and auxiliary heating ($P_{aux} = 1.7$ MW).

The predicted power scaling with heating power of both line-average and edge densities at MARFE onset is in good agreement with experimental observation.

5.3.4 Plasma Position Dependence

In order to investigate the influence of plasma position on MARFE development and hence on the density limit, TEXTOR's minor radius was reduced to $a = 42$ cm by inserting poloidal main limiters from the top and the bottom (Figure 3.1). The horizontal position of the plasma was shifted by manipulating the magnetic control signal. Shifting the plasma horizontal position outward increased the MARFE onset density limit in TEXTOR [5.10, 5.16], as shown in Figure 5.11. The plasma was heated by NBI ($H \rightarrow D$, co-direction) with a heating power of $P_{aux} \sim 1.0$ MW [5.10].

A threshold in the neutral hydrogen flux from the bumper limiter for MARFE onset was observed. Since the line-averaged density for outward shifted plasmas was higher than that of inward shifted plasmas, it was concluded [5.10, 5.16] that MARFE onset was triggered by the bumper flux and not the density. However, the variations of the edge temperature and density with plasma position were not reported.

The dependence of plasma edge properties and hence MARFE onset was studied in discharges limited by the ALT-II limiter and/or the bumper limiter, with the poloidal main limiters withdrawn. The plasma minor radius changes as a function of the plasma position, as shown in Eqs. (3.1)-(3.3). Using the displacement of shot 80252 ($P_{aux} = 1.33$ MW, $H \rightarrow D$, co-direction) as the reference ($\Delta R = 0$), the plasma was shifted inward (ΔR

= -1 cm) and shifted outward ($\Delta R = 3$ cm). The edge temperature did not change relative to shot 80252 for the inward shifted position and increased for the outward shifted position. The edge density at MARFE onset was the same ($\sim 6.5 \times 10^{18} \text{ m}^{-3}$) for the reference and the inward shifted plasmas. The edge density of the outward shifted plasma was higher without a MARFE forming [5.10].

Shifting the plasma column outward will reduce the generation of neutrals and impurities at the bumper limiter, reducing f_0 and f_z in Eqs. (2.1), (2.5) and (5.16), which would increase the predicted MARFE onset density limit. Numerically it was found that above an edge temperature of about 26 eV, a further increase in edge temperature would increase the predicted MARFE onset density limit. Thus, the theoretical prediction is qualitatively consistent with the observed increase in the MARFE onset density limit shown on the Hugill diagram in Fig. 5.1 and in Fig. 5.11, as the plasma is shifted outward away from the bumper limiter.

5.3.5 Wall Material

The transition from metallic walls to carbonized walls will reduce the term $f_z L_z$ in Eqs.(2.1), (2.5) and (5.16) and increase the predicted MARFE edge density limit for all currents. Moving from carbonized walls to boronized walls further reduces $f_z L_z$ (particularly the contribution of oxygen) and further increases the predicted density limit. Moving from boronized to siliconized walls further reduces the oxygen content, reducing $f_z L_z$ and increasing the density limit further. These predictions match qualitatively the

observed increases in the density limit with the change in wall material illustrated by the Hugill diagram in Figure 5.1.

5.4 Radiative Collapse Density Limit Parameter Dependence in TEXTOR

If we assume that the temperature dependence of the heating term can be neglected, then the radiative collapse volume-average density limit of Eq. (2.7) may be written in the form [5.27]

$$n_{RC} \approx \frac{\chi_{\perp} \left(5.5/a^2 \right)}{f_z \left(-\frac{z}{\partial T} \right)} \quad (5.17)$$

We can use Eq. (5.3) and the power balance

$$\frac{3 n T}{\tau_E} + n^2 f_z \frac{L_z}{z} = \eta j^2 + \frac{P_{aux}}{V} \quad (5.18)$$

to obtain the global parameter dependence of the radiative collapse density limit as

$$n_{RC} \approx \left\{ \frac{\frac{5.5^2}{12 T} \left[\eta j^2 + P_{aux} / V \right]}{\frac{5.5^2}{12 T} f_z \frac{L_z}{z} - f_z \frac{z}{\partial T}} \right\}^{1/2} \quad (5.19)$$

which possesses a form very similar to the MARFE density limit, Eq. (2.5). The only terms missing are the atomic physics terms, which have been neglected since neutrals are confined to the plasma edge, and the dependence on the edge gradient scale lengths. Thus, the parameter dependence of the radiative collapse will be very similar to the parameter dependence of the MARFE. For ohmic discharges, the radiative collapse density limit of Eq. (5.19) scales linearly with current, in general agreement with the ohmic discharges in the Hugill diagram (Fig. 5.1). The radiative collapse density limit of Eq. (5.19) will decrease with increasing L_z and more negative $\partial L_z / \partial T$. The radiative collapse density limit of Eq. (5.19) scales with the square root of the auxiliary heating power, which is consistent with experimental observation. There is general consistency of all these dependencies with the Hugill diagram (Fig. 5.1).

We note that all the radiative collapse phenomena in TEXTOR may be adequately described as a loss of power balance [5.10,5.11] with the density limit scaling as

$$\bar{n}_e^{DL} \propto \sqrt{\frac{P_{\text{heat}}}{Z_{\text{eff}} - 1}} \quad (5.20)$$

The general form of Eq. (5.20) is consistent with Eq. (5.19).

5.5 Symmetric Detachment or MARFE as the Density Limiting Phenomena?

As the density is increased in a typical TEXTOR discharge, the edge radiation and atomic physics cooling lowers the edge temperature until the plasma detaches from the

limiter, or the edge temperature remains sufficiently high that a MARFE forms. In Figure 5.5, six discharges are shown (solid circles) with a high heating power ($P_{\text{heat}} = 1400$ MW) and low Z_{eff} ($Z_{\text{eff}} < 2.5$) that MARFE prior to disrupting near the Greenwald density limit and not at the density limit implied by a loss of power balance given by Eq. (5.20) and shown as chained lines. The solid lines in Fig. 5.5 indicate the evolution of three higher Z_{eff} ($Z_{\text{eff}} > 2.5$) discharges that end with a symmetric radiative collapse and a detached plasma just before disruption.

The detachment of the plasma from the limiter implies that the process of recombination dominates ionization in the region just in front of the limiter. By examination of the recombination and ionization rates for hydrogen shown in Figure 5.12 [5.29], it is clear that the electron temperature in front of the limiter must be ~ 1 eV for detachment to occur. The reason that some shots end in a disruption following a symmetric detachment and radiative collapse while other shots end in a disruption following a MARFE can be understood in terms of the effect of the different edge conditions on the MARFE instability.

Figure 5.13 [5.9] shows the variation of edge parameters at the separatrix in carbonized TEXTOR discharges with respect to changes in discharge conditions like plasma current, average density, heating method, filling gas and radiative fraction. The edge temperature is seen to increase for increasing plasma current in ohmic discharges and to increase further for NBI heated discharges, while decreasing monotonically with increasing line-average density in all cases. The edge density n_e , the flux Γ_{HD} of recycling

neutrals at the limiter and the global radiative fraction γ increase initially with line-average density but begin to drop above a critical line-average density. The critical line-average density for detachment to begin occurs when the measured edge temperature (at a position poloidally removed from the limiter) drops to ~ 20 eV. In the detached plasma state, the measured edge temperature is about 10 eV; however, the temperature at the point of detachment must be about 1 eV.

The separatrix temperature and density in TEXTOR is typically measured at the midplane of the LFS. The pressure, to first approximation, may be assumed constant on a given flux surface. Therefore, a MARFE-like structure with high density and low temperature would be expected to be found near the limiters. Regions of enhanced radiation were observed near the limiters in TEXTOR [5.15].

Figure 5.14 [5.8] shows the variation of boronized and siliconized TEXTOR edge parameters and radiative fraction with respect to changes in line-average density for Ohmic and NBI heating. The toroidal magnetic field and plasma current are fixed at 2.25 T and 350 kA, respectively. The edge temperature decreases monotonically with increasing line-average density in all cases. The edge temperatures in auxiliary heated siliconized shots are lower because Si is a much stronger radiator above 40 eV than O, which dominates the radiation with boronization. For the case of ohmic heating, however, the edge temperature of the siliconized shots initially is lower but decreases slower with line-average density than in the boronized shots, due to the lower L_z of Si between 15 and 40 eV. The edge density increases monotonically with increasing line-

average density, with no sign of detachment. The radiative fraction of the boronized shots increases with increasing line-average density, while it decreases for siliconized shots. Also shown (dashed) for the NBI heated case is a model calculation in which O is eliminated.

At higher line-averaged density in the ohmic case, the edge temperature of the boronized plasma is lower than that of the siliconized plasma, while the edge density of the boronized plasma is higher than that of the siliconized plasma. The MARFE and radiative collapse density limits would both tend to be higher in the siliconized plasma due to the higher edge heat flux and edge temperature. The lower impurity levels and hence radiation levels must prevent the region in front of the limiter from becoming cool enough to detach before a MARFE can occur in the siliconized plasma. The same reasoning appears to apply to the auxiliary heated case. The edge heat flux and edge temperature are high enough to prevent the limiter from detaching, so the density limit is determined by the MARFE density limit. An explicit formula for the detachment of the limiter has not been derived, but it generally occurs when $P_{\text{rad}} \approx P_{\text{heat}}$ and the edge heat flux becomes small.

Previous work based on the MARFE theory used in this thesis included an explanation for MARFE formation and subsequent evolution into a detached symmetric plasma edge [5.30]. In this theory, cooling by impurity radiation and ionization causes a radiative band to be formed at the radial location at which the plasma temperature maximizes the cooling, usually near the edge. The edge impurity density initially is below

the MARFE density limit for all the modes, in which case the plasma is in the $k_{\parallel} = 0$ mode and a poloidally symmetric band of radiating impurities is formed near the plasma edge. As the impurity density increases, the density limit for the $k_{\parallel} = 0$ mode is eventually exceeded, and the edge plasma evolves into some combination of the still stable $k_{\parallel} > 0$ modes. As the edge impurity density continues to increase, the density limits of modes with successively higher mode numbers are exceeded, forcing the edge plasma into more highly asymmetric stable modes (the MARFE).

As the edge plasma becomes more asymmetric, it would normally reach a point at which nonlinear effects would cause a collapse of the temperature distribution, leading to a disruption, hence the disruption density limit. Thus, the MARFE ($k_{\parallel} = 0$) density limit (Eq. 2.1) would be somewhat less than the disruption ($k_{\parallel} > 0$) density limit, as observed.

Under certain conditions, the radiating edge plasma will cool sufficiently that the atomic physics effects will increase the density limit for successively lower modes down to the $k_{\parallel} = 0$ mode, and the plasma will evolve from a MARFE back to a symmetric edge distribution. At such low edge temperatures, the plasma is detached or near-detached.

This sequence of events which was observed in TFTR discharges [5.31], may provide some insights as to why the density limit in ohmic TEXTOR plasmas is generally a disruption following detachment, but in auxiliary heated plasmas is generally a disruption following a MARFE.

In an ohmic plasma, the density limit generally occurs when most of the heating power is radiated and the edge temperature is thus very low. To get to this state, however, the edge cools as the density is increased, as shown in Figures 5.13 and 5.14. For a discharge in a carbonized or boronized tokamak, oxygen will be the dominant impurity. The neutral emissivity term tends to be smaller than the radiation emissivity

term in the denominator of Eq. (5.16) at MARFE onset. The $-\frac{\partial L_0}{\partial T}$ component of the neutral emissivity will become the dominant term at temperatures below 10 eV (Fig. 5.12) and drive the MARFE density limit to large values. The impurity emissivity, however, varies over several orders of magnitude in the temperature range 10-100 eV. The peak of L_z will determine the minimum MARFE density limit. For example, a minimum in the MARFE onset edge density will occur somewhat above the local maximum of the oxygen L_z near 25 eV (Fig. 5.10). If the edge density is less than the MARFE onset edge density, then the edge continues to cool without a MARFE until the plasma detaches, as observed in TEXTOR. Apparently in TFTR it was possible to create an edge density greater than the minimum MARFE onset density “by ramping the plasma current down while maintaining a high influx of neutral gas.” A MARFE was triggered at an edge temperature somewhat above 25 eV, where L_z is large and $\partial L_z / \partial T$ is negative and stabilizing (Eq. 5.16). The conditions in TFTR were different from TEXTOR in that the MARFE didn’t cause a disruption, but allowed the edge to cool below 25 eV. Here, L_z decreases with temperature ($\partial L_z / \partial T$ is positive) and the MARFE onset density rises toward the edge

density. If the MARFE onset density limit becomes larger than the edge density before the plasma detaches, the plasma evolves back to a poloidally symmetric edge that cools further until it detaches. Otherwise, the edge with the MARFE may cool until the plasma detaches and the radiation in the edge is symmetric poloidally.

In auxiliary heated TEXTOR discharges, the edge density and temperatures at a given line-average density are significantly higher than in ohmic heated plasmas (Figures 5.13 and 5.14). The higher edge temperature makes it possible to achieve much higher line-average densities before a MARFE occurs. This is qualitatively consistent with the Hugill diagram (Fig. 5.1).

In siliconized TEXTOR discharges, silicon is the dominant impurity and has a local maximum in its L_z at ~ 5 eV (Fig. 5.10), much lower than oxygen. From about 100 eV down to about 15 eV, silicon's L_z is decreasing with temperature and $\partial L_z / \partial T$ is positive (stabilizing in Eq. 5.16). In Fig. 5.14, the radiative fraction is seen to actually decrease with increasing line-average density in this edge temperature interval, which is consistent with Fig. 5.10. The edge temperature and density are lower for the auxiliary heated siliconized case than for the boronized case in Fig. 5.14. However, the minimum in the MARFE onset density will occur at a much lower temperature for the siliconized case than for the boronized case. This should permit a much higher density to be achieved before MARFE onset. This is consistent with the neutral beam heated boronized and siliconized cases shown in the Hugill diagram (Fig. 5.1).

Thus, the reason that the ohmic discharges in TEXTOR generally disrupt following symmetric detachment and radiative collapse, while the auxiliary heated discharges generally disrupt following a MARFE and radiative collapse seems to be as follows. As the density increases in ohmic discharges the edge cools sufficiently that the edge density limits for MARFE onset (which approach a minimum as a peak in the L_z nears) remains larger than the actual edge density, allowing the edge to cool symmetrically until detachment takes place. In auxiliary heated discharges, the actual edge densities are higher and become larger than the MARFE edge density limit before the edge can cool to the point of detachment.

The exceptions to the general rule of detachment in ohmic discharges and MARFEs in auxiliary heated discharges can be explained in the same way. MARFEs are observed prior to disruption in ohmic discharges with siliconized walls but not with boronized walls. As shown in Fig. 5.14, the edge density of the boronized shot is much lower on the high temperature side of oxygen L_z peak, than the edge density of the siliconized shot on the high temperature side of the silicon L_z peak. The edge density of the siliconized shot is more likely to be greater than the MARFE onset density.

The three auxiliary heated discharges which end in detachment followed by disruption, shown by the solid lines in Fig. 5.5, achieve quite high Z_{eff} . Since the L_z peak for Ne occurs at about 40 eV and somewhat smaller than the peak of O and Si, the actual edge density apparently remains smaller than the MARFE onset density. This allows the edge to cool symmetrically to the point of detachment.

5.6 Conclusions

The purpose of this chapter is to discuss a qualitative comparison of the parameter dependence of the measured density limit in TEXTOR with the predictions of the MARFE and radiative collapse thermal instability density limit theories.

The measured MARFE line-averaged density limits scaled linearly with current ($n \sim I$), as the inverse square root of the magnetic field ($n \sim B^{-0.5}$) and as the square root of the auxiliary heating power ($n \sim P_{\text{aux}}^{0.5}$). When the power balance and some empirical scalings are used to convert the theoretical prediction of the edge density limit in terms of edge parameters into a prediction of the line-average density limit in terms of I , B and P , we find good agreement with the B - and P -scalings, but not with the I -scaling. When we examine this more closely, we find that the predicted I -scaling of the edge density limit agrees with experiment for two shots differing only in the value of I and that this edge density limit is inverse to the line-average density limit I -scaling which was reported, indicating that there is a strong dependence of the density profile on I which is not being taken into account.

The measured MARFE line-average density dependence on wall material and on plasma position within the chamber can be qualitatively explained by the effect on the impurity and neutral concentrations in the plasma edge. The increase in MARFE density limit when a metal wall is replaced with a carbon wall, when a carbon wall is replaced with a boronized wall, and when a boronized wall is replaced with a siliconized wall can all be understood in terms of reduction of radiation intensity in the plasma edge, since a

reduction in radiation intensity leads to a larger predicted MARFE density limit. The measured MARFE line-average density dependence on position can be reconciled qualitatively with the MARFE density limit theory by taking into account the reduction in recycling hydrogen and impurity fluxes as the plasma moves away from the inner bumper limiter, which increases the predicted MARFE density limit.

The measured density limit in shots which symmetrically detach, rather than MARFE, prior to disruption can be described by an expression which scales as the square root of the ratio of the heating power to the impurity content. The theoretical thermal instability density limit formula has the same form. In particular, both formulas predict the Greenwald $n \sim I$ scaling for ohmic heated plasmas. The same dependence of the density limit on wall conditioning as discussed above for the MARFE is observed experimentally and predicted theoretically for the 'radiative collapse induced detachment followed by disruption' density limit.

Most ohmic shots and some high Z_{eff} auxiliary heated shots are observed to detach symmetrically and disrupt at the density limit, while most auxiliary heated shots and some low Z_{eff} ohmic shots are observed to MARFE and disrupt at the density limit. This difference can be explained by the fact that the MARFE edge density limit decreases with decreasing edge temperature (in the temperature range where dL_{e}/dT is negative). For the shots with a relatively low edge temperature throughout (ohmic and high Z_{eff} auxiliary heated shots), the MARFE edge density limit remains above the actual edge density throughout and the edge cools symmetrically and detaches. At some point during shots

with higher edge temperature (auxiliary heated and low- Z_{eff} ohmic shots), the MARFE density limit becomes smaller than the actual edge density , resulting in a MARFE before the edge can cool to the point of detachment.

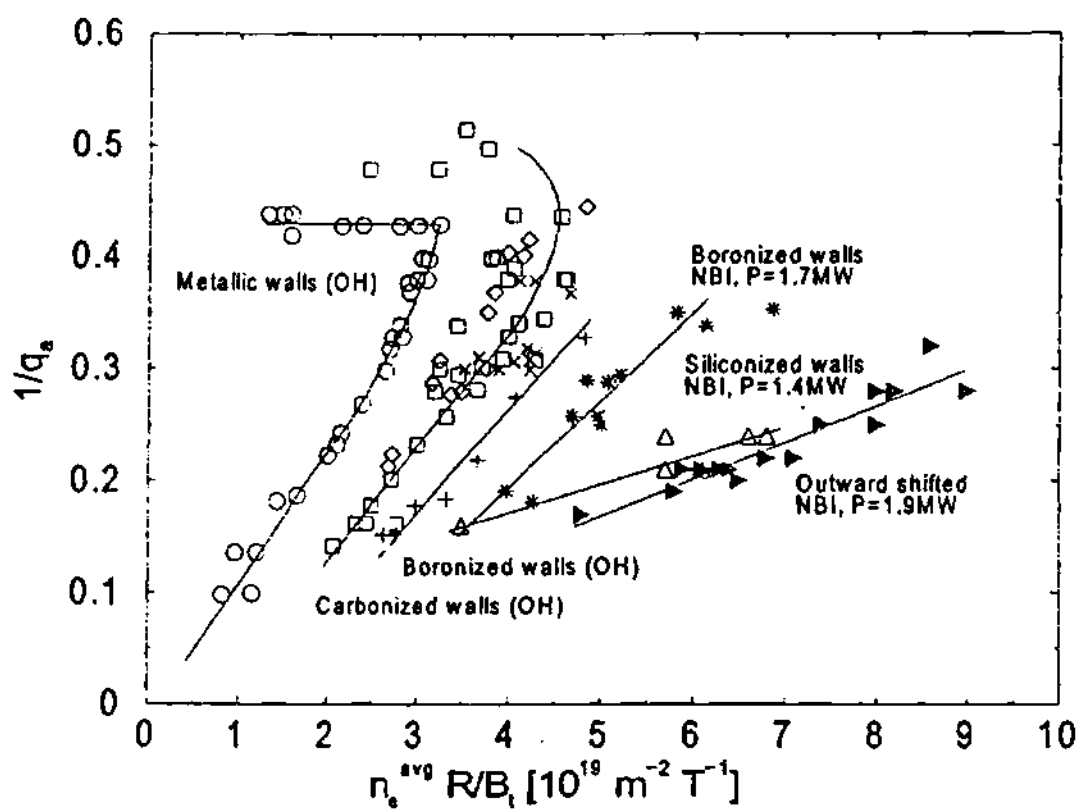


Figure 5.1 Hugill-diagram of TEXTOR.

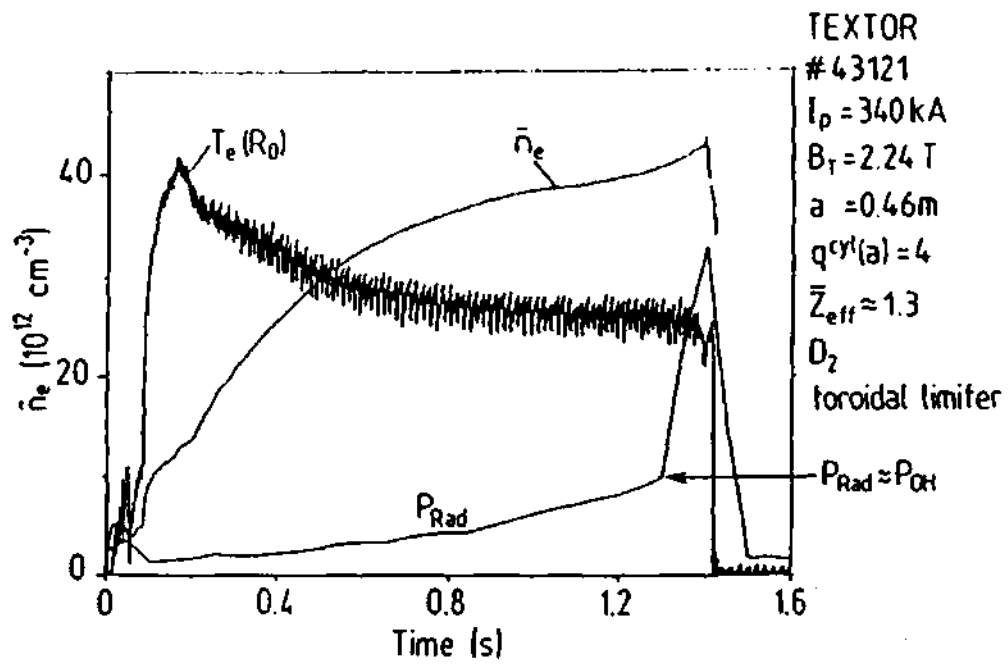


Figure 5.2 The line averaged density \bar{n}_e , the electron temperature on axis $T_e(R_0)$ and the total radiated power P_{rad} from an Ohmic discharge which disrupted at the density limit.

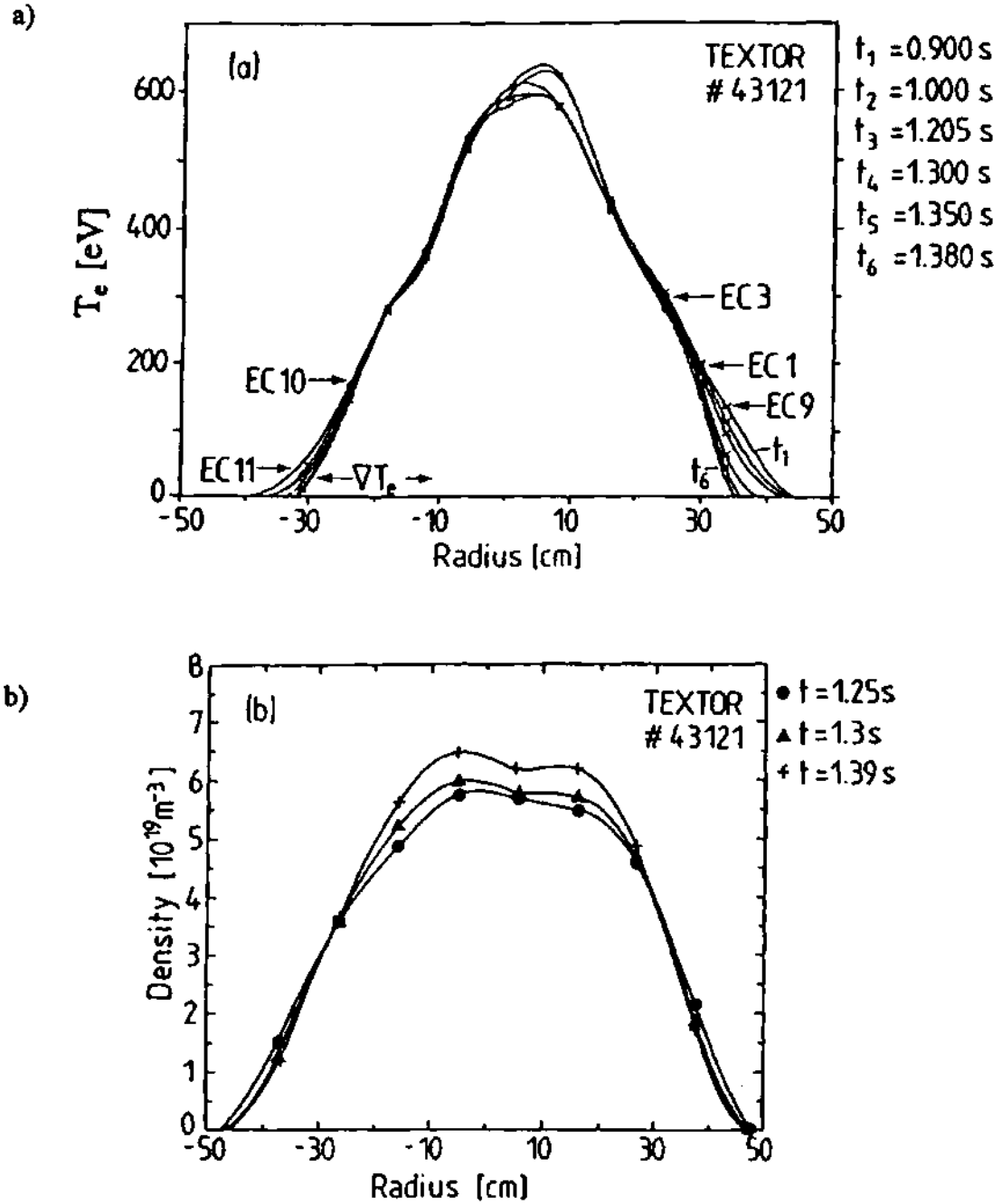


Figure 5.3 a) Electron temperature profile and b) radial density profile at the beginning of contraction. CCD camera recording showed plasma detachment from the limiters. The temperature gradient region is indicated by the ∇T_e on the high field side of the profile. The labels EC1, etc., denote ECE channels.

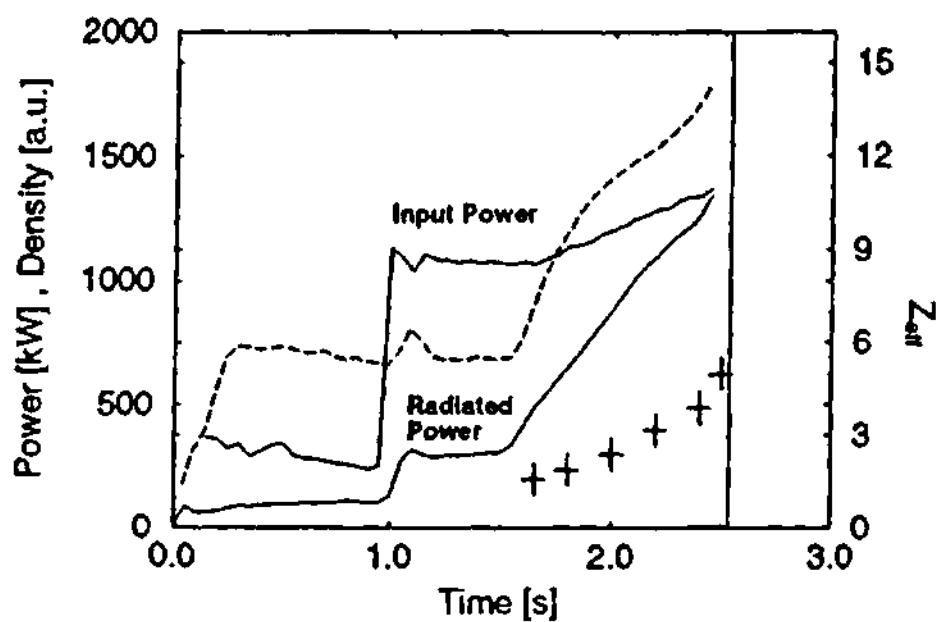


Figure 5.4 Temporal evolution of the radiative collapse of TEXTOR shot 71257: heated and radiated powers, solid curves; line-averaged density, dashed curve; Z_{eff} , plus symbols. Neon injection begins at 1.5 s and the time of disruption is indicated by the vertical line.

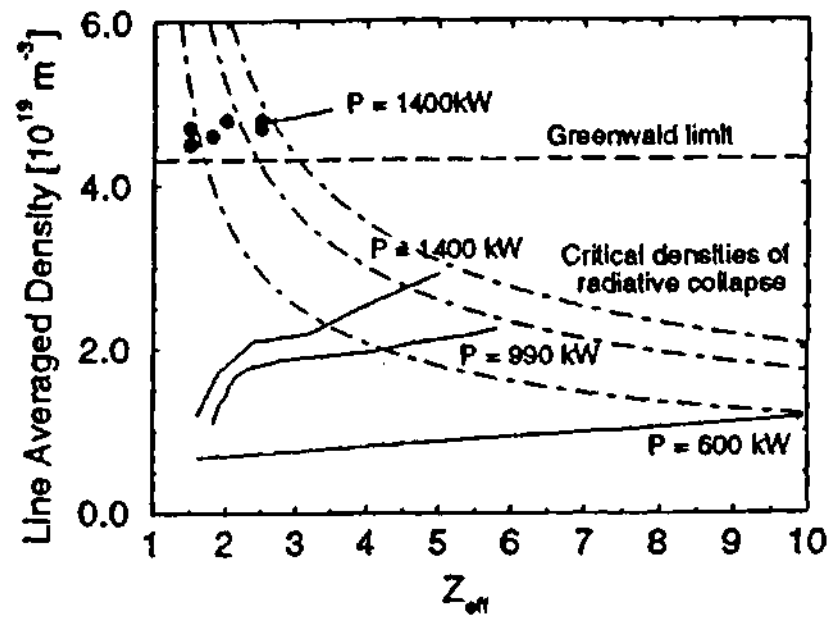


Figure 5.5 Line-averaged density versus Z_{eff} comparison of TEXTOR shots that disrupted after detachment or MARFES. Evolution of three radiative collapse discharges that detached (solid curves) and the predicted density limit (chain curves). The circles indicate discharges that MARFEd before disrupting near the Greenwald limit (horizontal dashed line).

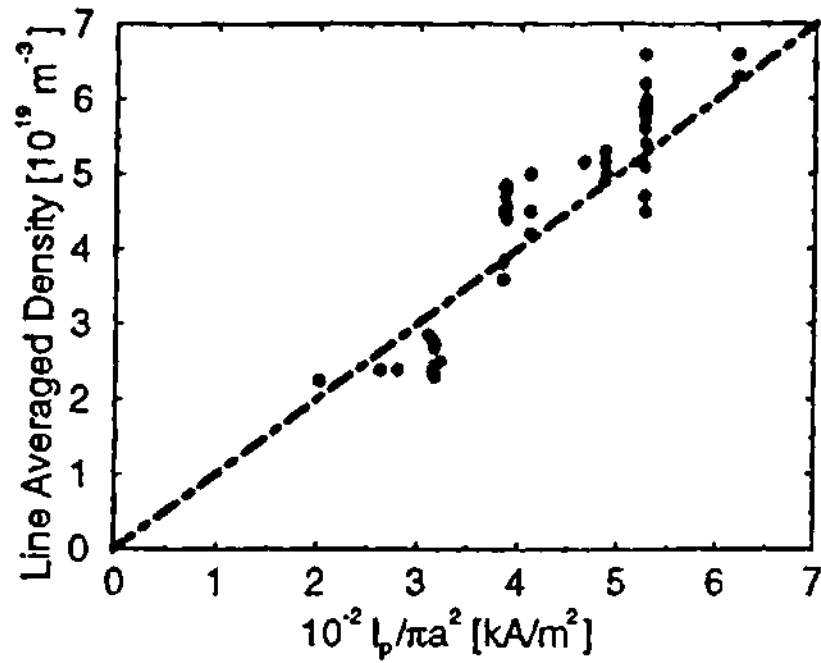


Figure 5.6 Disruptive density limit versus average current density for auxiliary heated TEXTOR discharges ($P_{aux} = 1.1\text{-}2.3$ MW). The chained line indicates the Greenwald limit.

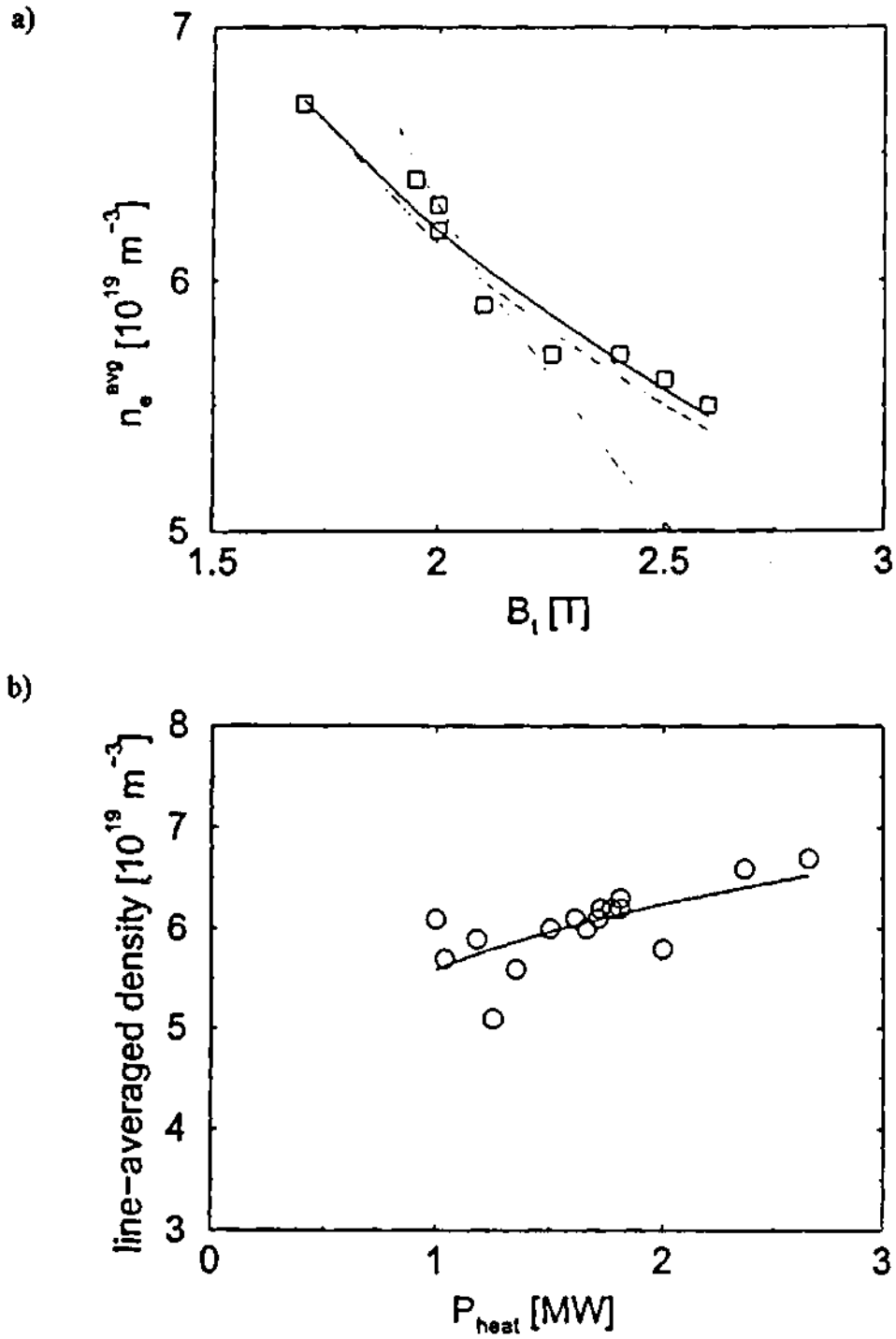


Figure 5.7 \bar{n}_e scaling with global parameters ($I_p = 350$ kA, $P_{NBI} = 1.4$ MW): a) toroidal magnetic field $n_e^{cr} \propto B_t^{-0.5}$ solid line, $n_e^{cr} \propto a + b \times B_t^{-0.5}$ dashed line, $n_e^{cr} \propto B_t^{-1}$ dash-dot line; b) heating power, $n_e^{cr} \propto P_{heat}^{0.16}$.

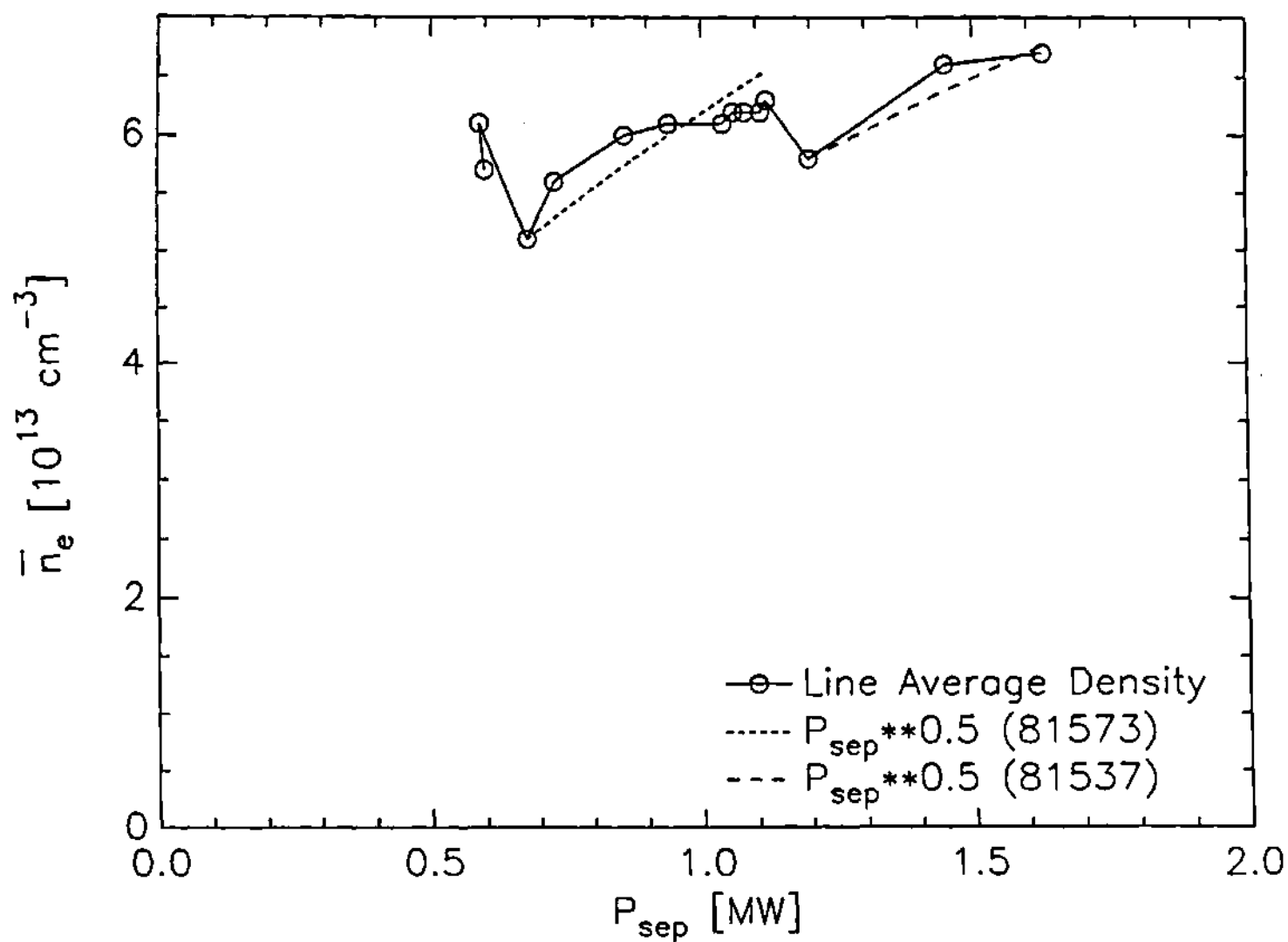


Figure 5.8 \bar{n}_e versus P_{sep} for shots 81531-81532, 81573-81581, 81537-81539 at MARFE onset ($I_p = 350 \text{ kA}$ and $B_T = 2.25 \text{ T}$).

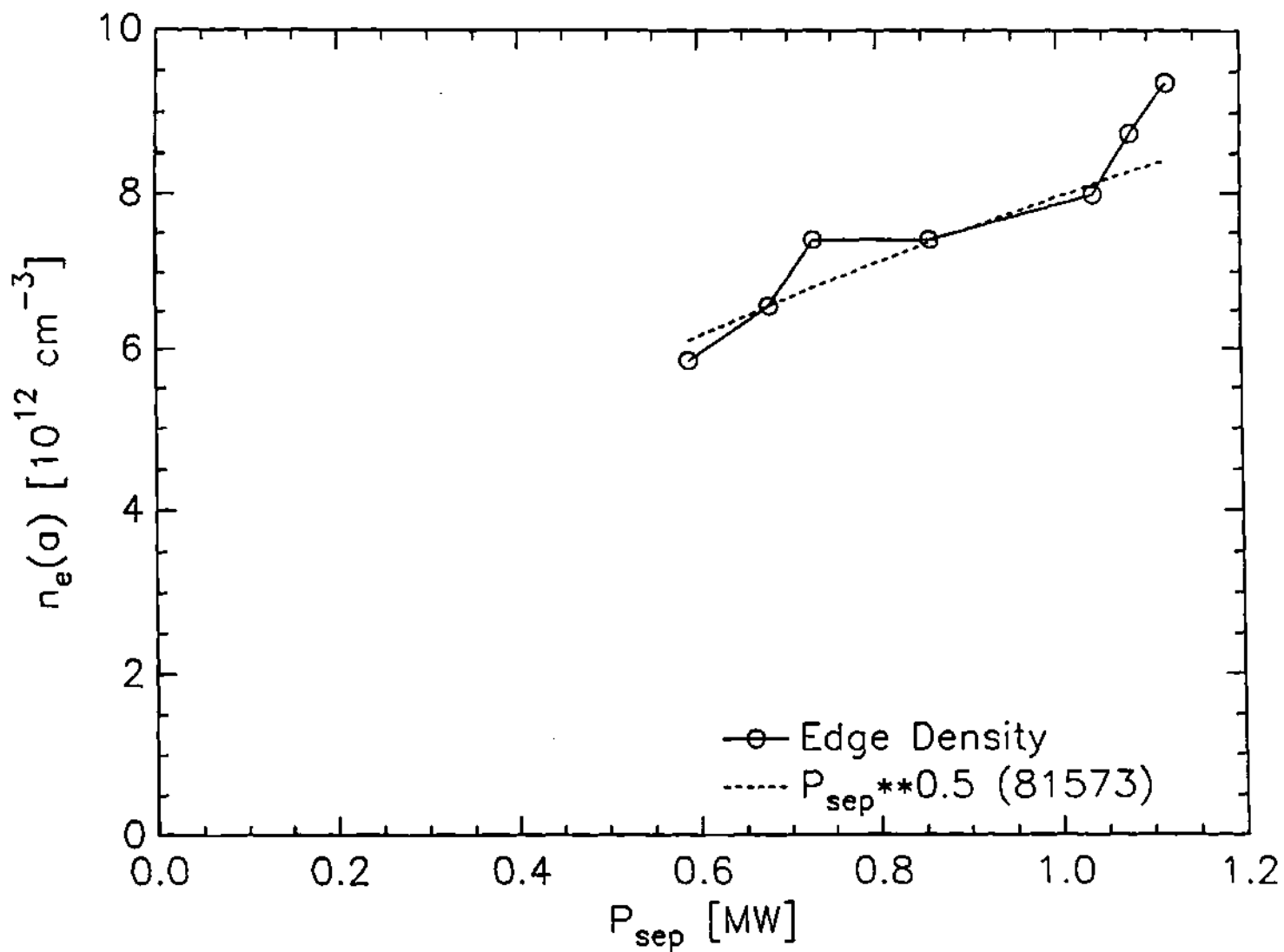


Figure 5.9 $n_e(a)$ versus P_{sep} for shots 81532, 81573-81575, 81577, 81579, 81581 at MARFE onset ($I_p = 350$ kA and $B_T = 2.25$ T).

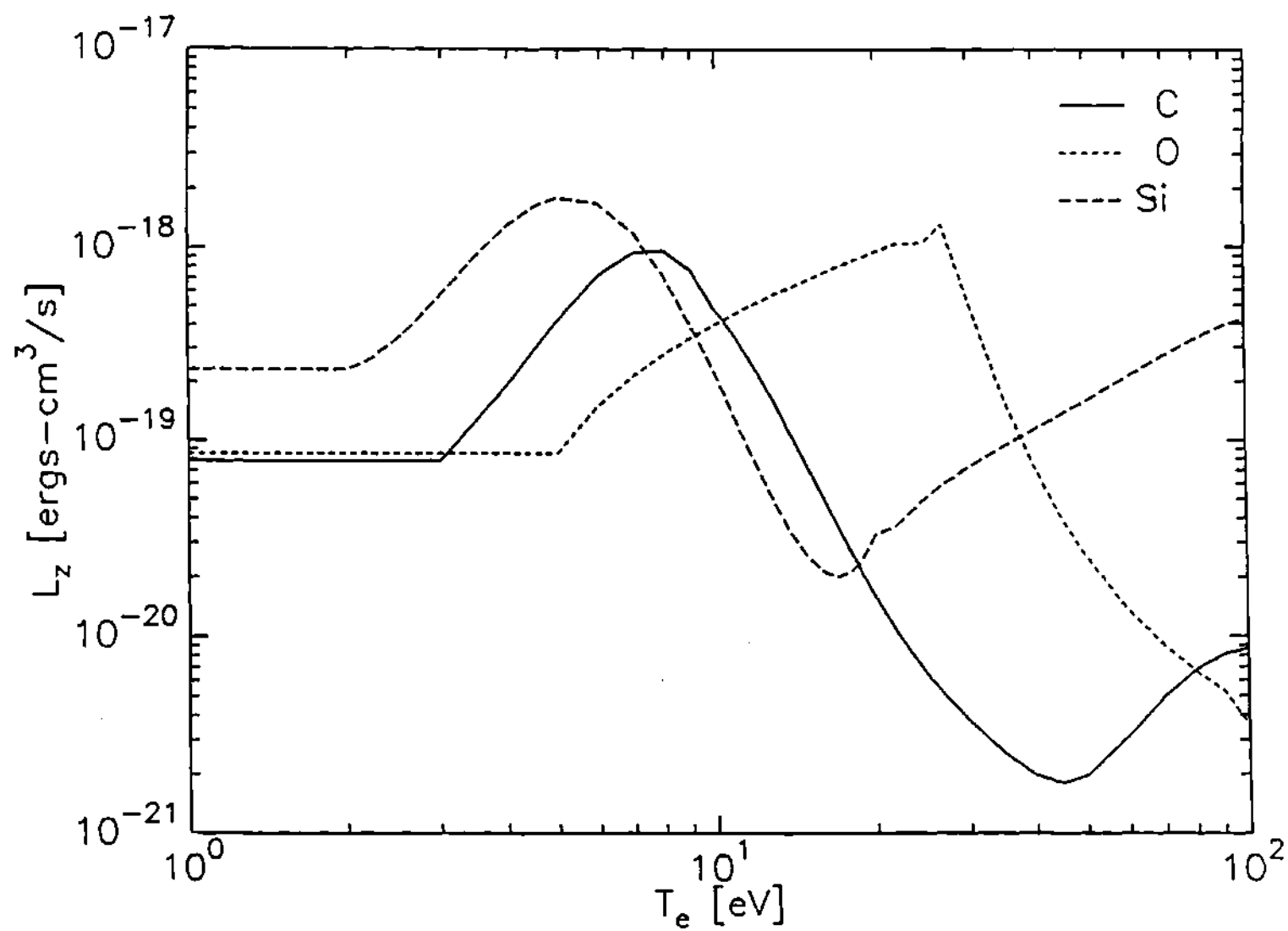


Figure 5.10 Radiative cooling rates of carbon, oxygen and silicon versus electron temperature.

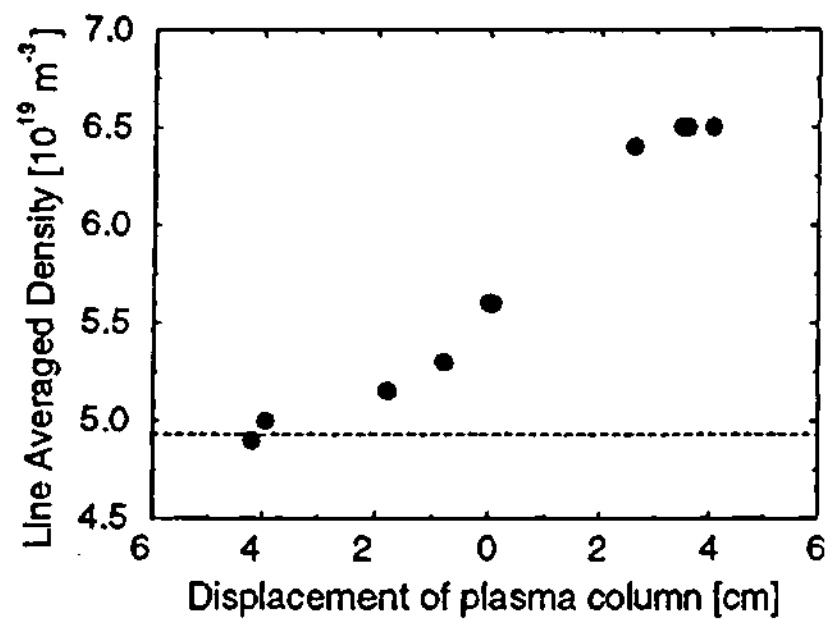


Figure 5.11 Dependence of the disruptive density limit on the horizontal plasma position ($I_p = 270 \text{ kA}$, $P_{aux} = 0.9\text{-}1.0 \text{ MW}$). The Greenwald limit is indicated by the dashed line.

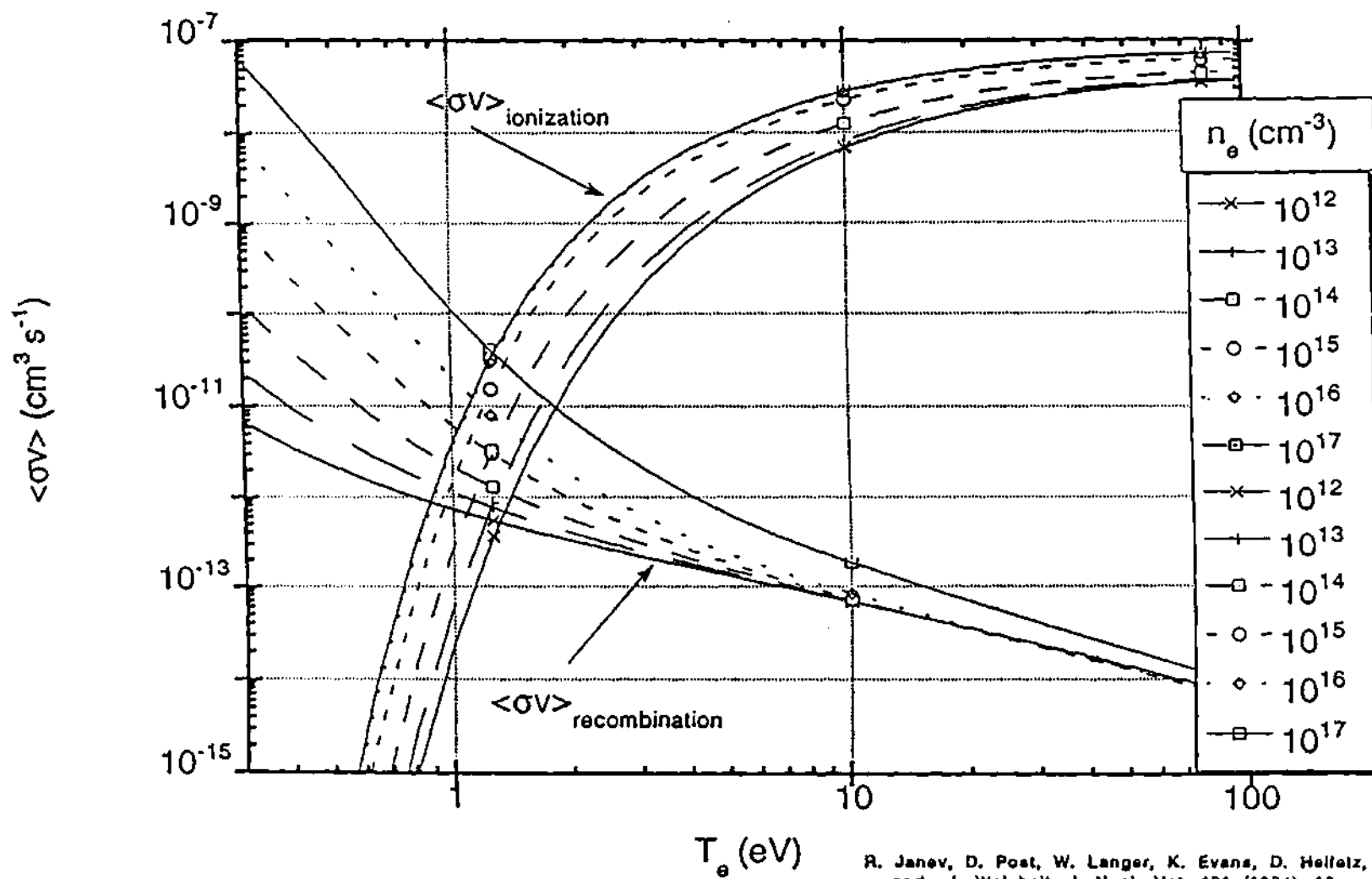


Figure 5.12 $\langle \sigma v \rangle (\text{cm}^3 \text{s}^{-1})$ for recombination and ionization.

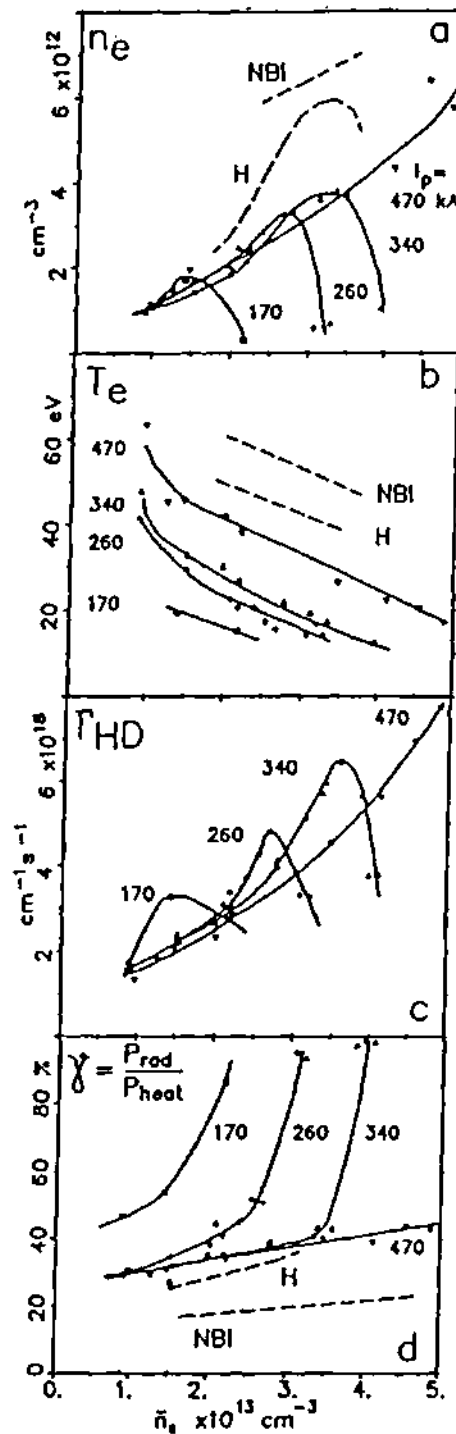


Figure 5.13 a) Local electron density, b) temperature, c) D/H flux at the limiter and d) global radiation level as a function of line-averaged electron density. The data for ohmic heating, $I_p = 340 \text{ kA}$ and deuterium filling are used as the reference case. The variation of parameters (plasma current, neutral beam heating "NBI" and hydrogen filling "H") with respect to the reference data are indicated.

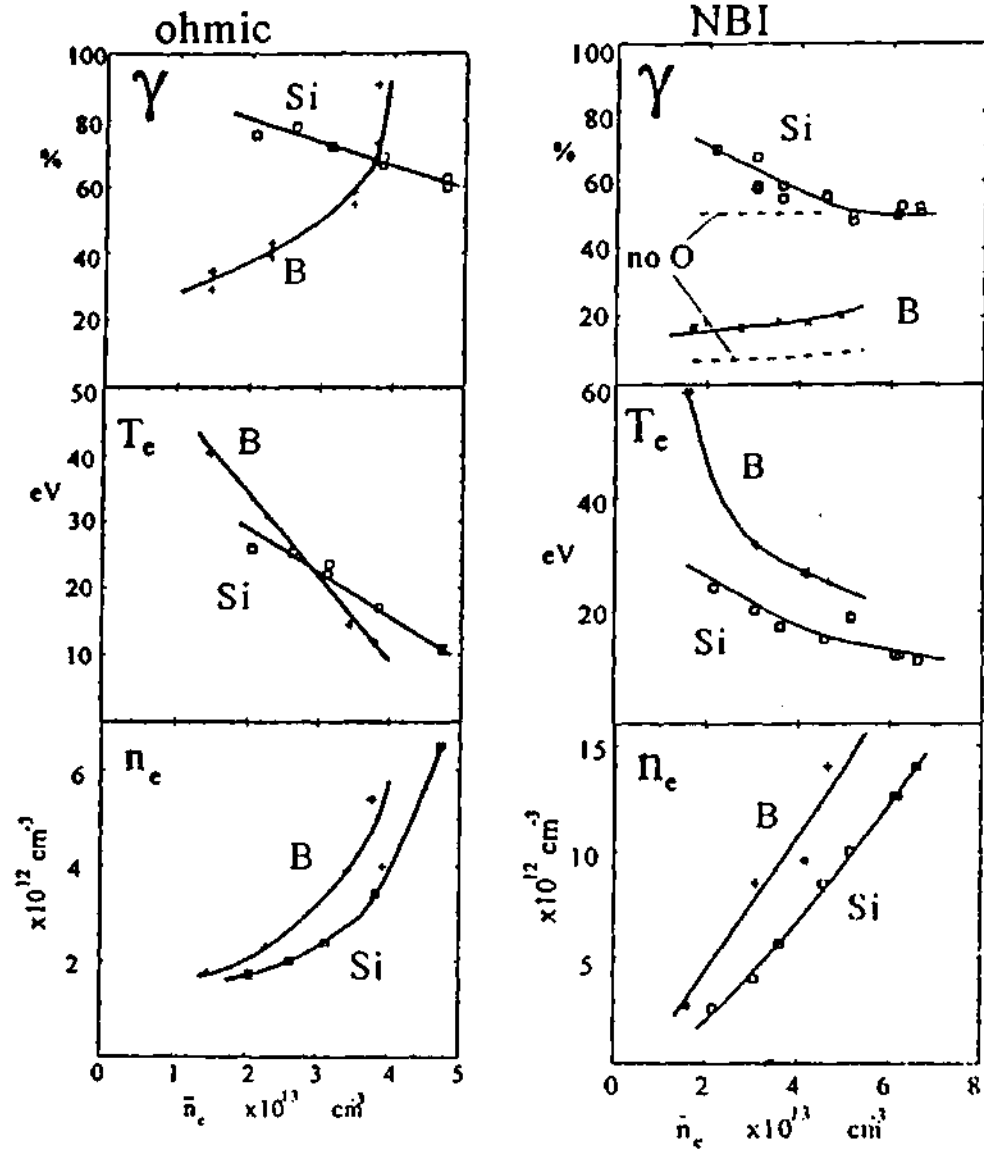


Figure 5.14 Variation of the plasma edge parameters n_e and T_e and the radiative fraction with line-average density, with and without auxiliary heating ($P_{\text{heat}} = 0.3/1.5 \text{ MW}$), and for siliconized and boronized conditions.

CHAPTER VI

DENSITY LIMITS OF FIRE (FUSION IGNITION RESEARCH EXPERIMENT)

6.1 Introduction

A modular approach to the next physics steps in magnetic fusion is envisioned as a burning plasma experiment and an advanced toroidal experiment running in parallel. The fusion plasma science objectives [6.1] for these physics experiments are:

“Burning Plasma Physics - The achievement and understanding of alpha-dominated plasmas that have characteristics similar to those expected in a fusion energy source, and

Advanced Toroidal Physics - The achievement and understanding of bootstrap-current-dominated plasmas with externally controlled profiles and other characteristics (e.g., confinement and β) similar to those expected in an attractive fusion system.”

These small, cost-effective experiments would then be followed by a physics integration experiment which would be built based on the knowledge gained in burning plasma physics and advanced toroidal physics.

The Fusion Ignition Research Experiment (FIRE) is a next-step burning plasma experiment option for the United States fusion program. The mission [6.2] of FIRE is to determine the conditions necessary to generate, control and sustain alpha-dominated tokamak plasmas. The effects of alpha-dominated heating on energy confinement,

pressure and density limits, profile control (including bootstrap current) and particle exhaust are of primary interest.

This chapter uses the density limit theories of Chapter 2 to predict the operational density limits for FIRE.

6.2 Analysis of MARFE Density Limit in FIRE

The latest (September 2000) FIRE parameters [6.3] available are given in Table 6.1. These parameters are based on 0-D spreadsheet models and 1½-D simulations. The baseline temperature and density profiles from 1½-D simulation [6.3] are shown in Figures 6.1 and 6.2, respectively. An analysis of the baseline parametric model [6.4] with the 2-D neutrals code GTNEUT indicates that the average edge neutral concentration will be less than 1×10^{-5} .

A series of studies were performed to determine the major factors affecting the MARFE density limit as defined in Eq. (2.5). The results are expressed in terms of the MARFE Index (Eq. 2.6). The nominal gradient scale lengths just inside the LCFS were determined from the baseline profiles (Figures 6.1 and 6.2) to be $\lambda_T = 2.7$ cm and $\lambda_n = 5.4$ cm. Since the edge profiles in the 1½-D model are dependent on uncertain boundary conditions, the gradient scale lengths are also uncertain, and the MARFE Index will be evaluated for a range of values of λ_T and λ_n .

The first study examined the MARFE Index, MI, as a function of neutral concentration in the edge transport barrier (~1 cm inside the last closed flux surface), f_0 .

Several values of the gradient scale lengths were considered. The result shown in Figure 6.3 indicates that MARFE onset is predicted ($MI > 1$) at about $f_0 = 4. \times 10^{-4}$ in the nominal case. Doubling and halving the gradient scale lengths effectively halve and double, respectively, the predicted neutral concentration at MARFE onset.

Table 6.1 Baseline FIRE Machine Parameters

| Parameter | Value |
|--|------------------------------|
| R_o , major radius | 2.0 m |
| a , minor radius | 0.525 m |
| B_o , field on axis | 10 T |
| κ_{95} , elongation | 1.77 |
| δ_{95} , triangularity | 0.40 |
| I_p , plasma current | 6.44 MA |
| P_{fus} , fusion power | 158 MW |
| P_{aux} , RF heating | 22 MW |
| Q | 7.2 |
| Z_{eff} | 1.4 |
| f_{Be} , beryllium fraction | 0.03 |
| f_α , thermal alpha fraction | 0.026 |
| $n_{e0}/\langle n_e \rangle$ | 1.24 |
| \bar{n}_e / n_{GW} | 0.70 |
| $\langle T \rangle_n$ | 6.9 (T_e), 6.6 (T_i) |
| $T_{i0}/\langle T_i \rangle_n$ | 2.8 |
| ITER IPB98(y,2) multiplier | 1.1 |
| $P_{out}/P_{L-H thr}$ | 1.95 |
| $P_{rad}(core)$ | 10.5 MW |
| $P_{out} = P_\alpha + P_{aux} - P_{rad}$ | 44.3 MW |
| $\tau_{flattop}$ | 20 s |
| τ_E | 0.6 s |

The second study examined the MI as a function of f_0 , while the baseline impurities (Be and He) were varied. The result shown in Figure 6.4 indicates that sensitivity to the baseline impurity concentrations is small.

The next studies examined the MI as a function of f_0 with the baseline helium concentration fixed and a second impurity varied up to 1/3 of its “fatal fraction.” Since iron and carbon are possible first-wall or divertor materials, and since neon injection may be considered for enhancing confinement or radiative power exhaust, beryllium, carbon, neon and iron impurities were considered. The fatal fraction of an impurity is the concentration above which ignition becomes impossible due to dilution and radiation losses from the central plasma (Table 6.2) [6.5]. In these calculations, the fusion and

Table 6.2 Maximum allowed impurity fractions for ignition.

| Z | 4 | 6 | 10 | 18 | 26 | 42 | 74 |
|----------------|-----|------|------|-------|-------|-------|--------|
| Fatal fraction | 14% | 6.7% | 2.4% | 0.54% | 0.25% | 0.11% | 0.011% |

radiated powers were calculated consistently with regard to the impurity concentration. However, the temperature and density profiles were assumed to remain unchanged from their baseline values shown in Figures 6.1 and 6.2.

Figures 6.5, 6.6, 6.7 and 6.8 show the MARFE Index as a function of the neutral concentration for beryllium, carbon, neon and iron, respectively. MARFE onset at 1/3 the

fatal fraction is reached at neutral concentrations of 3×10^{-4} , 2×10^{-5} , 4×10^{-4} and 1×10^{-4} for beryllium, carbon, neon and iron, respectively.

The MI is seen to increase rapidly with increasing carbon concentration in Figure 6.6. In our calculations, the radiative cooling rate for carbon was enhanced by the charge-exchange/recombination process in the presence of neutrals [6.6]. This process was not taken into account for the other impurities.

For iron concentrations near 1/3 the fatal fraction, the MI is seen to become flat, and the design edge density is near the MARFE density limit even for very low neutral concentrations, as shown in Figure 6.8. If the radiative cooling rate for iron were enhanced by neutrals, as was done for carbon, then it is very likely that the MARFE density limit will be exceeded, even for neutral fractions of 1×10^{-5} .

6.3 Analysis of Disruptive Density Limit in FIRE

The disruptive density limit of Eq. (2.7) was examined for concentrations of beryllium, carbon, neon and iron up to 1/3 the fatal fraction of each impurity. FIRE was thermally stable against radiative collapse for all impurities as long as the neutral concentration was below 1.3×10^{-3} . For f_0 above 1.3×10^{-3} , FIRE was unstable regardless of the impurity used. The disruptive density limit is clearly dominated by neutral cooling of the edge, not radiative cooling, for these impurities present in concentrations no larger than 1/3 their fatal fraction..

6.4 Transport Barrier Neutral Concentration in FIRE

The 2-D Transmission and Escape Probabilities (TEP) code GTNEUT [6.7] was used to calculate [6.4] the neutral distribution in the plasma edge of the baseline FIRE design. The GTNEUT code has been successfully benchmarked against the Monte Carlo method and experiment [6.8-6.9].

The edge plasma and first wall geometry, background plasma properties and expected ion fluxes to the inner and outer divertor plates were obtained from a UEDGE-DEGAS 2 simulation [6.4]. Up-down symmetry was assumed for the baseline Double-Null FIRE design. A relatively small number of computational regions were used to represent the edge plasma in GTNEUT, since the TEP method is believed to provide accurate values of the average neutral density using only a few large regions. The computational regions just inside the separatrix extend a few centimeters inside the separatrix, and the calculated neutral densities represent an average value over this radial extent. The edge geometry and the GTNEUT computational regions are shown in Figure 6.9.

In Figure 6.10a [6.4], the neutral density is plotted versus the normalized region number for the regions that are located inside the separatrix, starting from the inner midplane location. The computed neutral densities are in qualitative agreement with the neutral densities predicted by the DEGAS 2 code [6.4].

The MARFE analysis discussed above pertains to the edge transport barrier region, which extends about a centimeter inside the separatrix. Since the neutral density

attenuates rapidly with distance into the FIRE plasma, the average neutral densities shown in Figure 6.10a may be as much as an order of magnitude smaller than the average neutral densities in the transport barrier.

In Figure 6.10b [6.4], the net neutral flux from the edge to the core plasma is plotted versus the normalized region number (same numbering as in Figure 6.10a). These fluxes represent the net neutral influx into the core due to edge recycling under the assumption of no active pumping in the divertor. The total ion flux is about 1.4×10^{21} #/s. For comparison, the average particle loss rate for the baseline FIRE parameters, assuming that $\tau_p = 5\tau_E$, is estimated to be equal to 3.5×10^{21} #/s [6.4].

6.5 Discussion and Conclusions

Since MARFE growth rates are typically 10^{-4} /s, ions and electrons will move a considerable distance along field lines while a MARFE is forming. This implies that an average f_0 along the field lines should be used in evaluating the MARFE index. Taking into account that the field lines in the vicinity of the X-point are quite long, the poloidal neutral density distribution shown in Figure 6.10a, and the fact that the neutral density in the transport barrier may be an order of magnitude greater than the neutral density shown in Figure 6.10a, we conservatively estimate $n_0 \approx 10^{15} - 10^{16}$ #/m³ or $f_0 \approx 10^{-5} - 10^{-4}$, for the purpose of evaluating the MARFE index.

Our principal conclusion is that the nominal operating densities for the FIRE design should be achievable without encountering MARFE or radiative collapse density

limit phenomena. Figures 6.3 - 6.5 indicate stability against MARFE formation ($MI < 1$) for the baseline design parameters and impurities, for $f_0 < 10^{-4}$. Radiative collapse is not predicted for $f_0 < 10^{-3}$. This conclusion could change if the radiative cooling rate for beryllium was found to be enhanced by charge-exchange/recombination, as is the case for carbon.

A second, tentative, conclusion is that MARFEs could impose a density limit less than the present design value if the design was changed to have carbon or stainless steel plasma facing components, as indicated in Figures 6.6 and 6.8.

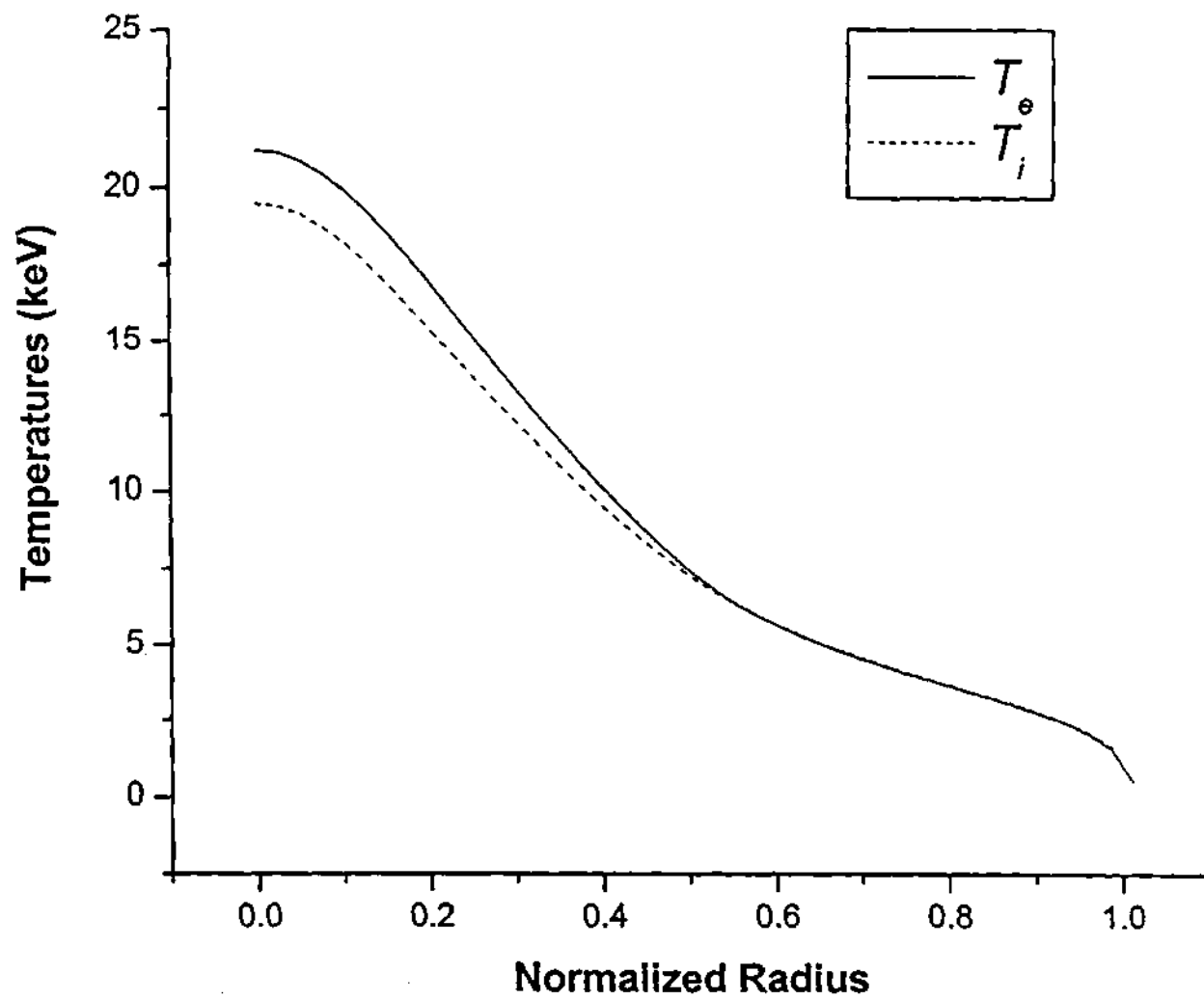


Figure 6.1 FIRE baseline ion and electron temperature profiles.

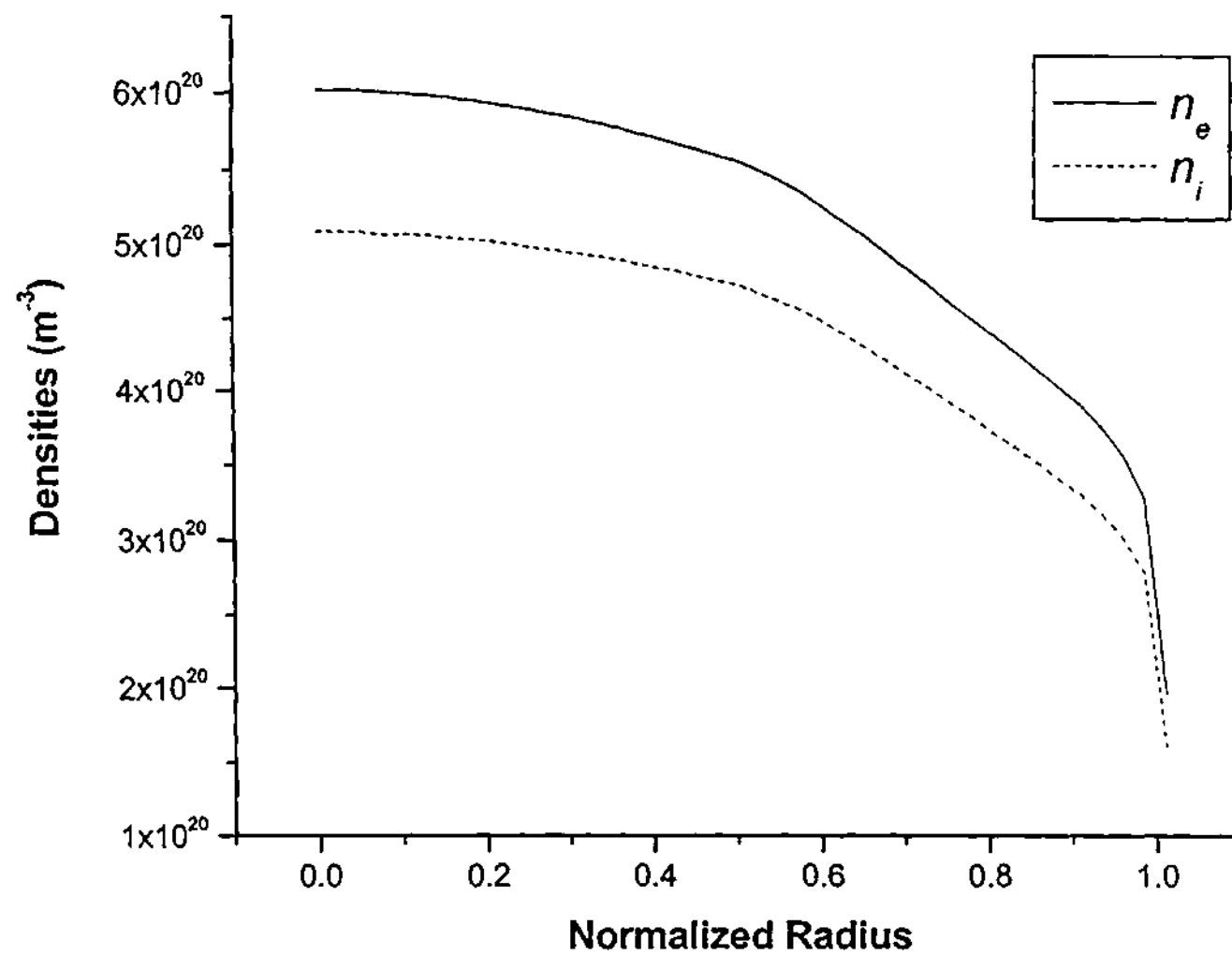


Figure 6.2 FIRE baseline ion and electron density profiles.

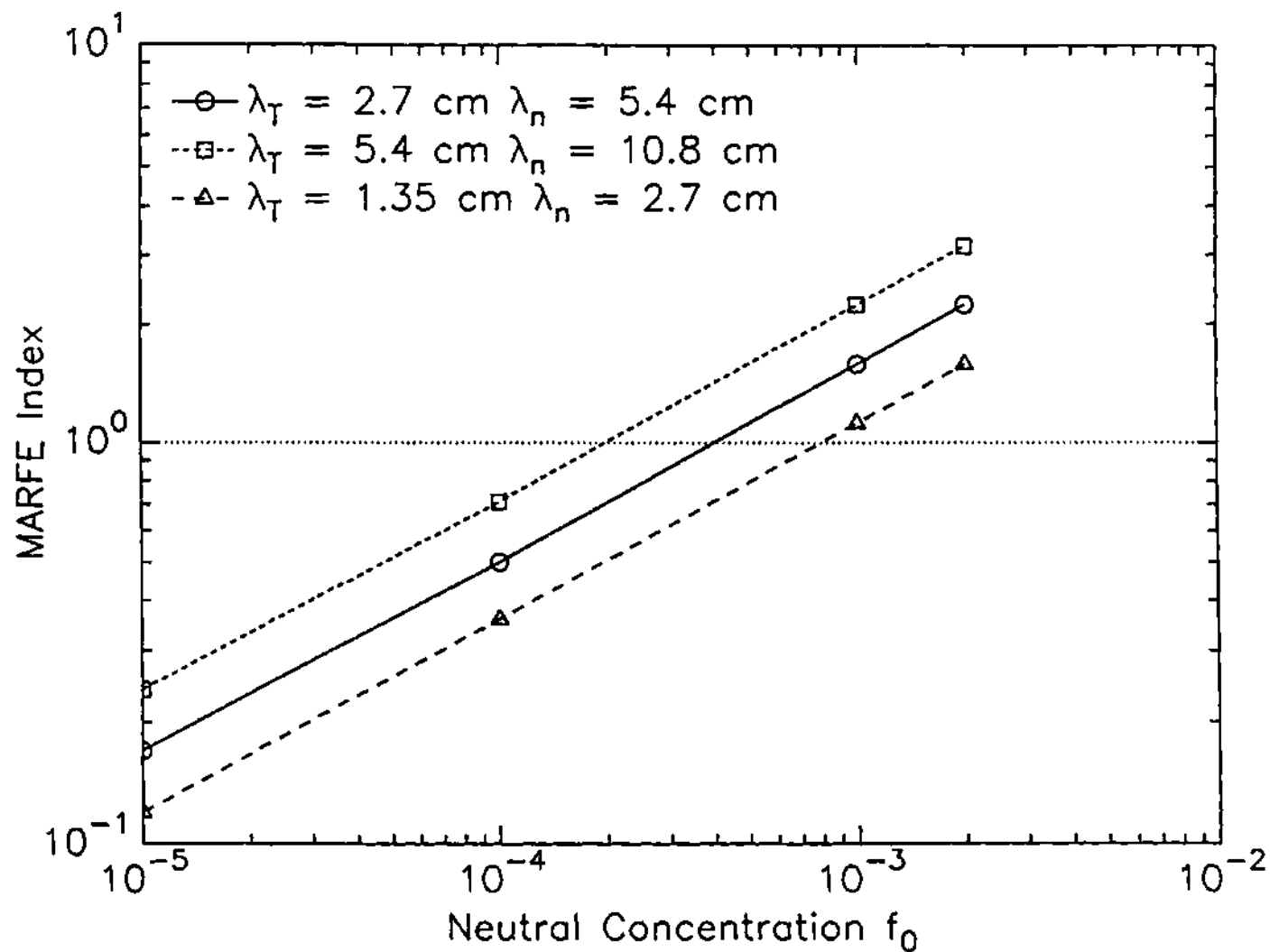


Figure 6.3 MARFE Index versus neutral fraction for FIRE with varied λ 's.

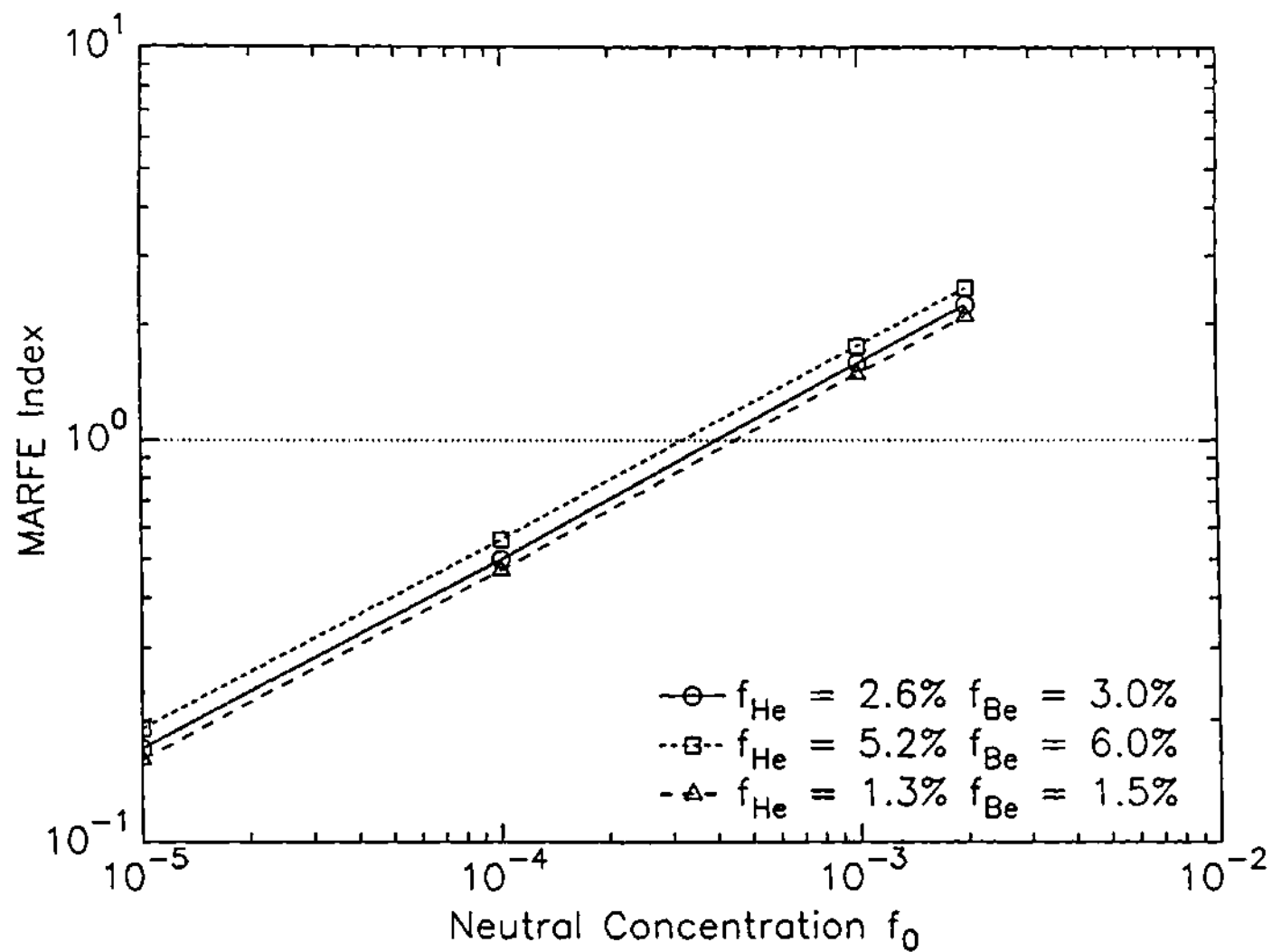


Figure 6.4 MARFE Index versus neutral fraction for FIRE with varied impurities.

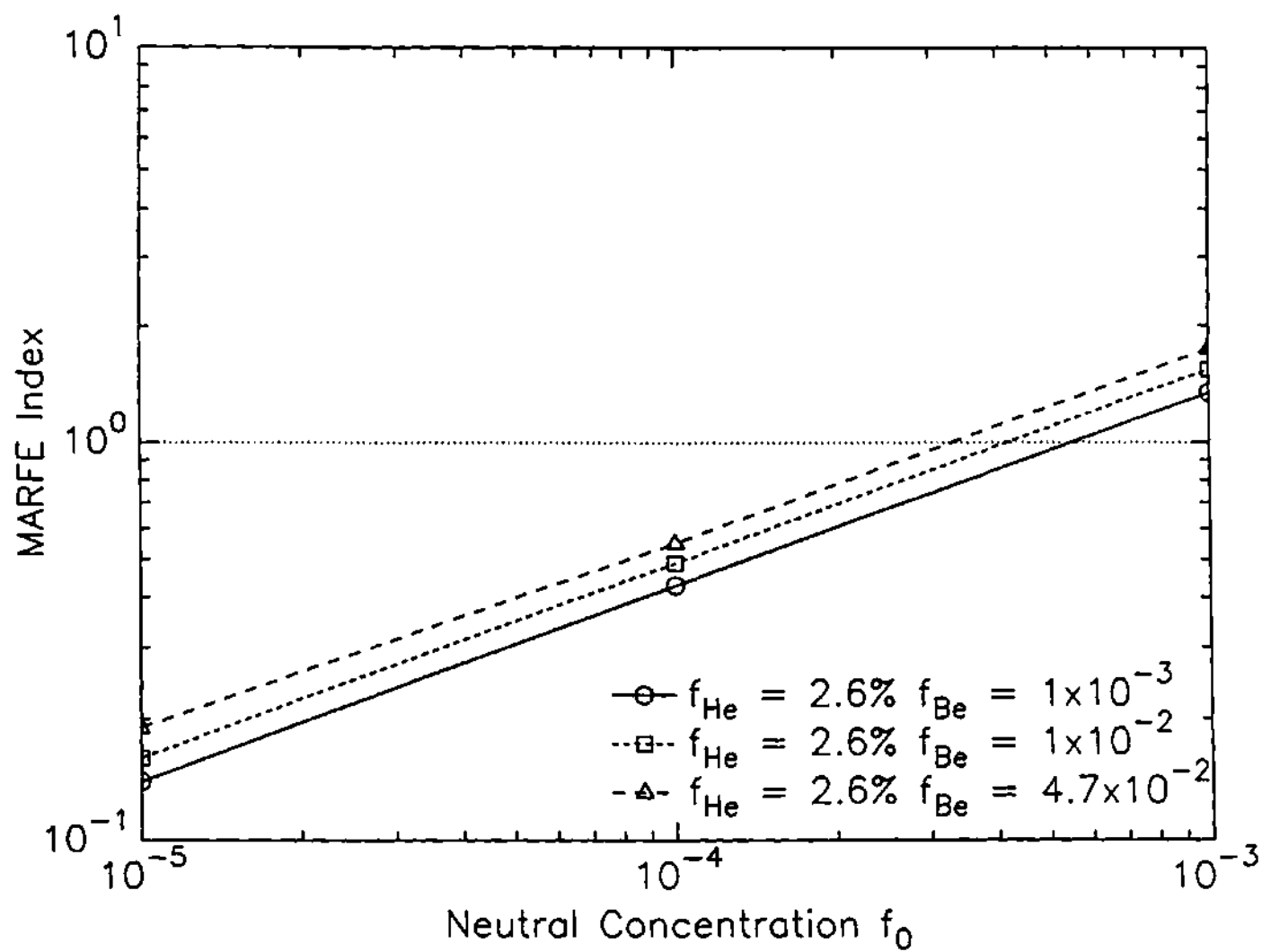


Figure 6.5 MARFE Index versus neutral fraction for FIRE with varied beryllium concentration.

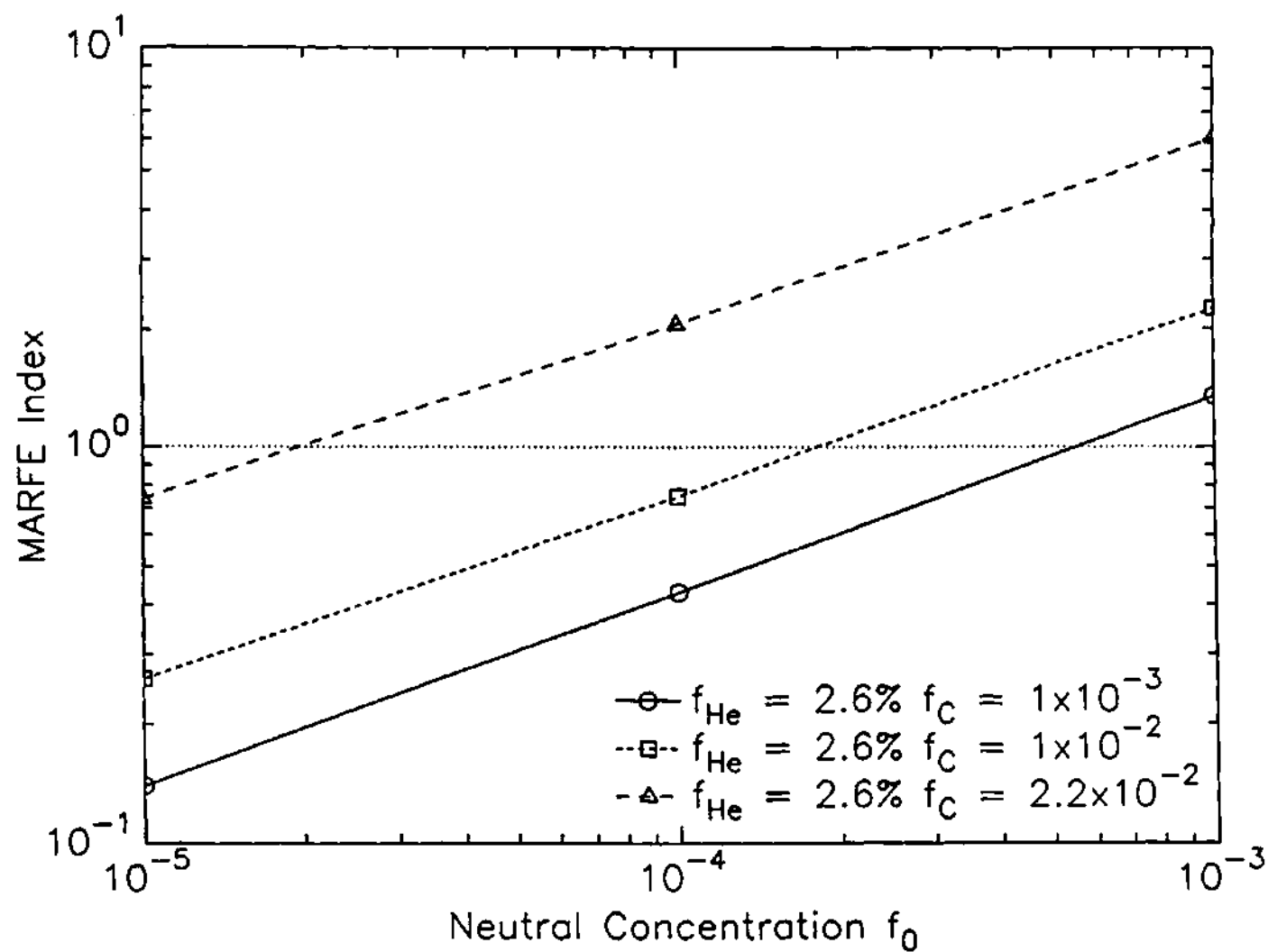


Figure 6.6 MARFE Index versus neutral fraction for FIRE with varied carbon concentration.

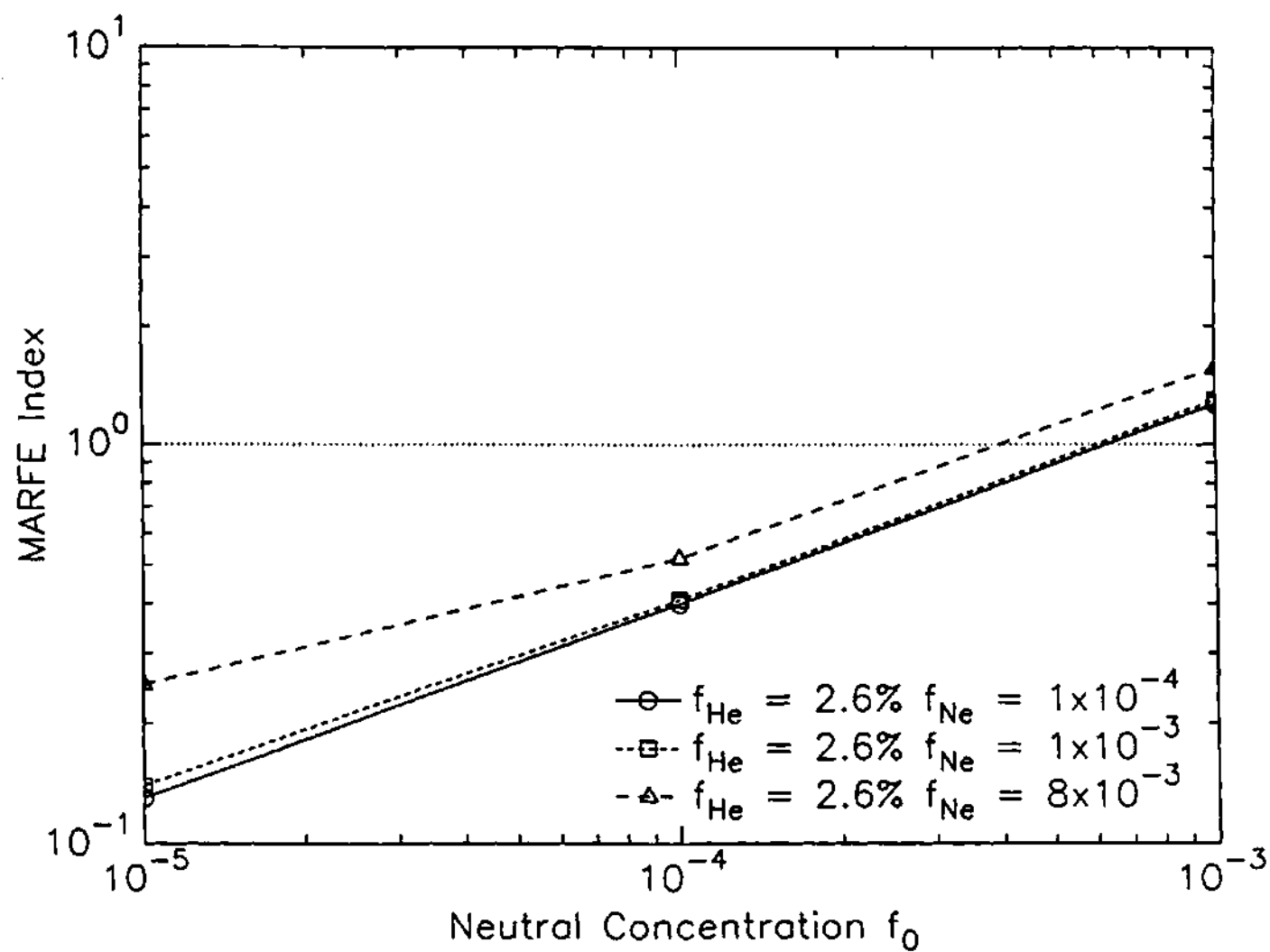


Figure 6.7 MARFE Index versus neutral fraction for FIRE with varied neon concentration.

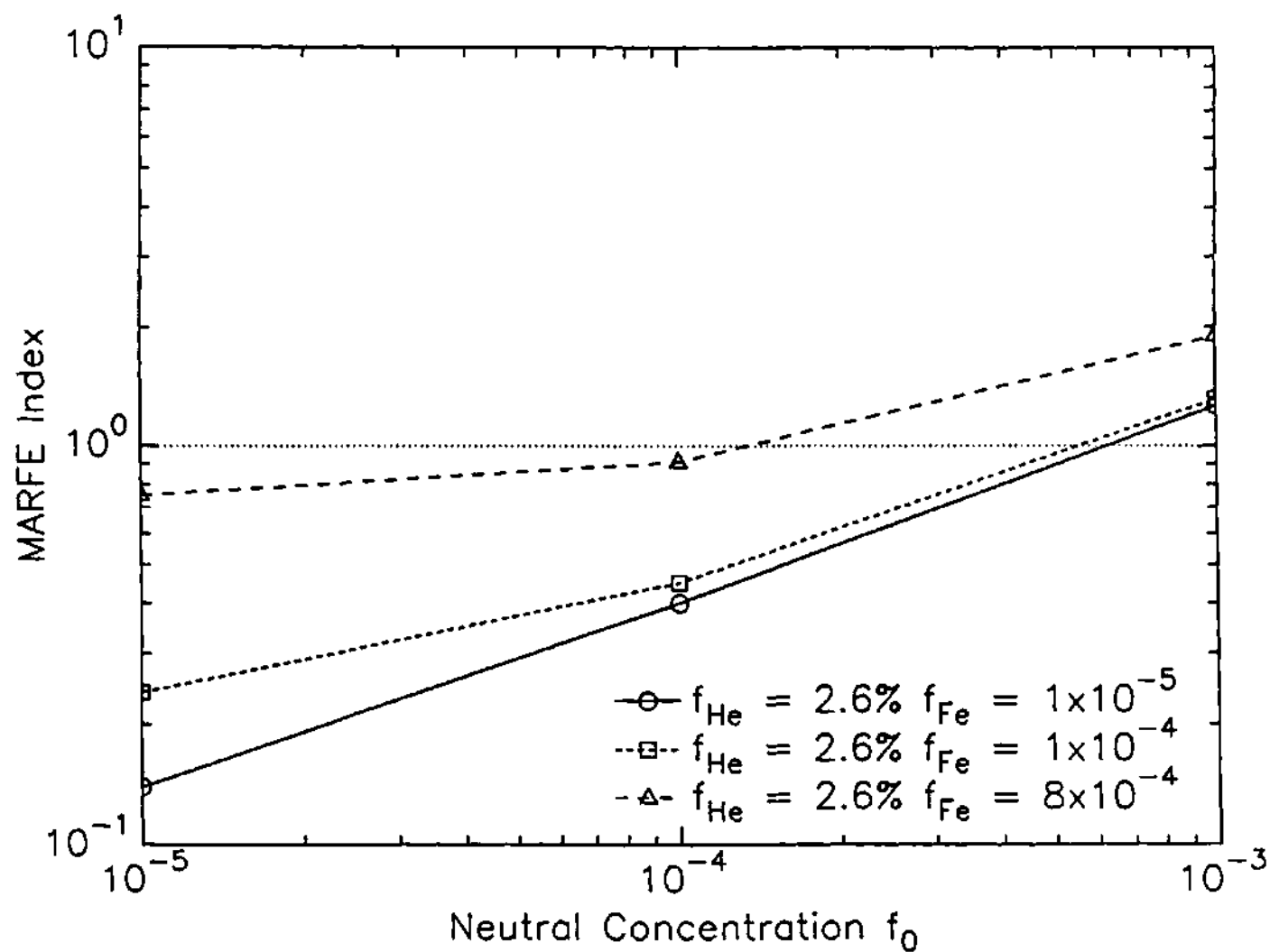
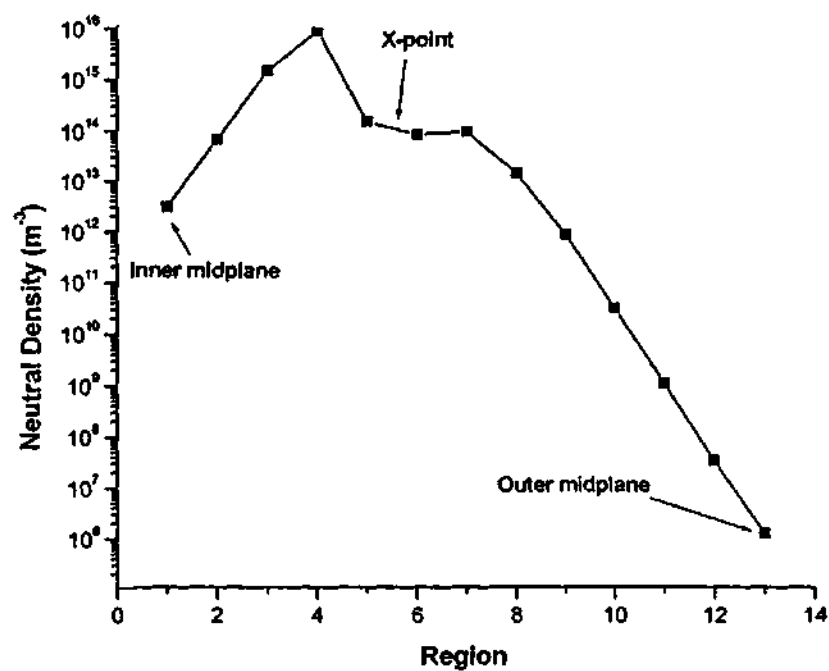


Figure 6.8 MARFE Index versus neutral fraction for FIRE with varied iron concentration.

Figure 6.9 FIRE lower divertor edge geometry and GTNEUT computational regions.

a)



b)

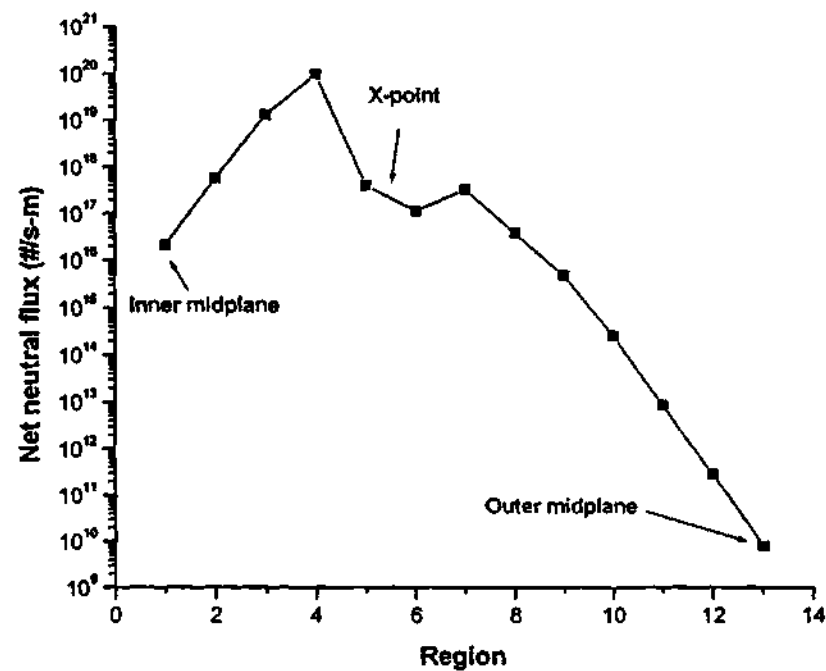


Figure 6.10 a) Neutral densities in the regions just inside the FIRE separatrix and b) net neutral influx from edge to core from regions inside the separatrix.

CHAPTER VII

SUMMARY AND CONCLUSIONS

A series of density limit shots in the TEXTOR tokamak that ended in MARFEs have been analyzed and compared with thermal instability theory of MARFE onset. The analysis included the reduction and correction of measured data to construct the parameters appearing in the predictive algorithm, as well as the calculation of the penetration of neutral gas sources at the various surfaces of the plasma chamber into the plasma edge.

The thermal instability theory predicts a critical value of the density on closed flux surfaces just inside the separatrix at which MARFE onset occurs. The onset of the MARFE was investigated in a number of TEXTOR shots in which neutral beam heating and continuous gas fueling were used to achieve high density, with the objective of comparing the measured edge density at MARFE onset with the predicted maximum edge density before MARFE onset.

In a power scan over which the neutral beam heating varied from 0.61 MW to 2.33 MW, the measured line-average and edge electron densities at MARFE onset varied from $5.1 \times 10^{19} \text{ m}^{-3}$ and $5.8 \times 10^{18} \text{ m}^{-3}$ to $6.7 \times 10^{19} \text{ m}^{-3}$ and $9.4 \times 10^{18} \text{ m}^{-3}$, respectively, and the edge electron temperature varied from 28 eV to 35 eV.

MARFE onset ($MI > 1$) was predicted for the experimental conditions measured just prior to the observed MARFE onset in 8 out of 10 shots in the power scan using our best estimate of the experimental parameters. A prediction of MARFE onset ($MI > 1$) fell within the experimental uncertainty for all shots in the power scan. The conditions for MARFE onset occurred for a combination of small values of $\chi L_T^{-2} = Q_{\perp} L_T^{-1} / n T$ and large values of $n f_z L_z / T$ and $n f_0 L_0 / T$ in the plasma edge, where L_z is the radiative cooling rate and L_0 represents an equivalent rate for ionization/charge-exchange/elastic-scattering cooling of the edge plasma. The agreement between predicted and measured MARFE onset over a range of values of the edge parameters, lends confidence to the interpretation of the MARFE as a thermal instability in the plasma edge.

The parametric dependence of the wider body of TEXTOR density limit experiments was compared with the parametric dependence for MARFE onset and radiative collapse predicted by thermal instability theory. This comparison required the development of expressions relating the global plasma parameters, in terms of which the experimental density limits were correlated, to the physics parameters that enter the thermal instability theory. The measured MARFE line-averaged density limits scaled linearly with current ($n \sim I$), as the inverse square root of the magnetic field ($n \sim B^{-0.5}$) and as the square root of the auxiliary heating power ($n \sim P_{aux}^{0.5}$). The theoretical predictions of the MARFE density limit agreed well with the B- and P-scalings, but not obviously with the I-scaling. There is evidence of a strong dependence of the density profile on I which

cannot be taken into account, and this profile dependence may account for the failure to obtain qualitative agreement on the current scaling.

The measured MARFE line-averaged density dependence on wall material and on plasma position within the chamber can be qualitatively explained by the differences in the impurity and neutral concentrations in the plasma edge, i.e. changes in f_z and f_0 .

The measured density limit in shots which suffer radiative collapse can be described by an expression which scales as the square root of the ratio of the heating power to the impurity content. The theoretical disruptive thermal instability density limit formula has the same form. In particular, both formulas predict $n \sim I$ scaling for ohmic heated plasmas. We surmise, as discussed above for the MARFE parameter dependence, that there may exist a strong dependence of the density profile on I which accounts for the current scaling observed in auxiliary heated discharges.

The difference between shots that MARFE (auxiliary heated and low- Z_{eff} ohmic shots) and shots that detach symmetrically and disrupt (most ohmic and some high Z_{eff} auxiliary heated shots) can be attributed to the fact that in the latter the predicted MARFE edge density limit decreases with decreasing edge temperature (for a temperature range where dL_z/dT is negative) and becomes smaller than the actual edge density before the edge becomes cool enough to detach, whereas in the former the edge density exceeds the MARFE density limit before the edge becomes cool enough to detach.

Finally, the thermal instability theory was applied to predict density limits for the next-step burning plasma experiment (FIRE) conceptual design. An analysis of the neutral

density in the edge of FIRE predicted neutral concentrations in the range 10^{-5} - 10^{-4} . For the baseline design parameters, FIRE was predicted to be stable against MARFEs and stable against disruptive collapse for neutral concentrations below 10^{-4} and 10^{-3} , respectively. The introduction of higher Z impurities (carbon, neon, and iron) up to 1/3 the fatal fraction still resulted in predictions of stability against MARFEs and disruptive collapses, but the safety margin grew smaller. These latter conclusions must be qualified by the fact that the radiative cooling rates for beryllium, neon and iron were not enhanced by charge-exchange /recombination, as were the rates for carbon.

REFERENCES

Chapter 1

- 1.1 M. Greenwald, et al., Nucl. Fusion **28** (1988) 2199.
- 1.2 T. W. Petrie, et al., Nucl. Fusion **33** (1993) 929.
- 1.3 R. Maingi, et al., Phys. Plasmas **4** (1997) 1752.
- 1.4 M. A. Mahdavi, et al., 24th EPS Conf. on Contr. Fusion and Plasma Physics, Berchtesgaden **21A** Part III (1997) 1113.
- 1.5 T. W. Petrie, et al., J. Nucl. Mater. **241-243** (1997) 639.
- 1.6 W. M. Stacey, et al., Phys. Plasmas **6** (1999) 3941.
- 1.7 W. M. Stacey and T. W. Petrie, Phys. Plasmas **7** (2000) 4931.
- 1.8 G. Waidmann and G. Kuang, Nucl. Fusion **32** (1992) 645.
- 1.9 P. C. de Vries, et al., Phys. Rev. Lett. **80** (1998) 3519.
- 1.10 J. Rapp, et al., Nucl. Fusion **39** (1999) 765.
- 1.11 J. Rapp, et al., 26th EPS Conf. on Contr. Fusion and Plasma Physics, Maastricht **23J** (1999) 665.
- 1.12 H. R. Koslowski, Fusion Techn. **37** (2000) 85.
- 1.13 V. Mertens, et al., Nucl. Fusion **37** (1997) 1607.
- 1.14 V. Mertens, et al., 26th EPS Conf. on Contr. Fusion and Plasma Physics, Maastricht **23J** (1999) 1397.

- 1.15 V. Mertens, et al., Nucl. Fusion **40** (2000) 1839.
- 1.16 J. Stober, et al., Plasma Phys. Control. Fusion **42** (2000) A211.
- 1.17 C. G. Lowry, et al., 17th EPS Conf. Contr. Fusion and Plasma Heating, Amsterdam (1990) 339.
- 1.18 J. A. Wesson, et al., Nucl. Fusion **29** (1989) 641.
- 1.19 C. F. Maggi, et al., Nucl. Fusion **39** (1999) 979.
- 1.20 JET Team, Nucl. Fusion **39** (1999) 1687.
- 1.21 G. F. Matthews, et al., J. Nucl. Mater. **266-269** (1999) 1134.
- 1.22 W. Suttrop, et al., Plasma Phys. Control. Fusion **39** (1997) 2051.
- 1.23 R. J. Goldston, in New Ideas in Tokamak Confinement, ed. M. N. Rosenbluth, AIP Press (1994) 39.
- 1.24 N. Ohya, Nucl. Fusion **19** (1979) 1491.
- 1.25 D. E. T. F. Ashby and M. H. Hughes, Nucl. Fusion **21** (1981) 911.
- 1.26 W. M. Stacey, Phys. Plasmas **3** (1996) 1012.
- 1.27 W. M. Stacey, Phys. Plasmas **4** (1997) 1069.
- 1.28 F. C. Schüller, Plasma Phys. Contr. Fusion **37** (1995) A135.
- 1.29 K. Borrass, Nucl. Fusion **31** (1991) 1035.
- 1.30 K. Borrass, Nucl. Fusion **33** (1993) 63.
- 1.31 K. Borrass, Nucl. Fusion **37** (1997) 1523.
- 1.32 J. Neuhauser, W. Schneider, R. Wunderlich, Nucl. Fusion **26** (1986) 1679.
- 1.33 J. F. Drake, Phys. Fluids **30** (1987) 2429.

- 1.34 W. M. Stacey, Phys. Plasmas **3** (1996) 2673.
- 1.35 W. M. Stacey, Phys. Plasmas **3** (1996) 3032.
- 1.36 W. M. Stacey, Phys. Plasmas **4** (1997) 134.
- 1.37 W. M. Stacey, Phys. Plasmas **4** (1997) 242.
- 1.38 W. M. Stacey, Plasma Phys. Contr. Fusion **39** (1997) 1245.
- 1.39 W. M. Stacey, Fusion Techn. **36** (1999) 38.
- 1.40 W. M. Stacey, Phys. Plasmas **7** (2000) 3464.

Chapter 2

- 2.1 B. Lipschultz, B. LaBombard, E. S. Marmor, M. M. Pickrell, J. L. Terry, Nucl. Fusion **24** (1984) 977.
- 2.2 B. Lipschultz, J. Nucl. Mater. **145-147** (1987) 15.
- 2.3 J. Neuhauser, W. Schneider, and R. Wunderlich, Nucl. Fusion **26** (1986) 1679.
- 2.4 J. F. Drake, Phys. Fluids **30** (1987) 2429.
- 2.5 S. R. Choudhury and P. K. Kaw, Phys. Fluids B **1** (1989) 1646.
- 2.6 H. Capes, Ph. Ghendrih, A. Samain, A. Grosman, and J. P. Morera, Plasma Phys. Controlled Fusion **32** (1990) 103.
- 2.7 P. Kaw, S. Deshpande, K. Avinash, and S. Rath, Phys. Rev. Lett. **65** (1990) 2873.
- 2.8 W. M. Stacey, Phys. Plasmas **3** (1996) 2673; **3** (1996) 3032; **4** (1997) 134; **4** (1997) 242; Fusion Technology **36** (1999) 38.

- 2.9 A. De Ploey, M. Goossens, and R. A. M. Van der Linden, *Phys. Plasmas* **1** (1994) 2623.
- 2.10 A. De Ploey, R. A. M. Van der Linden, G. T. A. Huysmans, M. Goossens, W. Kerner, and J. P. Goedbloed, *Plasma Phys. Controlled Fusion* **39** (1997) 423.
- 2.11 M. Z. Tokar, J. Rapp, D. Reiser, U. Samm, F. C. Schüller, G. Sergienko, and P. C. de Vries, *J. Nucl. Materials* **266-269** (1999) 958.
- 2.12 A. N. Simakov and S. I. Krasheninnikov, *Phys. Plasmas* **7** (2000) 950.
- 2.13 W. M. Stacey, *Plasma Phys. Controlled Fusion* **39** (1997) 1245.
- 2.14 W. M. Stacey, *Phys. Plasmas* **6** (1999) 2452.
- 2.15 N. Ohya, *Nucl. Fusion* **9** (1979) 1491.
- 2.16 D. E. T. F. Ashby and M. H. Hughes, *Nucl. Fusion* **21** (1981) 911.
- 2.17 W. M. Stacey, *Phys. Plasmas* **3** (1996) 1012.
- 2.18 W. M. Stacey, *Phys. Plasmas* **4** (1997) 1069.
- 2.19 K. Borrass, R. Schneider, and R. Fanengo, *Nucl. Fusion* **37** (1997) 1523.
- 2.20 K. Borrass, D. J. Campbell, S. Clement, and G. C. Vlasses, *Nucl. Fusion* **33** (1993) 63.
- 2.21 K. Borrass, *Nucl. Fusion* **31** (1991) 1035.
- 2.22 R. Hulse, *Nucl. Technol./Fusion* **3** (1983) 259.
- 2.23 D. E. Post, *J. Nucl. Mater.* **220-222** (1995) 143.
- 2.24 M. Keilhacker, R. Simonini, A. Taroni, and M. L. Watkins, *Nucl. Fusion* **32** (1991) 535.

- 2.25 W. M. Stacey, M. A. Mahdavi, R. Maingi and T. W. Petrie, *Phys. Plasmas* **6** (1999) 3941.
- 2.26 W. M. Stacey and T. W. Petrie, *Phys. Plasmas* **7** (2000) 4931.

Chapter 3

- 3.1 H. Soltwisch, et al., *Plasma Phys. Controlled Fusion* **26** (1984) 23.
- 3.2 E. Hintz, et al., in *Contributions to High-Temperature Plasma Physics*, edited by K. H. Spatschek and J. Uhlenbusch, Akademik Verlag, Berlin (1994) 373.
- 3.3 J. Rapp, et al., *Nucl. Fusion* **39** (1999) 765.
- 3.4 B. Schweer, M. Brix and M. Lehnen, *J. Nucl. Fusion* **266-269** (1999) 673.
- 3.5 A. M. Messiaen and P. E. Vandenplas, in *Contributions to High-Temperature Plasma Physics*, edited by K. H. Spatschek and J. Uhlenbusch, Akademik Verlag, Berlin (1994) 373.
- 3.6 A. Krämer-Flecken and G. Waidmann, in *Electron Cyclotron Emission and Electron Cyclotron Heating (Proc. 10th Joint Workshop, Ameland, 1997)* World Scientific Publishing, Singapore (1997) 209.
- 3.7 M. Lehnen, et al., 14th PSI, Rosenheim (to be published *J. Nucl. Mater.*, 2001).
- 3.8 A. Huber, et al., *Plasma Phys. Control. Fusion* **42** (2000) 569.
- 3.9 A. Pospieszczyk, et al., *J. Nucl. Mater.* **176-177** (1990) 180.
- 3.10 D. S. Gray, et al., *Control. Fusion and Plasma Phys., Proc. Euro. Conf. (Lisboa)* **17C** (1993) II-679.

- 3.11 P. Bogen and E. Hintz, in "Physics of Plasma-Wall Interactions in Controlled Fusion," Eds. D. E. Post and R. Behrisch (Plenum New York, 1986) p. 211.
- 3.12 J. Rapp, personal communication (1999-2000).
- 3.13 D. S. Gray, et al., Nucl. Fusion **38** (1998) 1585.
- 3.14 B. Unterberg, et al., J. Nucl. Mater. **241-243** (1997) 793.
- 3.15 B. Unterberg, et al., Control. Fusion and Plasma Phys., Proc. Euro. Conf. (Lisboa) **17C** (1993) II-663.
- 3.16 U. Samm, et al., J. Nucl. Mater. **162-164** (1989) 24.
- 3.17 H. Gerhauser and H. A. Claassen, Control. Fusion and Plasma Phys., Proc. Euro. Conf. (Lisboa) **17C** (1993) 835.
- 3.18 M. Lehnen, et al., Control. Fusion and Plasma Phys., Proc. Euro. Conf. (Maastricht) **23J** (1999) 717.
- 3.19 H. Gerhauser, R. Zagorski, H. A. Claassen and M. Lehnen, submitted to Contrib. Plasma Phys.
- 3.20 J. P. Freidberg, "Ideal Magnetohydrodynamics," Plenum Press, New York (1987).
- 3.21 P. Dumortier, et al., Control. Fusion and Plasma Phys., Proc. Euro. Conf. (Montpellier) **18B** Part I (1994) 74.

Chapter 4

- 4.1 J. Rapp, et al., Nucl. Fusion **39** (1999) 765.

- 4.2 A. Pospieszczyk, in "Atomic and Plasma-Material Interaction Processes in Controlled Thermonuclear Fusion," ed. R. K. Janev and H. W. Drawin, 1993.
- 4.3 J. Rapp, personal communication (1999-2000).
- 4.4 M. Z. Tokar, et al., J. Nucl. Mater. **266-269** (1999) 958.
- 4.5 R. J. Hawryluk, et al., in "Physics Close to Thermonuclear Conditions," (Commission of the European Communities, Brussels, 1980), Vol. 1, p19.
- 4.6 W. M. Stacey, Phys. Plasmas **4** (1997) 179.
- 4.7 E. W. Thomas and W. M. Stacey, Phys. Plasmas **5** (1998) 1015.
- 4.8 R. Hulse, Nucl. Technol./Fusion **3** (1983) 259.
- 4.9 J. Mandrekas, personal communication.
- 4.10 R. A. Hulse, D. E. Post and D. R. Mikkelsen, J. Phys. B: Atom. Molec. Phys. **13** (1980) 3895.
- 4.11 D. E. Post, J. Nucl. Mater. **220-222** (1995) 143.
- 4.12 M. Brix, personal communication (2000).
- 4.13 B. Schweer, M. Brix, and M. Lehnen, J. Nucl. Mater. **266-269** (1999) 673.

Chapter 5

- 5.1 J. Rapp, et al., 26th EPS Conf. on Contr. Fusion and Plasma Physics, Maastricht, Vol. **23J** (1999) 665.
- 5.2 G. Waidmann and G. Kuang, Nucl. Fusion **32** (1992) 645.
- 5.3 J. Winter, J. Nucl. Mater. **145-147** (1987) 131.

- 5.4 J. Winter, et al., J. Nucl. Mater. **162-164** (1989) 713.
- 5.5 U. Samm, et al., Plasma Phys. Control. Fusion **35** (1993) B167.
- 5.6 E. Hintz, et al., in Contributions to High Temperature Plasma Physics edited by K. H. Spatschek and J. Uhlenbusch, Akademik Verlag, Berlin (1994) 373.
- 5.7 J. Winter, J. Nucl. Mater. **176-177** (1990) 14.
- 5.8 U. Samm, et al., J. Nucl. Mater. **220-222** (1995) 25.
- 5.9 U. Samm, et al., J. Nucl. Mater. **176-177** (1990) 273.
- 5.10 J. Rapp, et al., Nucl. Fusion **39** (1999) 765.
- 5.11 F. C. Schüller, Plasma Phys. Control. Fusion **37** (1995) A135.
- 5.12 A. Krämer-Flecken, et al., Nucl. Fusion **33** (1993) 921.
- 5.13 M. Tokar, et al., J. Nucl. Mater. **266-269** (1999) 958.
- 5.14 U. Samm, et al., J. Nucl. Mater. **266-269** (1999) 666.
- 5.15 G. Sergienko, et al., 20th EPS Conf. on Contr. Fusion and Plasma Physics, Lisbon, Vol. 17C (1993) II-667.
- 5.16 P. C. de Vries, et al., Phys. Rev. Lett. **80** (1998) 3519.
- 5.17 B. Lipschultz, J. Nucl. Mater. **145-147** (1987) 15.
- 5.18 M. Greenwald, et al., Nucl. Fusion **28** (1988) 2199.
- 5.19 T. Nishitani, et al., J. Nucl. Mater. **176-177** (1990) 763.
- 5.20 A. Krämer-Flecken and G. Waidmann, 21st EPS Conf. on Contr. Fusion and Plasma Physics, Montpellier, Vol. 18B, Part I (1994) 122.

- 5.21 ITER Physics Expert Groups on Confinement and Transport and Confinement Modeling and Database, and ITER Physics Basis Editors, Nucl. Fusion **39** (1999) 2175.
- 5.22 Y. T. Lie, et al., 21st EPS Conf. on Contr. Fusion and Plasma Physics, Montpellier, 1994 Vol. **18B**, Part I (1994) 126.
- 5.23 J. W. Conner and H. R. Wilson, Plasma Phys. Contr. Fusion **36** (1994) 719.
- 5.24 J. Wesson, Tokamaks, 2nd Ed., Clarendon Press, Oxford, 1997.
- 5.25 M. A. Mahdavi, et al., 24th EPD Conf. on Contr. Fusion and Plasma Phys., Berchtesgaden, Vol. **21A**, Part III (1997) 1113.
- 5.26 G. D. Porter, et al., J. Nucl. Mater. **266-269** (1999) 917.
- 5.27 W. M. Stacey, Phys. Plasmas **4** (1997) 1069.
- 5.28 J. A. Wesson, et al., Nucl. Fusion **29** (1989) 641.
- 5.29 R. Janev, et al., J. Nucl. Mater. **121** (1984) 10.
- 5.30 W. Stacey, Phys. Plasmas **3** (1996) 2673.
- 5.31 C. E. Bush, et al., J. Nucl. Mater. **176-177** (1990) 786.

Chapter 6

- 6.1 D. M. Meade, et al., EPS 27th Conf. on Controlled Fusion and Plasma Physics, Budapest, 2000.
- 6.2 J. H. Schultz, IEEE/NPSS Symposium on Fusion Energy, Albuquerque, NM, 1999.
- 6.3 J. Mandrekas, personal communication (2000).

- 6.4 D. Zhang and J. Mandrekas, personal communication (2000).
- 6.5 D. E. Post, J. Nucl. Mater. **220-222** (1995) 143.
- 6.6 R. A. Hulse, et al., J. Phys. B: Atom. Molec. Phys. **13** (1980) 3895.
- 6.7 W. M. Stacey, J. Mandrekas, Nucl. Fusion **34** (1994) 1385.
- 6.8 W. M. Stacey, J. Mandrekas, R. Rubilar, "Interface Current Integral Transport Methods for the Calculation of Neutral Atom Transport in the Edge Region of Fusion Plasmas," to be published in Fusion Technology (2000).
- 6.9 R. Rubilar, W. M. Stacey, J. Mandrekas, "Neutral Particle Transport in the Edge and Divertor Region," submitted to Nuclear Fusion (2000).

VITA

Frederick Alan Kelly was born in Salem, Ohio on September 4th, 1953, the son of Thomas Russell Kelly and Dorothy Lois Hamilton Kelly. He attended the University of Cincinnati, where he received a Bachelor of Science degree (1976) in Electrical Engineering, a Master of Science degree (1978) in Electrical and Computer Engineering and a Doctor of Philosophy degree (1982) in Engineering Science.

He worked from 1982-1983 at the University of Cincinnati as a Research Assistant Professor on the dynamics and the inverse kinematics of industrial robots.

Dr. Kelly joined Michigan Technological University in 1983 as an Assistant Professor and developed a robot trajectory generation method.

In 1991, he entered the graduate program at the Georgia Institute of technology where he received a Master of Science degree (1992) in Nuclear Engineering and a Doctor of Philosophy degree (2001) in Nuclear Engineering.